Master's thesis

NTNU
Norwegian University of Science and Technology
Faculty of Natural Sciences
Department of Materials Science and Engineering

Martin Fast Buen

Effect of cerium-based master alloy on the solidification grain structure of austenitic stainless steel

Master's thesis in Material Science and Engineering
Supervisor: Yanjun Li
Co-supervisor: Leander Michels, Håkon T. Mauset
June 2023

NTNU
Norwegian University of
Science and Technology

Martin Fast Buen

Effect of cerium-based master alloy on the solidification grain structure of austenitic stainless steel

Master's thesis in Material Science and Engineering
Supervisor: Yanjun Li
Co-supervisor: Leander Michels, Håkon T. Mauset
June 2023

Norwegian University of Science and Technology
Faculty of Natural Sciences
Department of Materials Science and Engineering

NTNU
Norwegian University of
Science and Technology

Preface

This work has been carried out at the Department of Materials Technology, Norwegian University of Science and Technology and Elkem, Kristiansand, between January 2023 and June 2023. The work has been a collaboration between NTNU and Elkem Foundry Innovation Department. Professor Yanjun Li has been the supervisor for this project work, with Dr. Leander Michels and Håkon T. Mauset from Elkem as Co-supervisors. I would like to thank Professor Yanjun Li, who has been my supervisor during the course of this thesis. The discussions and guidance have been valuable. I would also like to thank Co-supervisor Dr. Leander Michels for helpful discussions on steel and EGR. Co-supervisor Håkon T. Mauset has been of essential assistance throughout the present work, from discussions to trivialities. Yingda Yu and Jarle Hjelen have provided essential assistance for the work on the JSM JEOL 840.

I want to thank Dr. Emmanuelle Ott and Dr. Gro Eide from Elkem and SFI RA2 for supporting this project. Dr. Eivind Hoel and Bente Kroka at Elkem Kristiansand also assisted with this work. Trondheim, June 2023 Martin Fast Buen

Abstract

The present work has studied the effect of a cerium-based grain refiner on the solidification structure and microparticle population in austenitic stainless steel. Smaller thermal analysis cups and larger Y-block samples underwent analysis in the form of LOM, SEM/EDX, AMICS, and EBSD. The developed and commercially available Elkem Grain Refiner(EGR) Stainseed was chosen for this purpose. The base steel for the study was a 316L austenitic stainless steel produced at Elkem, Kristiansand, in a pilot scale casting trial. As a highly reactive rare-earth element, cerium forms stable inclusions when added to the steel melt. These inclusions, cerium oxides, sulfides, aluminates, and oxysulphides, may act as nucleation sites for austenite grains. The effect of EGR addition on the solidification structure was studied in detail, in addition to a characterization of the non-metallic particles and intermetallic phases formed during solidification. Microparticle populations were acquired through AMICS and ImageJ analysis. EGR addition showed a refining effect on the solidification structure of the steel. Significant refinement of the columnar characteristics and grain size was observed. The secondary dendrite arm spacing was reduced by 27%, and the average grain size was reduced by up to 36% by adding EGR. The most frequent cerium inclusions observed in this work were $CeAlO_3$ and CeO_2. The addition of EGR was also found to completely remove the presence of Al_2O3 and, furthermore, reduced the number of intermetallic phases in the steel.

Sammendrag

Følgende arbeid har studert effekten av en cerium-basert kornforfiner på størkningstrukturen og mikropartikkel-populasjonen i et austenittisk rustfritt stål. Termisk anlayse kopper og større Y-blokk profiler har blitt analysert med hjelp av lysmikroskopi, SEM/EDX, AMICS og EBSD. Den kommersielt tilgjengelige Elkem Grain Refiner(EGR) Stainseed har blitt brukt til dette formålet. Utgangsstålet for studien var et 316L austenittisk rustfritt stål produsert som en del av et pilotskala smelteforsøk. Som et høyt reaktivt sjelden-jordart element, vil cerium danne stabile partikler når det blir tilsatt stålsmelten. Disse partiklene, som inkluder oksider, aluminater, sulfider og oksysulfider, kan opptre som lokasjoner hvor hetereogen kimdanning av austenitt korn kan initieres. Effekten av EGR tilsats på størkningstrukturen ble studert i detalj. I tilegg ble en karakterisasjon av ikke-metalliske parikler og intermetalliske faser utført. Mikropartikkel populasjoner ble hentet og analysert ved hjelp av AMICS og ImageJ analyse. EGR tilsats viste en forfinende effekt på den kolumnære karakteristikken og kornstørrelsen til stålet. Den sekundære dendrittarm avstanden ble redusert med 27% og den gjennomsnittelige kornstørrelsen ble redusert med opptil 36% med tilsats av EGR. Cerium partiklene som opptredde oftest i denne studien var $CeAlO_3$ og CeO_2. Tilsats av EGR viste også en total eliminasjon Al_2O3 partikler, og førte til en reduksjon av intermetalliske faser i stålet.

Contents

List of Figures

List of Tables

1 Introduction

Austenitic stainless steel alloys are considered an essential alloy class and are widely used for several applications today. They will continue to play an essential role in the future. The extensive use of this type of steel originates from its ability to form a passive oxide layer film, inducing robust self-protection against corrosion[1]. This is supplemented by the steel's high ductility and relatively high strength. The austenitic stainless steels are also superior from an economic perspective for their designated applications, for example, in marine constructions and the chemical industry[1].

Enhancing the mechanical properties of these steels will be beneficial in reducing the cost, energy consumption, and emissions associated with the transport and usage of these steels. A refinement of the as-cast solidification structure of austenitic stainless steel by inoculation treatment is a commonly used and effective practice in the industry. Inoculant particles are added to the steel melt, often in the form of master alloys, to act as heterogeneous nucleation sites upon which grain growth may be initiated, promoting a columnar to equiaxed transition in the steel. Furthermore, these solutes may slow down grain growth through the pinning effect and contribute to the constitutional undercooling in the melt, which is often responsible for generating a sufficient undercooling ahead of the solid/liquid interface, and thus providing the necessary driving force for the nucleation of equiaxed grains in this region.

Inoculant treatment of non-ferrous metals has undergone extensive studies in the last decades, and significant progress has been made in the field. However, the grain refining mechanisms of the inoculants are not yet fully understood in steels due to complex solidification processes. Generally, Ti-based or RE-based master alloys are used for the inoculation treatment of steels[2]. In the last decades, cerium-based inoculants have, together with other rare earth elements, undergone extensive research regarding their potency as grain refiners in steels. Elkem developed, in collaboration with NTNU, the Elkem Grain Refiner(EGR), a cerium master alloy designed to introduce particles to the steel melt for which the steel could nucleate heterogeneously, promoting equiaxed grain growth. Research has demonstrated promising results of grain refinement in, among others, duplex steels, austenitic manganese steels, and super austenitic steels by adding EGR[3, 4]. In the steel melt, the master alloy rapidly dissolves, and the highly reactive cerium will react with elements such as sulfur, oxygen, and aluminum. Different oxides, sulfides, oxysulfides, and aluminates are thus formed. The different crystal structures of these particles facilitate heterogeneous nucleation in different ways[5]. Furthermore, the size distribution and morphology of the inoculant inclusions are of importance for the nucleation processes during solidification[6]. Therefore, an investigation of the roles of cerium in master alloy and the addition rate on the refinement effect of the austenite grains during solidification and the impact on non-metallic particles in the steel will benefit in-depth understanding and further development for grain refiners in steels.

2 Theroretical background

2.1 Stainless steel

Stainless steels are highly valued in various industries due to their corrosion resistance, generated by a protective oxide film. To be considered stainless steel, it must contain at least 10.5 wt% chromium[1]. Moreover, they do not exceed 1.2 wt% carbon. Figure 1 shows the iron-carbon phase diagram. The stainless steels will be located to the left in the diagram, within the $\delta - \gamma - \alpha$ region. Depending on the combination of alloying elements, stainless steel can be fully austenitic, fully ferritic, a mixture of both, or martensitic, with varying properties and uses. The most common type of stainless steel is fully austenitic, which is ductile and has a strength high enough for a wide range of applications. Table 1 shows typical compositions for some austenitic stainless steels.

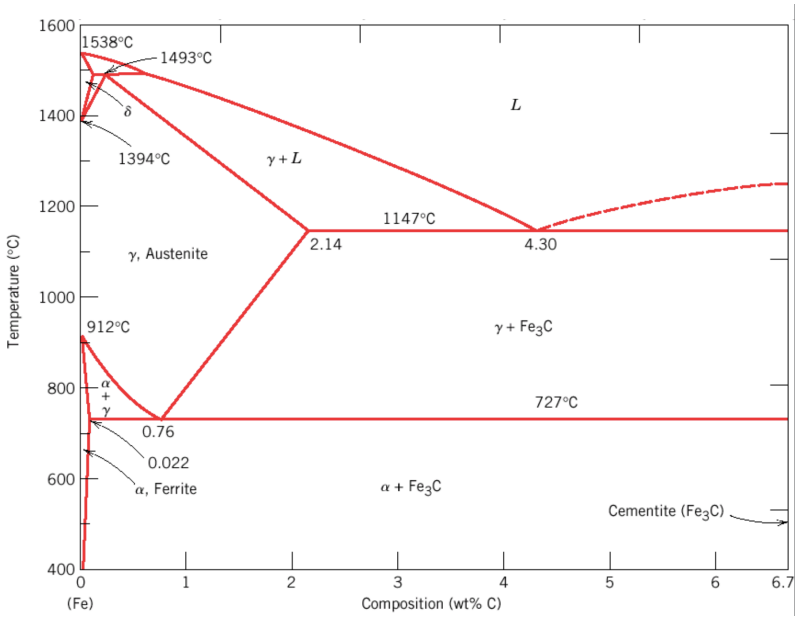

Figure 1: Iron-carbon phase diagram[1].

Table 1: Compositions of three widely used austenitic stainless steels from the AISI 300 series[7]. Percentages are in wt%.

Steel/Element	C max	Si max	Mn max	Cr	Mo	Ni
304	0.08%	1.0%	2.0%	18-20%	-	8-12%
316	0.08%	1.0%	2.0%	16-18%	2.0-3.0%	10-14%
316L	0.03%	1.0%	2.0%	16-18%	2.0-3.0%	10-14%

2.1.1 Alloying elements in austenitic steel

Austenitic stainless steels are often alloyed with elements that stabilize the austenite structure at lower temperatures. These elements, known as austenite stabilizers, promote austenite formation and are usually calculated in terms of Ni-equivalent, as nickel is a highly effective austenite former. Similarly, there are stabilizing elements for ferrite, called chromium-equivalents, with chromium being an effective ferrite former. The calculation of chromium and nickel equivalents can be done using the following formulas:[8]

$$Cr_{eq} = Cr + Mo + 1.5Si + 0.5Nb \tag{1}$$

$$Ni_{eq} = Ni + 30C + 0.5Mn \tag{2}$$

The impact of the chromium-equivalent and Ni-equivalent terms can be evaluated and analyzed using a Shaeffler diagram, as depicted in Figure 2. This diagram plots the chromium-equivalent on the x-axis and the Ni-equivalent on the y-axis. The equations presented previously indicate that molybdenum, silicon, and niobium have a stabilizing effect on ferrite, in addition to chromium. The stability of the austenite phase is also influenced by the contents of carbon and manganese, in addition to nickel.

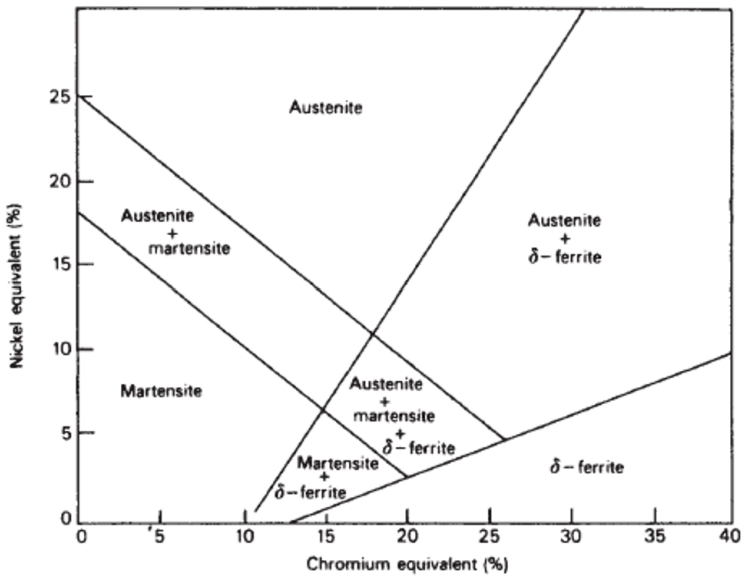

Figure 2: Scheffler diagram[8].

The properties of stainless steel can be significantly altered by incorporating specific alloying elements. In combination with heat treatment and, to some extent, impurities, the presence of these elements will determine the characteristics of a particular steel grade. The interactions between these factors will vary in different stainless steel types. The following elements are commonly added to stainless steel alloys:

1. Chromium provides the stainless steel with general corrosion resistance by forming a passive oxide layer on the surface. The oxidation resistance is increased with increasing chromium content in the alloy. A higher chromium addition will result in an enhancement of these effects.

2. Molybdenum significantly improves the resistance to localized and uniform corrosion while slightly increasing the strength. Molybdenum also promotes the formation of secondary phases in stainless steel. [9]

3. Nickel generally increases the ductility and toughness of the steel and reduces the corrosion rate in an active state. [9, 10]

4. Manganese increases the solubility of nitrogen in steels and is therefore widely used in austenitic stainless steels. Additionally, it acts as an austenite former and can replace some of the nickel content in stainless steel.

5. Nitrogen significantly enhances the mechanical strength of stainless steels and increases the resistance to localized corrosion, especially when combined with molybdenum, resulting in a synergistic effect.[11]

2.1.2 Intermetallics and particle formation

Stainless steels are generally vulnerable to developing undesired phases and precipitates during manufacturing as they contain a high concentration of alloying elements[12]. The presence of σ-phase and χ-phase, as well as large precipitates of carbides, particularly chromium carbides, can negatively impact the steel by decreasing its strength and ductility as a result of their brittle characteristics. These phases can also result in local depletion of alloying elements such as chromium (Cr) and molybdenum (Mo), reducing the material's corrosion resistance.[1, 12]

The precipitation of intermetallic phases in stainless steel has been extensively researched[13, 14, 15]. It is well documented that the compositions of the σ and χ phases vary slightly with the composition of the steel in question. Additionally, the compositions will be affected by in which phase they are forming. Hence, studies and experimental data give different compositions. Table 2 gives the approximate compositions of the σ and χ phases.

Table 2: Compositional ranges of σ phase and χ phase in stainless steels. Values in wt percent.

	Si	**Mo**	**Cr**	**Mn**	**Fe**	**Ni**
σ	0.4-1-0	4.0-8-0	26.5-31	1.3-1.8	47-58	4.7-11
χ	0.4-1-3	9.0-11.5	23-26	1.3-2-3	59-60	3.5-4.6

2.2 Solidification theory

2.2.1 Heat extraction

For a liquid metal to solidify, heat extraction is required[16]. Heat extraction leads to a change in the energy of both the solid and liquid phases in the system. This change is achieved through two mechanisms:

1. A decrease in the enthalpy of the liquid or solid due to cooling.
2. A decrease in the enthalpy of the liquid due to the liquid-solid transformation, which is equal to the latent heat of fusion.

Heat extraction occurs upon the application of cooling to the system, resulting in an external heat flux. The cooling rate can be determined by conducting a heat balance, assuming that the metal is isothermal and the solid and liquid's specific heat is equal. The cooling rate, represented by $\dot{T}$, can be calculated using the following equation[16]:

$$\dot{T} = \frac{dT}{dt} = -q_e(\frac{A'}{vc}) + (\frac{df_s}{dt})(\frac{\Delta h_f}{c}) \tag{3}$$

where $\dot{T}$ is the cooling rate, q_e is the external heat flux due to the applied heating, A' is the surface area of the casting, and v is its volume. c is the specific heat, f_s is the solid fraction and Δh_f is the latent heat per unit volume. The equation considers both a geometric term, reflecting the effect of the casting geometry, and the continuous evolution of latent heat of fusion from the solidification process.

2.3 Structural zones in castings

During the solidification of liquid metal in a mold or crucible, distinct structural zones are formed[16, 17].

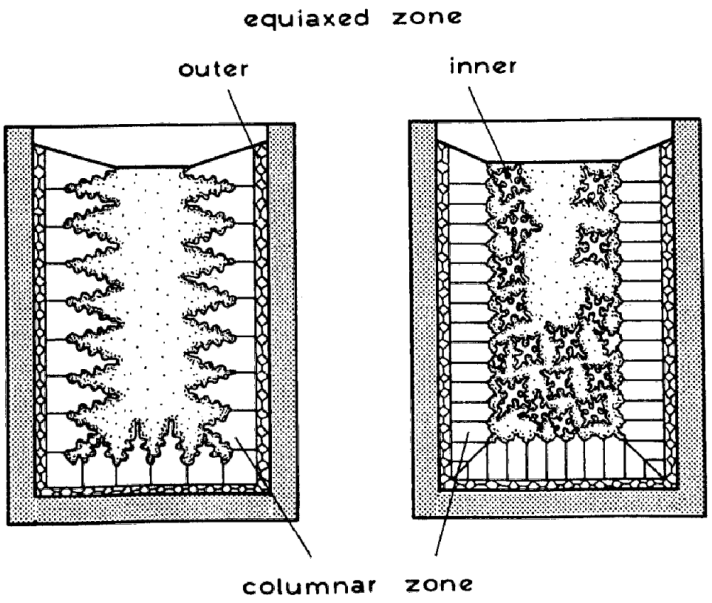

Figure 3: Structural zones in casting[16].

An equiaxed zone is formed along the mould's walls due to the liquid metal's rapid cooling to below its liquidus temperature as a result of the temperature difference between the liquid metal and mould walls. The high undercooling promotes large nucleation of grains in this region, developing a fine equiaxed zone.[16, 17]

Subsequently, directional columnar growth towards the center of the mould occurs. The crystals in the outer equiaxed zone that can grow parallel or opposite to the heat flow direction are favored, resulting in the establishment of a columnar zone. The center of a casting typically consists of randomly oriented coarse equiaxed grains, which may have nucleated on detached branches from the columnar dendrites or nucleation sites ahead of the solid/liquid interface in the undercooled melt. The detached dendrite arms can grow into equiaxed grains if transported and isolated by convection in the melt, while stable solid particles in the undercooled melt can serve as nucleation sites for the growth of new grains.[17]

2.4 Homogenous nucleation

The initiation of the solidification process is dominated by nucleation, including during columnar dendrite solidification, where each nucleus leads to the formation of a single equiaxed grain. To solidify a pure melt, a substantial supercooling below the metal's liquidus temperature is necessary to generate a significant driving force for nucleation. With adequate supercooling, clusters of atoms exceeding a critical size can initiate a nucleation process. By assuming a spherical shape, the critical size can be calculated as follows:

$$r^0 = \frac{2\sigma}{\Delta T_R \Delta S_f} \tag{4}$$

where σ is the solid/liquid interface energy, ΔT_R is the undercooling below the melting point and ΔS_f is the entropy of fusion.

With the number of atoms per volume, v', the number of atoms in a nucleus is given by:

$$n \approx \frac{4\pi r^3}{3v'} \tag{5}$$

The liquid atoms have to arrange themselves on the site of a corresponding crystal lattice for the nucleation of a spherical crystal to occur.

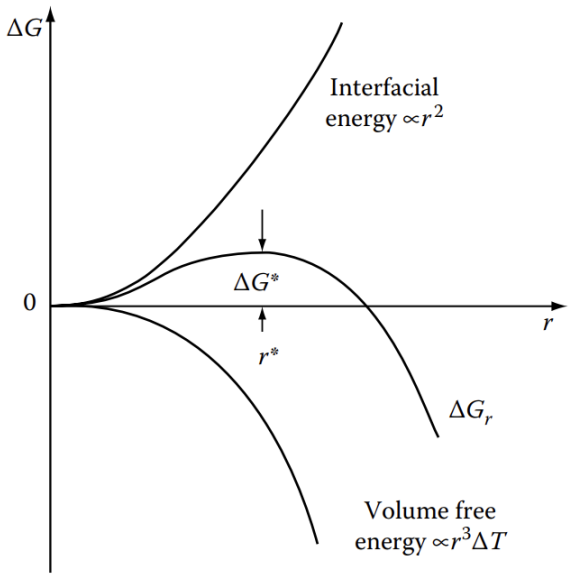

Figure 4: Variations in ΔG^* for embryo formation[18].

By adding the terms for the interface and volume Gibbs free energy, the total energy change for nucleation can be calculated:

$$\Delta G = \sigma 4\pi r^2 + \frac{\Delta g 4\pi r^3}{3} \tag{6}$$

The critical activation energy required to form a crystal nucleus which will continue to grow, will be the maximum value of Equation 6. This maximum can be obtained by:

$$\frac{d(\Delta G)}{dr} = 0 \tag{7}$$

The activation energy for the nucleation of a spherical particle in a pure melt is then[16]:

$$\Delta G_n^\circ = \left(\frac{16\pi}{3}\right)\left(\frac{\sigma^3}{\Delta g^2}\right), \Delta g = \Delta T_R \Delta S_f \tag{8}$$

2.5 Heterogenous nucleation

Heterogenous nucleation will to a much larger degree, describe the nucleation mechanisms and kinetics of real systems. In heterogeneous nucleation, solidification is initiated on foreign surfaces[17]. The foreign surfaces can be impurities in the melt, detached dendrite arms, or deliberate addition of substrates to control the microstructure. Classical nucleation theory states that the kinetics of heterogeneous nucleation is determined by the equilibrium of the interfacial energies shown in Figure 5.

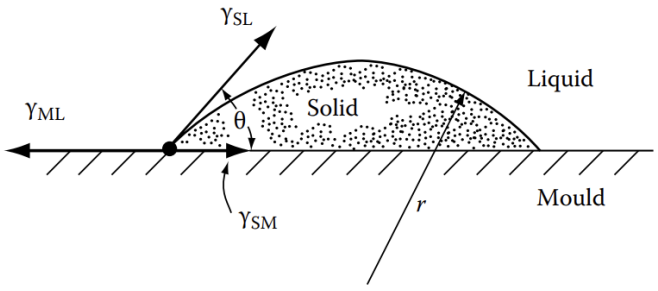

Figure 5: Heterogeneous nucleation of a spherical cap on a flat mould wall[18]. In the Figure, θ is the wetting angle, and γ_{SL}, γ_{ML} and γ_{SM} are the boundary surface tension between solid/liquid, mould/liquid and solid/mould respectively.

The various surface energies in Figure 5 can be related to the wetting angle, θ, through a force balance known as the Young-Laplace equation, given as:

$$\gamma_{ml} = \gamma_{sm} + \gamma_{sl} cos(\theta) \tag{9}$$

When $\gamma_{ml} > \gamma_{sm} + \gamma_{sl}$, the solid layer will completely cover the substrate, separating the liquid from the substrate. For the condition that $\gamma_{sm} > \gamma_{ml} + \gamma_{sl}$, there will be no gain of energy by solid layer formation on the foreign particle surface. Therefore, substrates that fulfill this criterion will not participate in a heterogeneous nucleation process. In the two described cases, there will be no value for the wetting angle, θ, that satisfies Equation 9. [17]

The main cases of interest, especially for grain refinement by inoculation, are when the solution for the contact angle satisfies

$$\left|\frac{\gamma_{ml} - \gamma_{sm}}{\gamma_{sl}}\right| \leq 1 \tag{10}$$

The solid is "wetting" the surface when $0 \leq \theta \leq \frac{\pi}{2}$.

By the same method of derivation of the nucleation energy barrier for homogenous nucleation, it can be shown that:

$$\Delta G^{\circ}_{n,het} = \left(\frac{16\pi}{3}\right)\left(\frac{\sigma^3}{\Delta g^2}\right) f(\theta) = \Delta G^{\circ}_{n,hom} f(\theta) \tag{11}$$

It is then evident that the nucleation energy barrier is reduced by a factor of $f(\theta)$ for heterogenous nucleation compared to homogenous nucleation.

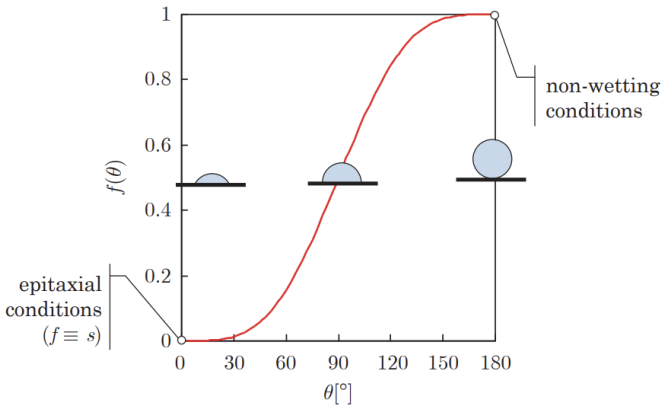

Figure 6: $f(\theta)$ function in heterogenous nucleation [17].

Through geometrical calculations[16], it can be derived that the scale of the wetting angle effect can be measured through:

$$f(\theta) = \frac{(2 + cos(\theta))(1 - cos(\theta))^2}{4} \tag{12}$$

Figure 6 shows how $f(\theta)$ varies with the wetting angle and illustrates three main wetting cases. Perfect wetting of the solid phase on the substrate is acquired when $\theta = 0$. An ideal compatibility between the two phases will then exist. In a solidifying melt, this case may occur when solidification is initiated on the solidifying metal itself, for instance, on dendrite arms detached by partial remelting as a result of convection[16, 17]. These fragments will act as potent nucleation sites. The potency of possible nucleation sites will decrease with increasing wetting angle.

The mechanisms of heterogenous nucleation have been extensively studied in the last decades[19, 20, 21], leading to new theories regarding the nucleation behaviors of equiaxed grains.

Classical nucleation theory long stated that heterogeneous nucleation is a stochastic process, where the generation of nuclei of a new phase in the melt must be thermally activated by an undercooling below the liquidus temperature[16, 17]. This corresponds to Figure 5

and Equation 9. Quested and Greer[19] analyzed the competition between classical thermal nucleation and athermal nucleation, in essence, the competition between a stochastic and deterministic process. In the deterministic process, the number of nucleation events in the liquid is a function of undercooling, not time or the initial formation of a solid layer upon the nucleant area.

As the spherical-cap model will have difficulties describing nucleation behaviors when θ is small, as is the case for potent nucleation sites such as designated inoculant particles, the classical nucleation theory is not working in many cases. Quested and Greer found that for nucleant areas of micron scale, thermal nucleation is negligible, and thus the nucleation of solid is deterministic.

2.6 Constitutional undercooling

During alloy solidification, a distribution coefficient, k, less than one, will result in a lower solubility of solute elements in the solid, causing a buildup of excess solute ahead of the solid/liquid interface[16]. As a result, a solute-enriched boundary layer will form during the transient growth phase before the start of steady-state growth. The concentration gradient in this layer significantly impacts the local equilibrium liquidus temperature of the liquid.

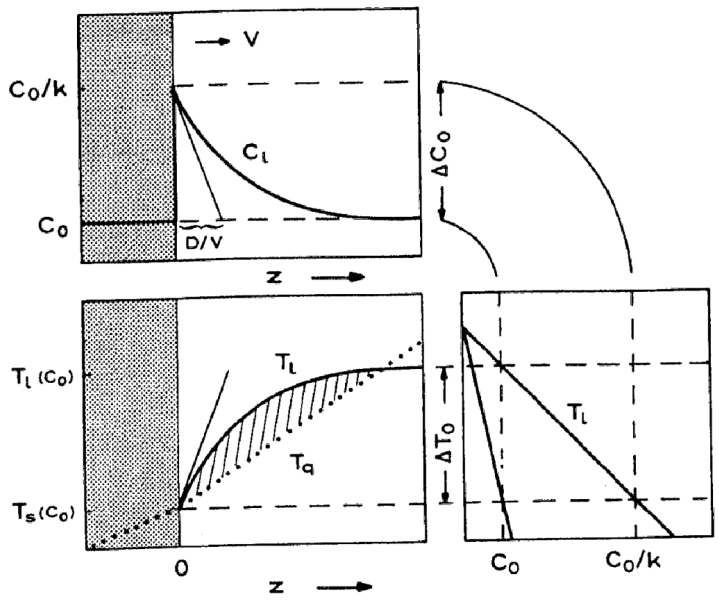

Figure 7: Constitutional undercooling in alloys[16].

The existence of a constitutional undercooled zone will depend on the temperature gradient in the liquid at the solid/liquid interface. This zone is defined as the melt volume ahead of the interface, where the actual temperature is lower than the local equilibrium solidification

temperature[22]. As a result, the melt in this zone is undercooled.

The presence of a constitutionally undercooled zone requires that the temperature gradient, G, at the interface in the liquid, should be smaller than the gradient of liquidus temperature change in the melt. For alloys, this implies that the interface is constitutionally undercooled when $G < mG_c$, where G_c represents the concentration gradient, and m is the liquidus slope[16].

2.7 Segregation

The solid/liquid interface rejects solute into the liquid as the solubility of the solute element is larger there than in the solid. However, when the solubility is larger in the solid than in the liquid, the solute will be enriched in the solid, generating a depleted zone ahead of the solid/liquid interface[17]. The solid concentration at the interface between solid and liquid is related to the liquid concentration by the equilibrium distribution coefficient:

$$C_s^* = kC_l^* \tag{13}$$

This difference in the composition will always lead to variations in concentration in the solidified alloy. This phenomenon is called segregation, and it is partly responsible for interdendritic precipitates, porosity, and concentration differences across dendrite arms and grains.

The high alloying contents in stainless steels make them susceptible to segregation of elements to interdendritic regions[23]. The extent of the segregation largely depends upon the alloy composition and the cooling rate during solidification and following cooling to room temperature. Solute-enriched regions can decompose at lower temperatures to form Mo-rich σ-phase if the steel contains molybdenum. This is, as mentioned in Section 2.1.2, a brittle phase that may be detrimental to the mechanical properties of the alloy.

2.7.1 Secondary dendrite arm spacing

The secondary dendrite arm spacing is closely related to the segregation in castings. During solidification, alloying elements and impurities will segregate into intercellular and interdendritic spaces. This will lead to compositional variations within the as-cast ingot. [16]

Secondary arms start forming close to the tip of the primary dendrite as a perturbation and will, as in the case of an unstable planar solid/liquid interface, grow and become cell-like. Some of them will be eliminated by neighboring arms, leading to only some becoming real secondary dendrite arms that will grow perpendicular to the primary arm for cubic

crystals. These dendritic arms stop growing when the diffusion field of their tips comes into contact with those growing from a neighboring dendrite. A coarsening of the arms then happens[16, 24].

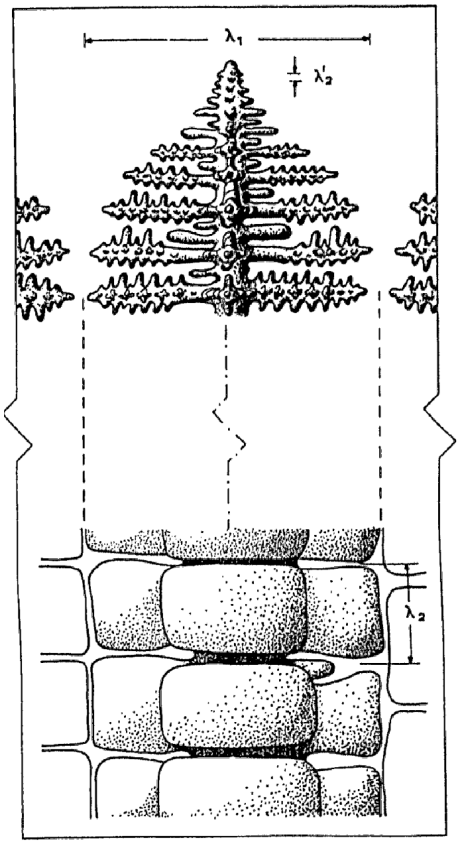

Figure 8: Growing primary dendrite with the formation and growth of secondary dendrite arms[16].

It is generally accepted that the secondary dendrite arm spacing is a function of the local solidification time, t_f, and thus also the cooling rate, $\dot{T}$. The secondary dendrite arm spacing can thus be described by:

$$\lambda_2 = \mu_0 t_f^{\frac{1}{3}} \tag{14}$$

where μ_0 is a material specific constant[24].

Experimental data on secondary dendrite arm spacing have been reported to fit a secondary dendrite arm spacing vs. cooling rate curve[25]:

$$\lambda_2 = \mu_1 \dot{T}^{-0.34 \pm 0.02} \tag{15}$$

where μ_1 is a material specific constant.

Secondary dendrite arm spacing measurements can give information about the local solidification conditions. It is an important parameter as it can determine the spacing of

precipitates or porosity in castings, which can significantly affect the mechanical properties of alloys.

2.8 Grain refinement

A common characteristic of most metals is their ability to solidify into polycrystalline volumes, inducing many smaller crystals commonly referred to as grains. These crystals in the solidified material are oriented in different orientations. The properties of the metal are, to a large degree, affected by the size of the grains. The yield strength of the metal is significantly affected by the grain size. The yield strength is defined as the stress at which the material starts to experience plastic deformation[26]. The effect is quantified through the Hall-Petch relation:

$$\sigma_y = \sigma_0 + \frac{k_y}{\sqrt{d}} \tag{16}$$

where σ_y is the yield strength of the material, σ_0 is the resistance of the lattice toward dislocation movement, k_y is a material-specific constant, and d is the average diameter of the grains. From the equation, it can be observed that the yield strength of the material is inversely proportional to the square root of the grain size. This effect results from the impeding effect of moving dislocations experience from grain boundaries[26]. As the number of grains increases in the metal, the total area of grain boundaries increases, increasing the yield strength. This contributes to the motivation for the refinement of grains in metals along with other benefits, such as minimizing the effect on the amount of segregation and porosity in steel ingots and castings[10, 27, 28], and is why grain refinement is a widely used technique in the metal industry.

There exist three main mechanisms to refine the equiaxed grain structure of an alloy during solidification[17]. One is through agitation of the melt. Applying mechanical means such as controlled electromagnetic stirring generates strong convection in the liquid. This can induce the partial remelting or fragmentation of existing dendrite arms, creating smaller solid fragments in the melt from which growth can start. Another is the mediated nucleation of another phase forming more easily from the liquid state. The third primary grain refinement mechanism is inoculating the melt by adding inoculant particles, on which heterogeneous nucleation can be initiated.

2.8.1 Grain refinement by inoculation

Inoculation-based grain refinement and the effect of different factors on grain refiner efficiency have been extensively studied. It is well-documented that this type of microstructure refinement is an effective and potent method.

Grain refiners are often added to the metal melt to achieve a refined grain structure and a larger fraction of equiaxed grains compared to columnar grains. In many cases, these are solid particles introduced into the melt as inoculants to act as nucleation sites from where heterogenous nucleation can begin.

Inoculation treatment has been proven to be an effective method for the grain refinement of steels[5, 29]. For being an efficient grain refiner, three main criteria are required for a potent inoculant:[29, 30]

1. The particles must be solid at the liquidus temperature of the metal.
2. The particles must be thermodynamically stable in the melt.
3. A low wetting angle must exist between the metal and the grain refiner.

To achieve effective of grain refinement, a fine distribution of inoculants is required throughout the whole melt. Grong et al[2] proposed that the optimal distribution of inoculants in the melt is to have many particles around the size of $1\mu m$ in diameter, as can be seen in Figure 9.

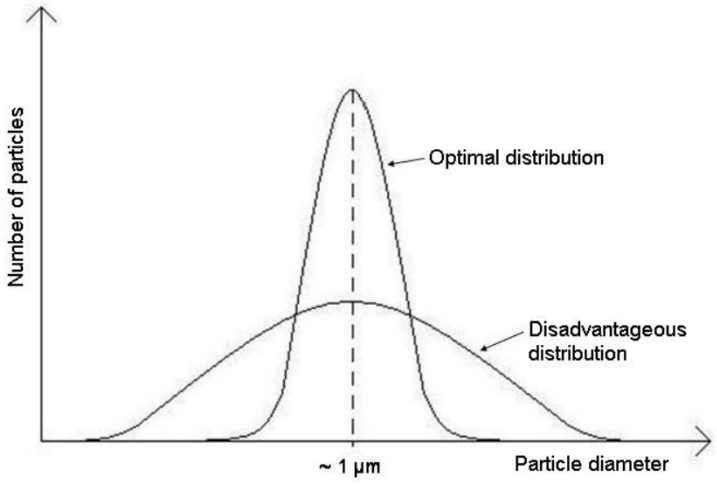

Figure 9: Optimal inoculant distribution [2].

A disadvantageous distribution is thus significant variations in the diameter of the inoculants, with few of the size $1\mu m$.

The grain refiner efficiency is influenced by the morphology, size distribution, and volume fraction of the inoculants[31, 6]. Greer et al.'s *Free growth theory*[6] proposes that the onset of a free growth condition controls the number of nucleated grains. The grain will grow from a nucleant particle at an undercooling inversely proportional to the particle diameter. The critical undercooling for free growth can therefore be related to the nucleant particle size by:

$$\Delta T_n = \frac{4\gamma_{sl}}{\Delta S_v d} \tag{17}$$

where ΔT_n is the critical undercooling for nucleation, γ_{sl} is the interfacial energy between the liquid and nucleation particle, ΔS_v is the nucleation entropy of fusion per unit volume and d is the diameter of spherical nucleation particle.

Another model for studying the efficiency of potent nucleants is the *Interdependence Theory*. This analytical model suggests that the constitutional undercooling and not the particle size is the limiting factor for the potency of the nucleant[32]. The model proposes that three main factors determine the final grain size of the metal[20]:

1. The distance an already nucleated grain must grow before a critical level of constitutional undercooling has been reached in order to nucleate the next grain.
2. The size of the critical constitutionally undercooled zone.
3. The distance from the critical constitutionally undercooled zone to the next potent particle.

Grain refiner efficiency is thus achieved by minimizing the nucleation-free zone from the first two factors. This can be achieved by increasing the growth restriction factor, Q, described in Section 2.8.3. The third and final factor emphasizes the importance of the distribution and density of the particles and, thus, why grain clustering should be avoided.

2.8.2 Lattice mismatch models for grain refiners

To improve the nucleation rate and the grain refiner efficiency, classic nucleation theory states that the interfacial energy between the grain refiner and the nucleus formed on it is required to be as low as possible.[5] Several factors influence the interfacial energy, including the crystallographic atomic matching between the nucleation phase and the nucleating agents. Atomic matching is usually used to evaluate a specific grain refiner's potency for inoculation in combination with a specific material. The atomic matching is based on the following two assumptions:

1. Coherent or semi-coherent interfaces between two solids will correspond to lower interfacial energy compared to an incoherent interface.
2. By maximizing the atomic matching across the interface, the interfacial energy can be minimized.

The Bramfitt two-dimensional disregistry model[5] has been widely used to evaluate grain refiner efficiency in the past decades. It measures the disregistry between the lattices of

the solid metal and a specific inoculant. In the model, the lattice disregistry is expressed as:

$$\delta_{(hkl)_n}^{(hkl)_s} = \sum_{i=1}^{3} [\frac{|d^i_{[uvw]_s} cos(\theta) - d^i_{[uvw]_n}|}{d^i_{[uvw]_n}}] * \frac{1}{3} * 100\% \tag{18}$$

where δ is the lattice disregistry, $[hkl]_s$ is a low-index plane of the inoculant in which $[uvw]_s$ is a low-index direction, $[hkl]_n$ is a low-index plane of the nucleus in which $[uvw]_n$ is a low index direction. $d_{[uvw]_s}$ is the interatomic spacing along $[uvw]_s$ and θ is the angle between $[uvw]_s$ and $[uvw]_n$. The lower the lattice disregistry is, the more potent the grain refiner is. According to Bramfitt, the criteria for a grain refiner to be effective is when the lattice disregistry, δ, is below 6%.[5]

The edge-to-edge model developed by M.X Zhang and P.M. Kelly[33] is a more recent model for determining grain refiner efficiency. Like the Bramfitt model, it is also based on minimizing the interfacial energy between lattices by maximizing the atomic matching across the interface. However, rather than the matching of lattices in the two-dimensional Bramfitt model, the edge-to-edge model quantifies the actual atomic matching at the interface between two phases. Figure 10 illustrates the principles of the E2EM model.

In general, the primary requirement of the model is the atomic matching along parallel atomic rows between two phases. These rows should be close-packed directions with a low interatomic spacing misfit, f_r. The E2EM model requires that straight rows match straight rows and zigzag rows match zigzag rows. These rows are called matching directions. The E2EM model additionally requires a pair of close-packed planes that contains the matching directions. These planes need a small interplanar spacing misfit, f_d, and are termed matching planes. Given that these requirements are fulfilled, an advantageous orientation relationship exists between the two phases. If both f_r and f_d are below 10%, the matching between the phases is satisfactory.

The E2EM model is superior to Bramfitt's disregistry model because of its ability to predict favorable orientation relationships. Additionally, the E2EM model focuses on close-packed planes and directions, which negates the problem of identifying low-index planes often associated with Bramfitt's model.

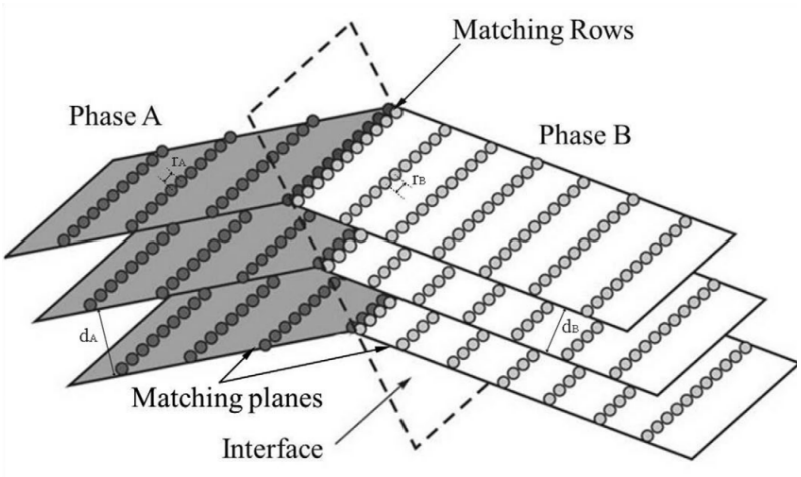

Figure 10: Schematic arrangement of sets of planes in two phases meeting edge-to-edge at an interface. The close-packed atom rows are parallel and match in the interface habit plane (shown dotted). Adapted from [34].

Due to the edge-to-edge matching model, new rare-earth-based grain refiners have been developed for ferritic steels[35] based on models and theories established in light alloys [36, 37].

2.8.3 Effect of solutes

The chemical compositions of alloys influence the effect of grain refinement, in addition to the type, size, and amount of inoculants. Extensive research on the solute and alloying elements' effect on grain refinement has been done[21, 38, 39, 40, 41]. This effect is due to the solute effect on the restriction of grain growth. As the solute re-partitioning takes place in the liquid ahead of the solid/liquid interface of the growing grain, a solute-enriched region is established. This will, as mentioned in Section 2.6, generate a constitutional undercooled zone. Additionally, a solute-suppressed nucleation zone is formed. Earlier studies propose that minimizing the extent of the solute-suppressed nucleation zone will improve the nucleation efficiency and grain refinement potential during solidification[42, 43]. In the *Interdependence theory*[20], it is proposed that the addition of effective solutes can reduce the width of the solute-suppressed nucleation zone via a growth restriction factor. This growth restriction effect can be quantified through the Q-factor. The concept was initially proposed by Maxwell[44] to describe the effect of solutes on the grain refinement mechanism. The growth restriction factor, Q, can for a binary alloy system be described as:

$$Q = mC_0(k-1) \tag{19}$$

where m is the liquidus slope, C_0 is the concentration of solute in the system, and k is the equilibrium partitioning coefficient.

Provided that the solute does not interact with other solutes or inoculant particles in the melt, a higher Q-value will generally benefit the grain refinement mechanism. Solute interactions are, however, inevitable. Quested and co-workers[31] thus proposed an alternate equation for the growth restriction factor, reflecting the initial rate of the development of constitutional undercooling with respect to the fraction of the solidifying phase.

$$Q = (\frac{\partial(\Delta T_s)}{\partial(\Delta f_s)})_{f_s \to 0} \tag{20}$$

where ΔT_s is the maximum constitutional undercooling and f_s is the solid mass fraction.

2.8.4 Effect of temperature gradient

Grain size prediction models are often based on the assumption of isothermal melt solidification. For casting and real purposes, the concept of unrestricted growth of dendrites in an infinite undercooled melt is insufficient to describe the growth mechanisms. These cases are normally associated with temperature gradients, constraining the dendrites from growing in the direction of the temperature gradient[17]. These gradients will always exist within the melt and often increase with the size of the casting. The effect of the temperature gradient in a melt has been extensively studied by experiments with unidirectional solidification, directional solidification by chill casting[45, 46, 47], and modeling studies[48, 49, 50]. The research shows that the temperature gradient significantly affects the columnar to equiaxed transition(CET), where a lower temperature gradient generally favors equiaxed solidification.

2.8.5 Fading mechanism

The fading mechanism is a phenomenon often observed during the inoculation treatment of metals. A gradually declining effect of the added inoculants on the grain refinement can be observed with increased time of the inoculants in the melt. Several explanations exist as to why this phenomenon occurs. Agglomeration of the inoculant particles is considered one of the primary reasons for the fading mechanism. The longer the inoculant particles stay in the melt, the more they are likely to agglomerate[51]. Research shows that a source for fading in the melt also is due to the settling of inoculant particles at the bottom or wall of the crucible, in addition to the chemical stability of the nucleating compounds is important to the fading phenomenon. [51]

2.8.6 Inoculation grain refinement in steel

Inoculation treatment through the addition of grain refiners through master alloys is currently the most efficient and reliable way for the grain refinement of steel. However, the

development and research on effective inoculant grain refiners for steel are not as substantial as their non-ferrous counterparts. Hence the mechanisms for specific inoculation processes in steel are still not fully understood. Inoculation grain refinement in steels can be challenging due to complex solidification processes. The solidification of steel will, in many cases, include $L \rightarrow \delta$, $L \rightarrow \gamma$, the peritectic transformation $L + \delta \rightarrow \gamma$, and the solid-state transformation $\delta \rightarrow \gamma$. Hence, the inoculation grain refinement of steel must take into account both the refinement mechanisms of δ-ferrite and austenite.

Generally, heterogeneous nucleation and solute restriction have been used to explain grain refinement in steel. The heterogeneous nucleation theories generally include crystallographic studies on the inoculants to evaluate grain refining efficiency. The grain refiners for δ-ferrite are usually divided into two groups: (i) Titanium compounds and (ii) RE compounds. The results from some planar disregistry calculations between different inoculant particles and the ferrite phase in steel are displayed in Figure 11. It indicates that many rare-earth oxides and some sulfides may efficiently nucleate δ-ferrite grains in steel. The titanium compounds, TiN and TiC, have been extensively used and are effective grain refiners for ferritic stainless steel attributed to heterogenous nuclation[52, 53, 54, 55]. Many RE inclusions also exhibit low lattice disregistry with δ ferrite and austenite and have effectively refined the solidification structure of steels[56, 57] These include Ce and La inclusions.

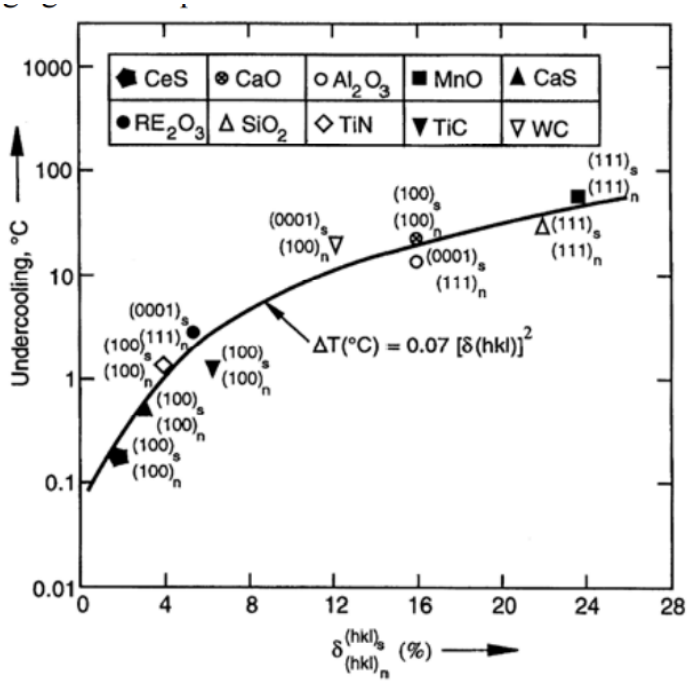

Figure 11: Undercooling required vs. planar disregistry between some given particles and ferrite phase in steels[58].

The grain refinement mechanisms of the titanium compounds and RE inclusions in steels are not yet fully understood. It is unclear if the grain refinement is due to the restriction

of grain growth via the growth restriction factor or due to the heterogeneous nucleation of grains on the inoculants.

Li and coworkers[59] studied commonly used grain refiners in low and medium-carbon steels. Using the E2EM model on NbO, CeS, TiN, Ce_2O_3 and TiC they found the following order for grain refiner efficiency in δ-ferrite:

$$NbO > CeS > TiN > Ce_2O_3 > TiC$$

2.8.7 Cerium as grain refiner

Cerium, a rare earth element, has been extensively used in grain refiners for steel and cast irons in the last decades. Due to the high affinity of cerium with other elements often encountered in metal melts, such as sulfur, oxygen, and aluminum, cerium is known to form stable inclusions in the melt. Many of these inclusions satisfy the requirements for potent grain refiners described in Section 2.8.1. In steels, these inclusions include oxides, sulfides, oxysulfides, and aluminates. Extensive research has been conducted on cerium-based grain refiners, and their positive effects on the solidification structures of different steels have been well documented[3, 4, 60].

Comparisons with grain-refiner models, such as the Bramfitt and E2EM models, reveal that cerium inclusions serve as potent nucleation sites for the solidification of austenite and ferrite grains in the steel melt. In studies by Yang et al[60], the lattice disregistry according to the Bramfitt model between austenite, Ce_2O_3, and Ce_2O_2S were 7.7% and 10.2% respectively. In the work of Van Der Eijk et al[4], the lattice disregistry between $CeAlO_3$ and austenite was 3.82%. Based on the criteria of the Bramfitt model, $CeAlO_3$ will thus be the most potent inoculant for the nucleation of austenite grains. Ji et al[61] calculated the lattice disregisties between δ-ferrite and cerium oxides, sulfides, and oxysulfides using the E2EM model. The results are listed in Table 3. The smaller values of the f_r and f_d imply that the Ce_2O_3, Ce_2O_2S and CeS particles are potent as heterogeneous nucleation sites for the δ-ferrite during the solidification of steels.

Table 3: Interatomic Spacing Misfit (f_r) and Interplanar Spacing Mismatch (f_d) of close-packed planes between $\delta - ferrite$ and $Ce_2O_3/CeS/Ce_2O_2S$. Adapted from [61].

Compound	**misfit(f_r)**	**mismatch(f_d)**
Ce_2O_3	4.60%	1.97%
CeS	1.51%	1.51%
Ce_2O_2S	4.27%	4.27%

Recently, extensive research efforts on the effect of cerium addition on non-metallic inclusions and the order of formation of cerium inclusions in steel melt have been proposed[62,

63, 64]. It is suggested and that Ce-rich particles form according to the following order when the steel is deoxidized:

$$Al_2O_3 \rightarrow CeAlO_3 \rightarrow Ce_2O_2S \rightarrow Ce_2O_2S + CeS \tag{21}$$

This is the case for many steels, as a deoxidation process is common before casting.

A study on high-sulfur steel with cerium addition[64] suggests that the forming of cerium sulfides and oxysulfides can be initiated on MnS particles. In aluminum-killed steels, the order of formation has been suggested as follows:

$$Ce_2O_3 \rightarrow Ce_2O_2S \rightarrow CeS \tag{22}$$

Figure 12 shows the relationship between Gibbs free energy and temperature, focusing on the formation of common cerium oxides, sulfides, and oxysulfides found in steels. Figure 13 illustrates the phase stability of Ce_2O_3 and $CeAlO_3$ within a Ce-Al-O-Fe-20%Cr-10% Ni system. Figure 12 shows that the cerium oxides are the most stable phases, followed by oxysulfides when no Al is present in the melt. The oxides are thus expected to form more frequently and before the sulfides. Figure 13 shows that when the concentration of Al reaches a certain level, the cerium aluminates will be the more stable inclusion.

Figure 14 reveals that the Al_2O_3 nonmetallic inclusions experience the lowest Gibbs free energy when modified by cerium, resulting in the formation of $CeAlO_3$ nonmetallic inclusions. Further, it is evident that even a small quantity of cerium in the steel can induce modification of the Al_2O_3 inclusions. As the content of cerium increases, Ce_2O_2S nonmetallic inclusions are formed in the steel, following the initial formation of $CeAlO_3$. [62]

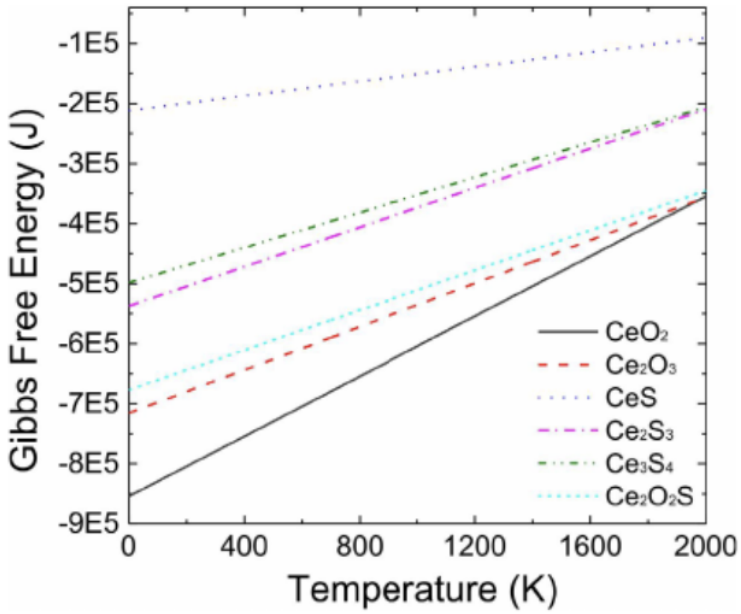

Figure 12: Gibbs free energy of formation for various cerium oxides and sulfides at various temperatures[65].

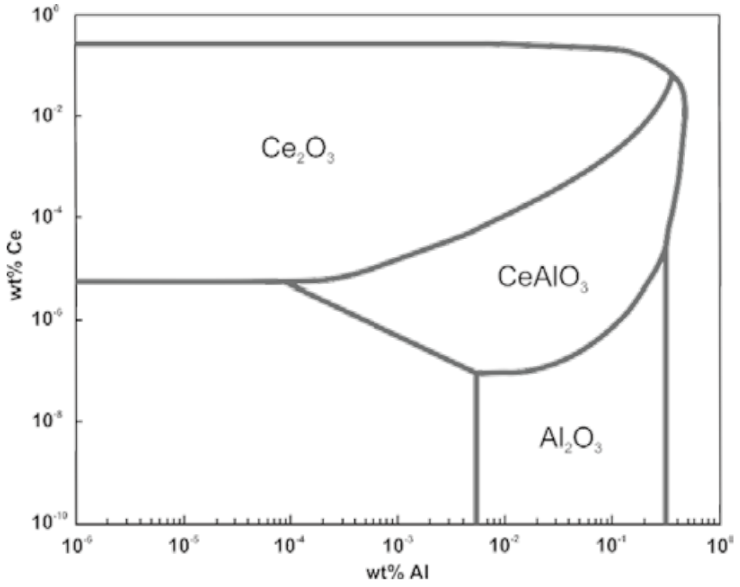

Figure 13: Phase stability diagram at 1550°C in Ce-Al-O-Fe-20%Cr-10%Ni system. Maximum dissolved oxygen is limited to 100 ppm[66].

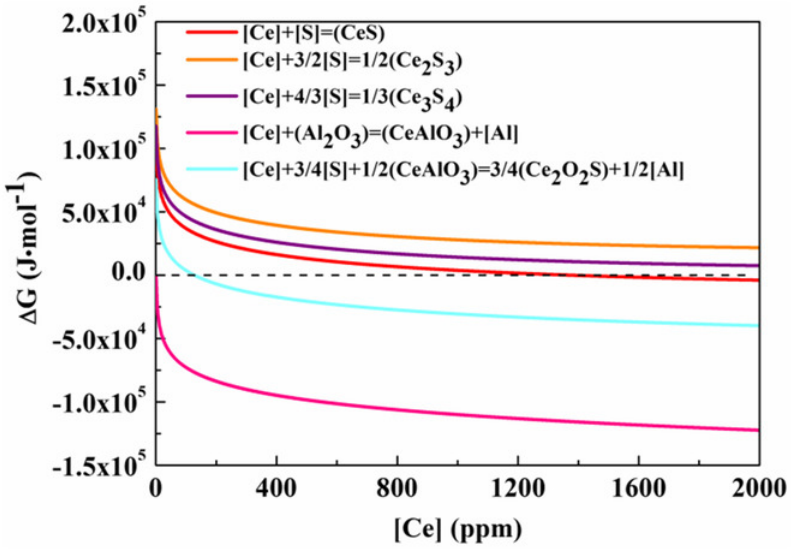

Figure 14: Gibbs free energy versus dissolved Ce content[62].

2.9 Particle distribution

To better quantify the inclusions and achieve a broader understanding of the inclusion distribution in the steel, the following thesis employs a 2D-to-3D model to convert relevant particles into three-dimensional inclusions. Thus, the experimental data will quantify both area- and volume-number densities.

Several methods in the literature can be used for the procedure[67]. The present work used the Finite Difference Method by Basak and Sengupta[68] in order to estimate the size distributions and the total number of particles per mm^3 in the samples. This method has been used to study size distributions and the total number densities for graphite and the entire non-metallic microparticle population in cast iron[69].

The 2D size distribution from the original data is divided into k class intervals, each of size Δ. Here $(N_A)_i$ is the number of particles per unit area(mm^{-2}) in the interval $\Delta(i-1)$ to Δi, where $1 \leq i \leq k$. $N_V(j)$ is then obtainable as:

$$N_V(j) = \Delta^{-1} \sum_{i=j}^{k} A(i,j) N_A(i) \tag{23}$$

As shown in [68], $A(i,j)$ can be calculated as:

$$A(i,j) = \begin{cases} 1 & (i=j), \\ \frac{2}{\pi}\left[\frac{j+\sqrt{j^2-(j-1)^2}}{j-1}\right] & \forall(j>1) \end{cases} \tag{24}$$

$A(i,j)$ is then:

$$A(i,j) = \frac{2}{\pi} \ln \left[\frac{i+\sqrt{i^2-(j-1)^2}}{i+\sqrt{i^2-j^2}} * \frac{i-1+\sqrt{(i-1)^2-j^2}}{i-1+\sqrt{(i-1)^2-(j-1)^2}} \right] \forall (i > j) \tag{25}$$

The total number of particles in a volume is thus:

$$N_{V,Total} = \sum_{j=1}^{k} N_V(\Delta j) \tag{26}$$

A log-normal distribution was used for the fitting of the number-particle densities. It is given as follows:

$$\frac{dn}{d\phi} = \frac{n_{max}}{\phi_\sigma \sqrt{2\pi}} \frac{1}{\phi} exp \left[-\frac{1}{2} \left(\frac{\ln \phi - \ln \phi_0}{\phi_\sigma} \right)^2 \right] \tag{27}$$

3 Experimental

3.1 Elkem grain refiner(EGR)

The cerium was added as Elkem Grain Refiner(EGR) StainSeed^{TM}. EGR is a commercially available master alloy containing cerium. It consists of crushed pieces in size range of 2-20 mm with the composition seen in Table 4

Table 4: EGR StainSeed^{TM} composition. All percentages are in weight percent.

Element	**Ce**	**Si**	**Cr**	**C**	**Fe**
Target	10-14%	18-22%	28-34%	<0.15%	Balance

In a steel melt, the EGR pieces are dissolved, and the cerium will react quickly with available aluminum, oxygen, and sulfur. The non-metallic inclusions formed when the cerium reacts are thermodynamically stable in the melt and work as nucleation sites during the solidification of the steel. To achieve maximum effect, the EGR should be added to the steel melt after the deoxidation before the casting, typically done during the tapping from the furnace into the ladle. Starting at one-third full ladle, the EGR should be added progressively to the metal stream. This will ensure the maximum yield of cerium.

3.2 Casting trial

The material studied in the thesis was an alloy with the target composition of an austenitic 316L stainless steel. The target composition of the steel is listed in Table 5. The samples and addition levels of EGR studied in the following thesis are a few chosen from a larger selection consisting of several castings and addition levels. The melting trial was performed by professional employees at Elkem, Kristiansand.

Table 5: Requirements to and target composition for trial steel in weight percent.

	C	**Si**	**Mn**	**P**	**S**	**Cr**	**Ni**	**Mo**	**N**	**Al**
Min	0					16.5	10	2		
Max	0.07	1.0	2.0	0.045	0.015	18.5	13	2.5		
Target	0.03	0.3	0.9		<0.001	17	12	2	0.04	0.03

3.2.1 Furnace

The steel composition was acquired by mixing steel plates from YC INOX, extra Nickel, and melt from previous trials of the same steel grade. 270 kg of steel melt was produced during the trial. Initially, the material was heated to a melt of around 1650 °Celsius

before a review of the slag was done to decide whether $FeSi$ should be added to the melt to reduce the amount of slag. Then the temperature was further increased to 1700°Celsius before the melt was deoxidized with 0.3kg Al coins. A deslagging of the melt was then done, and the melt was poured into the transport ladle to heat it before being returned to the furnace. A small amount of the melt was extracted for chemical analysis to decide if adjustments with Al, FeCr, Ni, and FeMo were needed to obtain the correct composition. Lastly, the melt was deslagged thoroughly and deoxidized with 0.3 kg Al before going into the transport ladle.

3.2.2 Rig

The rig setup and an overview of the melting trials, including addition levels of EGR and the different blocks cast, are illustrated in Figure 15. A total of six casting ladles with different addition levels of EGR were done in the trial. The EGR was weighed and added to the bottom of each ladle before the pouring of the melt. Ideally, the EGR was to be added progressively to the metal stream during pouring to ensure a high cerium recovery rate in the steel.

For each addition level of EGR, the following test blocks were cast:

- 1 Y-block type IV.
- 1 Vertical tensile block.
- 1 Step block.
- 2 Econ-O-Carb cups from Heraeus(designated for thermal analysis).
- 1 Quick cup(for chemical analysis).

The casting order of the trials is as seen in Figure 15, with the test block casting order being:

1. Econ-O-Carb cups.
2. Quick cup.
3. Step block.
4. Vertical tensile block.
5. Y-block.

In Figure 16, the actual setup of the blocks is shown, while in Figures 17 and 18, each type of block and cup is labeled.

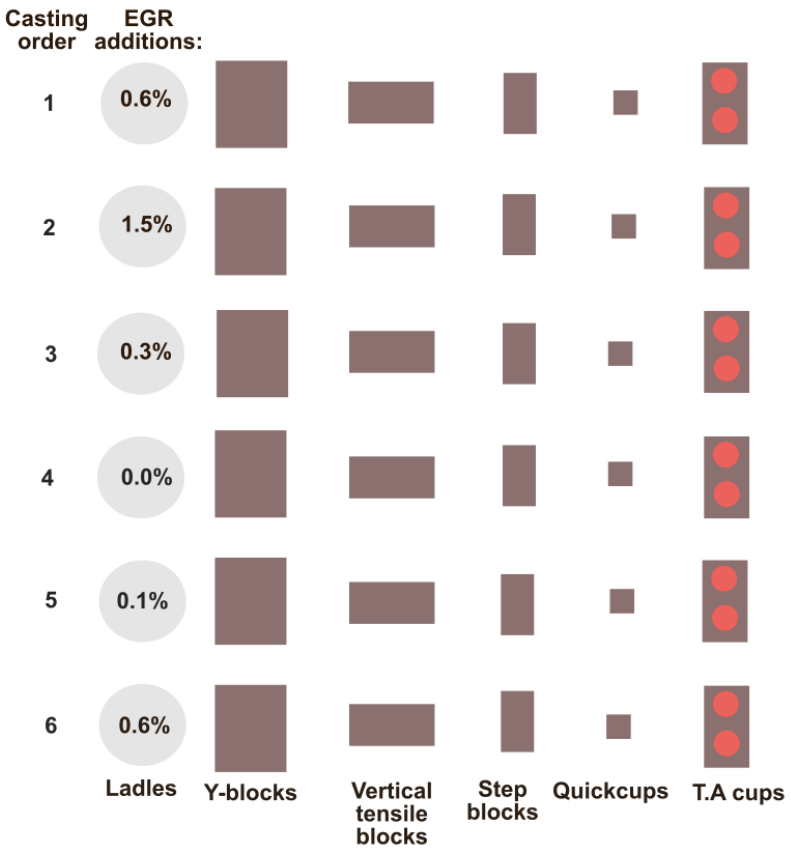

Figure 15: Trial overview: Casting order, EGR-addition levels, and castings.

Figure 16: Rig setup. Casting order from right to left.

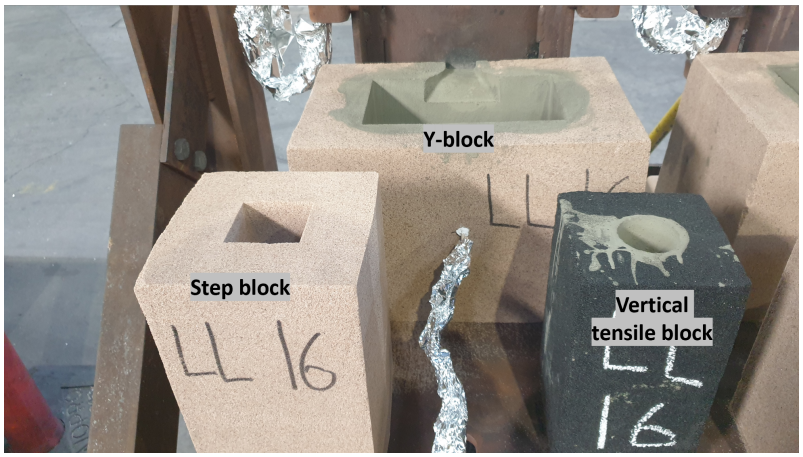

Figure 17: Y-block, stepblock and vertical tensile cup.

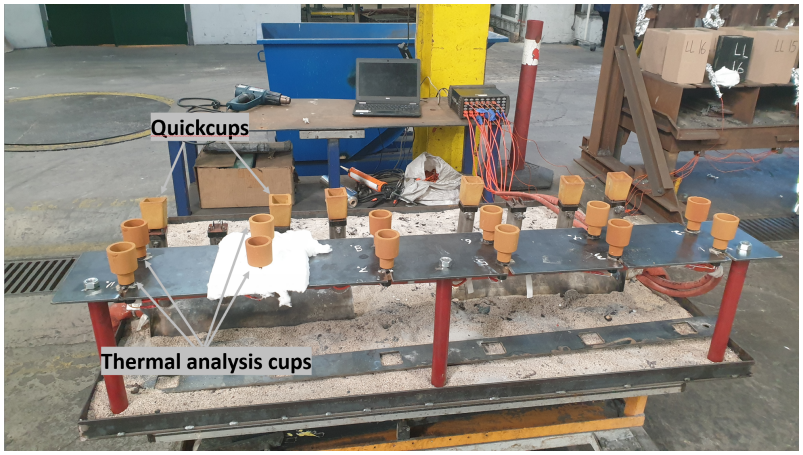

Figure 18: Quickcups and thermal analysis cups.

3.3 Sample preparation

The samples used in the thesis are based on the casting trials' Y-blocks and thermal analysis cups. Figure 19 shows the dimensions of the Y-block and where the block samples for analysis were extracted.

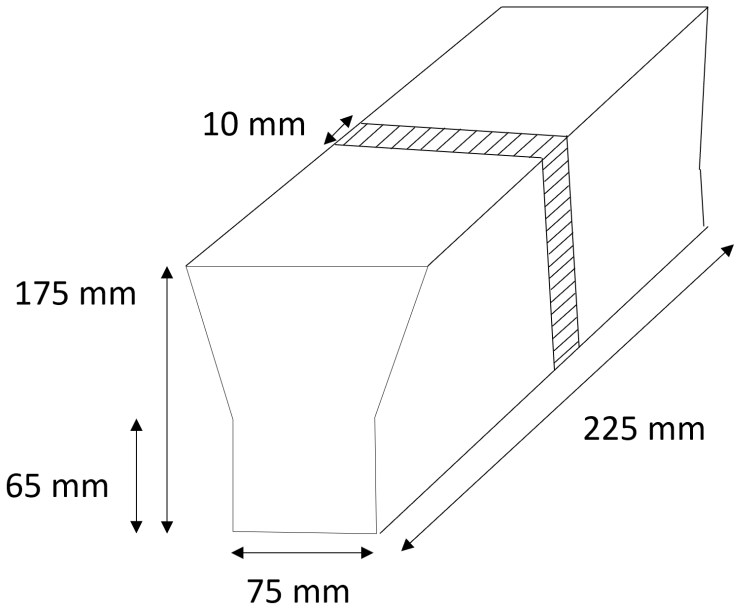

Figure 19: Y-block dimension and where samples were extracted(lined area).

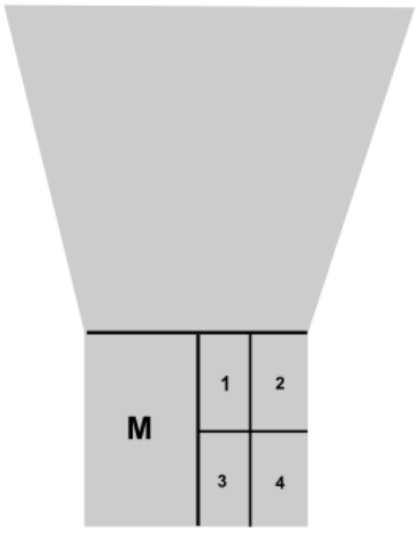

Figure 20: Numbering and placement of samples in the Y-block.

Figure 21 shows the dimensions of the thermal analysis cups and how the samples were extracted.

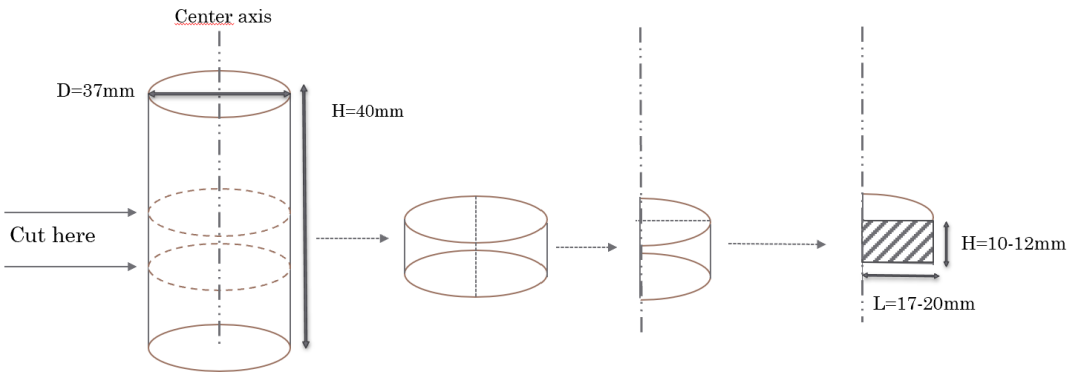

Figure 21: Sample cutting of thermal analysis cups.

The samples were grounded and polished on a Struers Tegramin-30 automatic grinding machine. The abrasive mediums used to ground the samples were MD piano 80, 220, 500, 800, 1200, and 4000 SiC discs from Struers. Polishing was done in three steps with diamond suspension: $3\mu m$ on an MD Dac plate, $1\mu m$ on an MD Nap plate, and $0.25\mu m$ on an MD Nap plate. Between each grounding and polishing step, the samples were cleaned with soap and water before receiving 5 minutes of ultrasound bathing. After polishing with diamond suspension, each sample was vibration polished in a Buehler Vibromet 2 with a Mastermet 2 colloidal silica suspension for 4 hours at 60 Hz. Two steel discs of 200 grams were added on the back during vibration polishing to obtain the maxiumum effect.

3.4 EBSD mapping

The samples were 32.5x18.5x10 mm, with some variations due to the cutting. A JSM Jeol 840 SEM fitted with an "online" NORDIF EBSD detector with a Comboscan addon was used, where "online" means the indexing of the EBSD patterns happens simultaneously with the pattern acquisition. Based on knowledge of the large as-cast grain size of austenite, the ability to comboscan the surface area was deemed necessary. Due to the machine commonly being used for very thin silicon wafers, a fitting sample holder for the steel samples did not exist. Hence, M4 screw threads were drilled 7mm into the back of each sample so that eccentric height could be maintained in the machine with settings adjusted for the silicon wafers.

For each session on the JSM Jeol 840, several parameters had to be optimized. The PCD detector had to be inserted to optimize the current and gun alignment. The X- and Y-stigmators had to be adjusted, and focus was found. Lastly, the dynamic focus was turned on and optimized for each sample by adjusting the amplitude. Before starting the EBSD scan, background removal was performed to get clear Kikuchi patterns during mapping. A calibration was performed after clear patterns were acquired by optimizing the exposure time. Only the gamma-iron phase was indexed during EBSD mapping to save pattern

acquisition time. The calibration was done close to the sample surface to negate minor differences in height across the sample surfaces due to the sample preparation.

For the mapping, the following parameters and values were used:

Table 6: SEM and EBSD parameters for EBSD pattern acquisition.

Parameter	Value
Magnification	25X
Working distance	24-27mm
Acceleration voltage	20.0 kV
Tilting angle	62.5°
Scan stepsize	$100\mu m$
Dynamic focus	On

The EBSD data were further analyzed with EDAX OIM analysis software, generating grain-boundary maps and orientation maps for each sample.

3.5 SEM and EDX

EDX analysis and SEM imaging of the samples were done with a Zeiss ULTRA 55 FEG-SEM using an Everhart-Thornley Secondary Electron Detector, a retractable Back Scattered Electron Detector, and a Bruker XFlash EDS detector. Esprit software was used to acquire compositional maps and spectra for particles and larger areas on the samples.

Table 7: Parameters and values for SEM and EDX analysis.

Parameter	EDX	SEM
Accelerating voltage	15 kV	20 kV
Working Distance	11mm	24mm

3.6 AMICS

Advanced Mineral Identification and Characterization System(AMICS) analysis was done to acquire data for the size and compositional particle distribution of the samples.

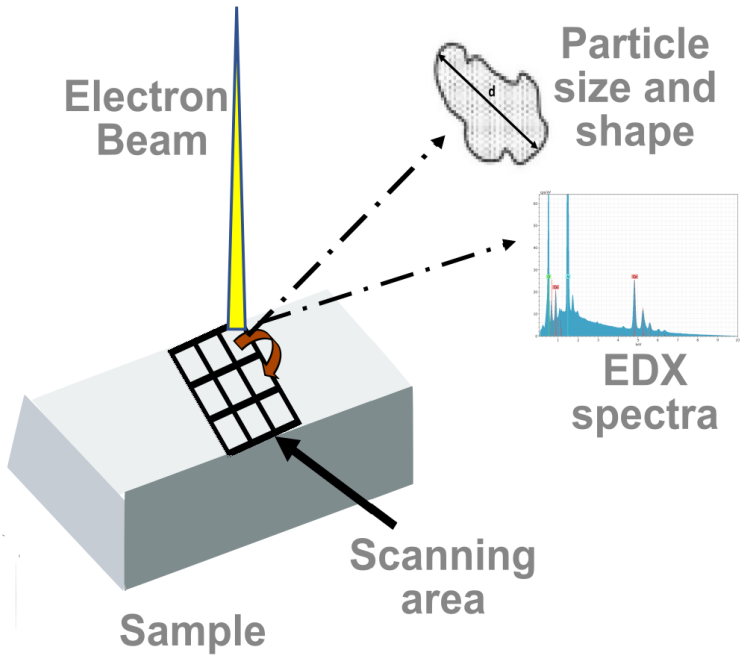

Figure 22: Principles of AMICS. A predetermined scanning area is automatically scanned. Particles and phases are automatically characterized by EDX and logged.

The analysis was done on a Zeiss Gemini SEM with a Bruker XFlash EDS detector. The composition(from EDX), area, feret size, and the number of particles were logged in an Excel sheet. This data was later sorted and categorized by an operator at Elkem. The categories were:

- Sulfides
- Aluminum oxides
- Metallics
- Cerium particles
- Pores
- Others

Table 8 give the area scanned during the AMICS analysis for each sample.

Table 8: The area scanned for each sample in AMICS.

	Y-block inoc	**Y-block ref.**	**T.A. cup inoc.**	**T.A. cup ref.**
Area	18.67 mm^2	18.67 mm^2	23.7 mm^2	18.7 mm^2

3.7 Chemical analysis

Chemical analysis of the samples from the casting trial was done with Optical Emission Spectrograph(OES), X-ray fluorescence (XRF) and combustion analysis at Degerfors laboratory in Degerfors, Sweden.

3.8 Thermal analysis

Temperature data from the trial were measured in the T.A. cups. These were Econ-O-Carb cups, an expendable test cup fitted with a high-grade S-type thermocouple (Pt 10% Pt/Rh) sticking up from the bottom protected with a quartz tube. Cooling curves were recorded using a data logger with a frequency of 10 Hz.

The data was plotted in Python in the forms of cooling curves(temperature versus time) and cooling rates(dT/dt versus time). A fitting of the curves was required to filter out noise from the data. The derivative was then calculated using the Numpy library in Python. The plots were then analyzed, giving information about solidus and liquidus temperatures and other phase transformations.

FactSage version 8.2 were used to calculate equilibrium phase diagrams for the samples. The databases used were: FactPS, FSstel, FTOxid, and FTOxCN. The input parameters were the compositions measured in the chemical analysis.

3.9 Particle and grain size distributions

Average grain size calculations were done with the intercept method[70].

The data acquired from AMICS were analyzed and plotted in Python in the form of number density in mm^{-3} as a function of particle diameter. This was done by converting the measured two-dimensional number densities to three-dimensional values. A Finite Difference Method was used for the conversion, the method of which is described in section 2.9. A log-normal fitting of the data was also performed, using equation 27.

A grain size analysis on the EBSD maps was done in the ImageJ software with the Fiji plugin extension. The software measured the maximum and minimum feret size of the grains. The feret size of the grains was used with the same Python script as the particles to convert the grains from two-dimensional to three-dimensional structures.

4 Results

4.1 Chemical analysis

The results of the chemical analysis of the reference and inoculated samples are listed in Table 9. The amount of chromium is lower for the experimental samples than for a standard 316L alloy, which should contain at least 16.5% chromium, 10% nickel, and 2% molybdenum[1]. The manganese concentration of the experimental castings is also about half of the target concentration. A higher nickel content than the minimum was targeted to minimize the amount of δ-ferrite formation during solidification.

Table 9: Chemical compositions of the experimental reference and inoculated alloy. All values in wt%.

Sample	C	Si	Mn	P	Cr	Ni	Mo	Al	N	Ce	O
Ref.	0.032	0.51	0.44	0.031	16.17	11.74	1.94	0.039	0.031	0	0.0067
Inoc.	0.033	0.70	0.45	0.031	16.33	11.65	1.92	0.050	0.032	0.050	0.0094

Table 10 depicts the addition level of EGR to each sample, the corresponding target concentration of Ce with 100% recovery rate, the measured Ce composition by OES, and the resulting cerium recovery. The cerium recovery ratio in the trial was low, with a decrease in recovery with increasing EGR addition level.

Table 10: EGR addition, target and measured content of Ce, and recovery of Ce.

Sample	EGR[wt%]	Target Ce[wt%]	Measured Ce[wt%]	Recovery
Ref.	0.0%	0.0%	0.0%	-
Inoc.	1.2%	0.195%	0.050%	25.6%

4.2 FactSage equilibrium diagrams

The equilibrium phases in the reference and inoculated samples were calculated with the FactSage software. The measured chemical compositions were used as the input of the models. The calculated fraction of different phases is given in Figures 23a and 23b.

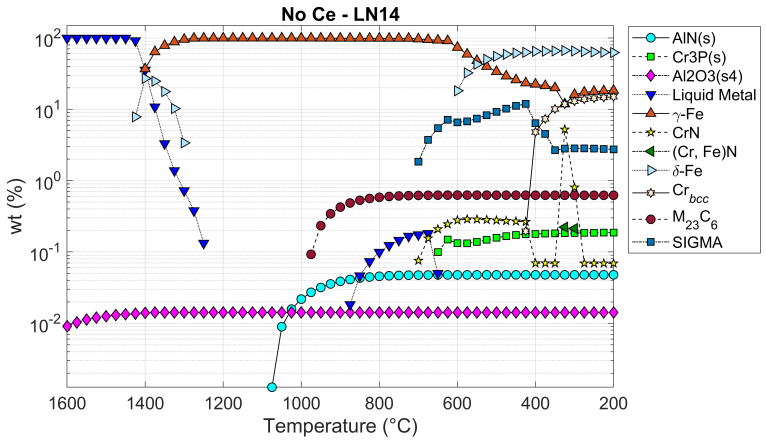

(a)

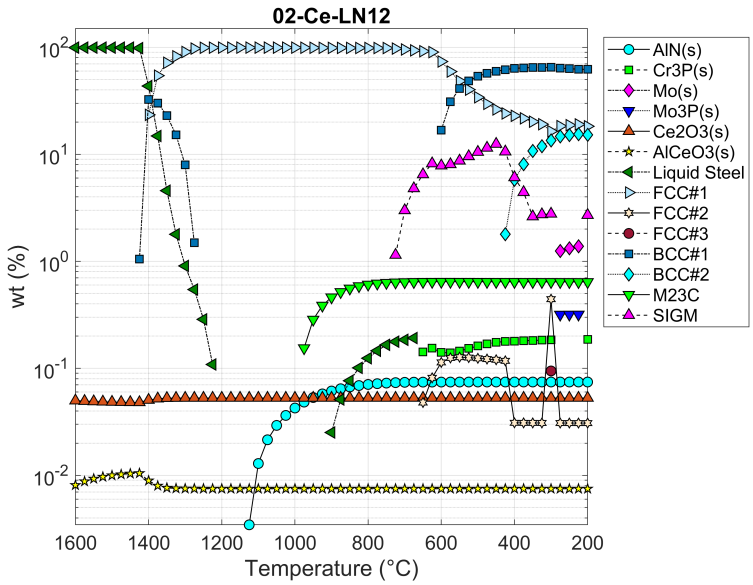

(b)

Figure 23: Calculated phase fractions as a function of temperature from Factsage for $\gamma - iron$ with no cerium(23a) and 0.050% cerium(23b). A logarithmic scale is used for the vertical axis. The calculations were performed by Elkem.

As observed in the diagrams, the solidification starts with the formation of δ-ferrite first, followed by a $L - \gamma + \delta$ transformation. A liquid-to-austenite transformation and a solid-state δ-ferrite-to-austenite transformation then occur. As the austenite is cooled further, the σ-phase precipitation is expected at about 760°C and a phase transformation to δ-ferrite at 610°C. It has to be noted that these diagrams are indicative and may not reflect the actual phases obtained during solidification with experimental conditions.

The solidus and liquidus temperatures calculated in FactSage are given in Table 11.

Table 11: Liquidus and solidus temperatures of the experimental steels calculated by FactSage.

	Reference	**With EGR**
Eq. Liquidus[°C]	1400-1425	1425
Eq. Solidus[°C]	1225-1300	1225-1250

4.3 Grain refinement analysis of T.A. cups

The measured cooling curves and the derived cooling rates for the solidification of the reference and EGR-inoculated T.A. cup are presented in Figure 24. The temperature dataset of both parallels was analyzed and plotted. Large deviations existed between the inoculated and reference sample and between each parallel.

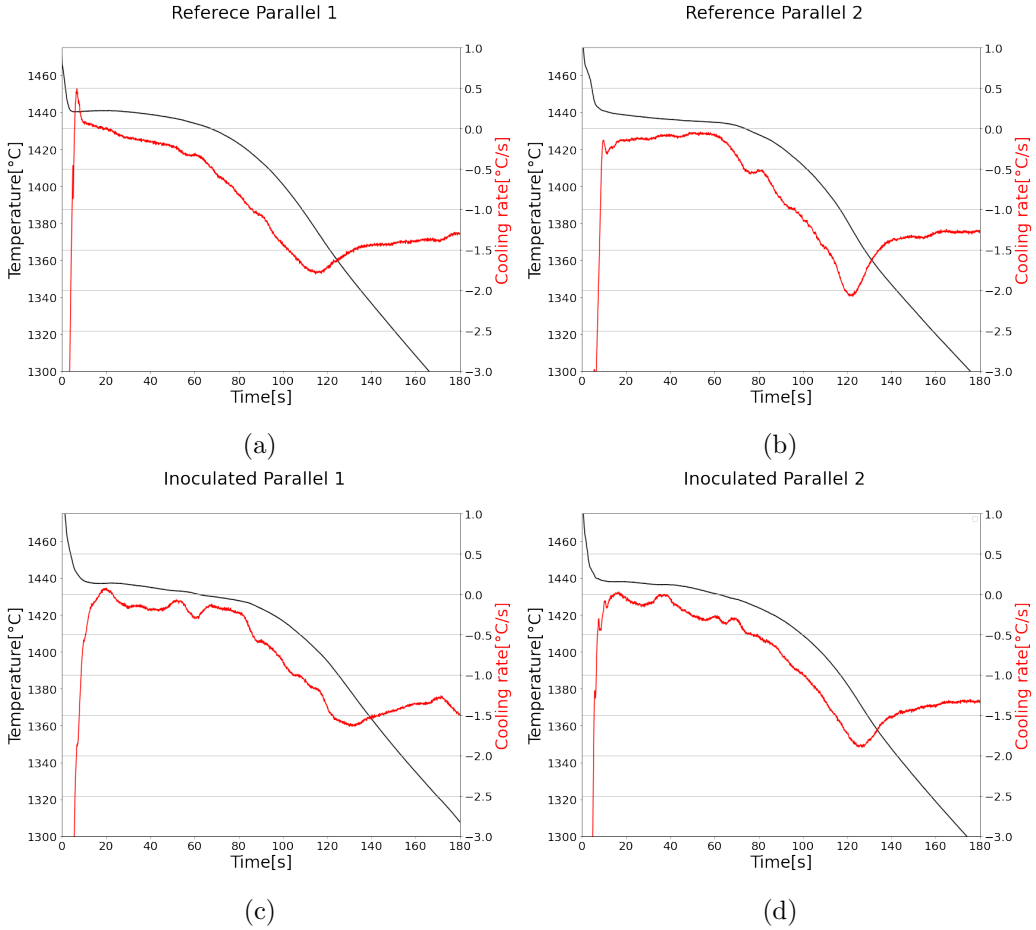

Figure 24: Cooling curves and cooling rates for the two parallels of reference and inoculated T.A. cup samples.

The macrostructures of the T.A. cup samples are presented in Figure 25. In the reference sample, a thin layer of refined equiaxed grains is observed at the top near the black dot representing the sample's surface, near the mould wall. Larger columnar grains are then

dominating the structure. For the inoculated sample in Figure 25b, the solidification structure is dominated by smaller equiaxed grains, indicating equiaxed growth of grains in the sample with EGR.

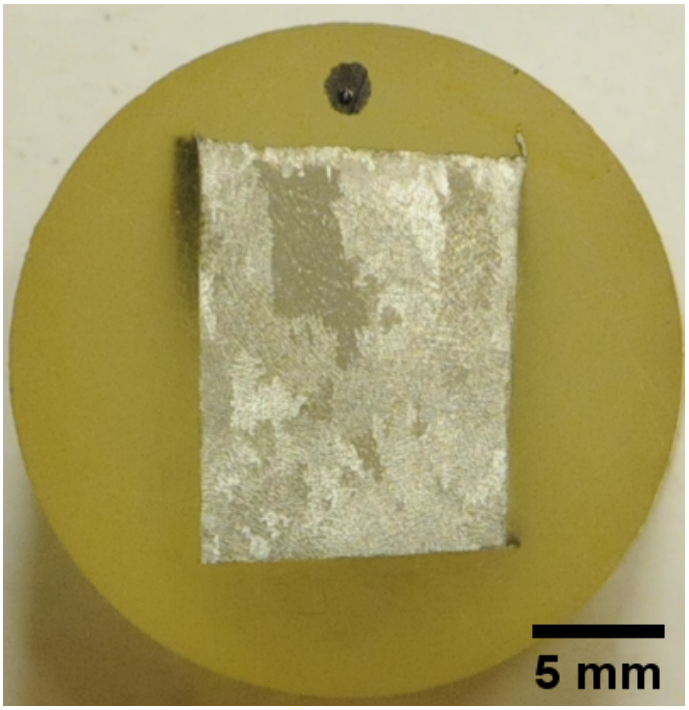

(a) Macro T.A.cup, reference.

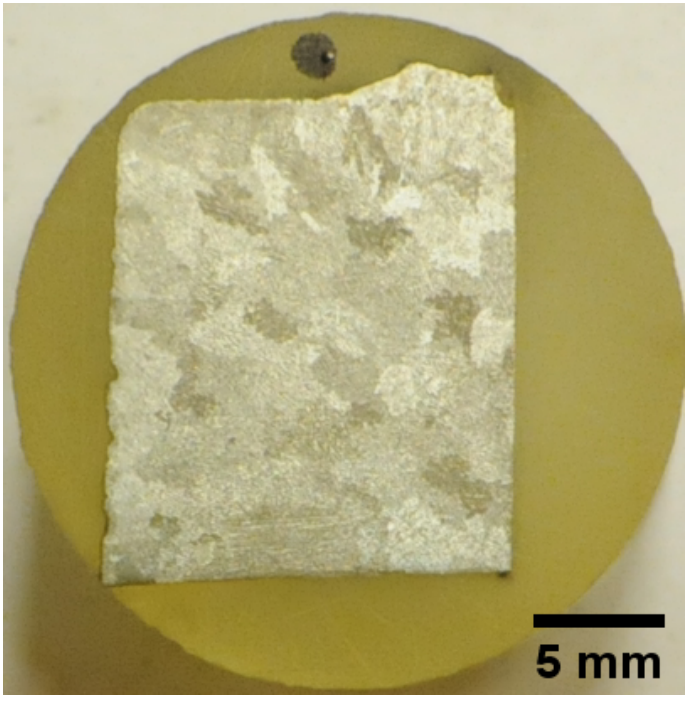

(b) Macro T.A. cup, inoculated.

Figure 25: Images of the reference and inoculated T.A. cup samples, respectively. The black dot indicates the surface of the sample.

Figure 26 shows the microstructures of the V2A-etched T.A. cup samples with and without EGR addition acquired by Light Optical Microscopy. The images were captured near the center of the samples. These micrographs provide a suitable basis for studying the impact of grain refiners on dendrite arms compared to macrostructures. By utilizing the V2A etching procedure, the dendritic structure of the samples is visible. In Figure 26a, the microstructure of the reference T.A. cup sample without cerium is presented. It consists of coarser columnar dendrites accompanied by coarse secondary dendrite arms. Figure 26b shows the microstructure of the inoculated T.A. cup sample. In this case, the microstructure displays much finer dendrite arms. Only a small portion of the image exhibits columnar dendrites, confirming equiaxed grain growth in the sample. Furthermore, the figure reveals darker phases present between the dendrites, which are likely interdendritic δ-ferrite. In the inoculated casting, the δ-ferrite are more dispersed.

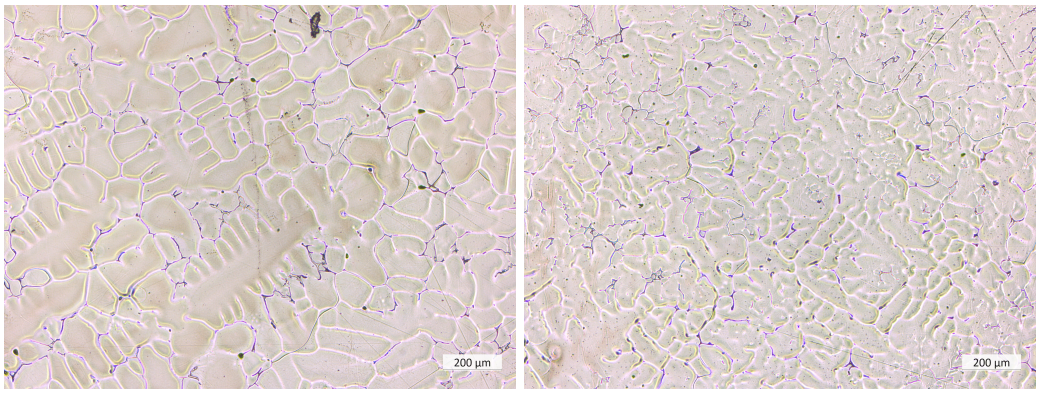

(a) Reference T.A. cup (b) Inoculated T.A. cup

Figure 26: Light Optical Microscopy image of the center region of V2A-etched T.A. cup samples.

In Figure 27, a stitched LOM image of the reference and inoculated T.A. cup samples are presented. The images show the solidification structure of the etched T.A. cups from the surface to the center of the cups. As shown in Figure 27a, the reference sample is composed of long columnar dendrites. Figure 27b shows the solidification structure of the inoculated sample. Though some regions appear as columnar dendrites, they are significantly refined compared to the reference sample.

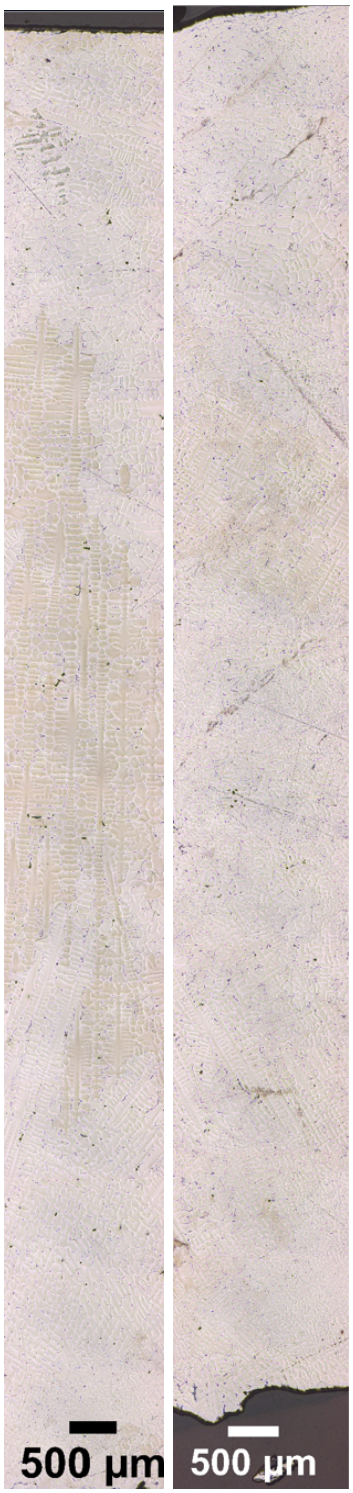

(a) Reference (b) Inoculated

Figure 27: Stitched LOM images of reference and inoculated T.A. cup samples.

The results of the LOM analysis of the T.A. cup samples are presented in Table 12. The table shows the results of the LOM analysis of the T.A. cup samples showing the columnar characteristics of the reference and inoculated sample in addition to the percentage of reduction for the inoculated sample compared to the reference. As can be seen, inoculation

has significantly reduced the length of columnar dendrites and SDAS.

Table 12: Measured secondary dendrite arms spacing(SDAS) and length of columnar dendrites.

	SDAS	**Longest grain**	**Tot. length of col. zone**
T.A. cup ref.	$82.5\mu m$	$6324\mu m$	$9836\mu m$
T.A. cup inoc.	$60.3\mu m$	$1783\mu m$	$3927\mu m$
Reduction	27%	72%	60%

Large-area EBSD maps were also acquired for the thermal-analysis-cup samples. The EBSD map of the reference sample in Figure 28 shows a significant degree of columnar grains, with nearly all the grains being elongated. Some equiaxed grains are only observed near the center. Measurements from ImageJ show that the longest columnar grain in the reference T.A. cup sample was $9379\mu m$.

Figure 28: EBSD map of thermal analysis cup sample without EGR.

Figure 29 shows the EBSD map for the inoculated thermal analysis cup sample. The grain structure is dominated by equiaxed grains, with some columnar grains at the surface region of the sample.

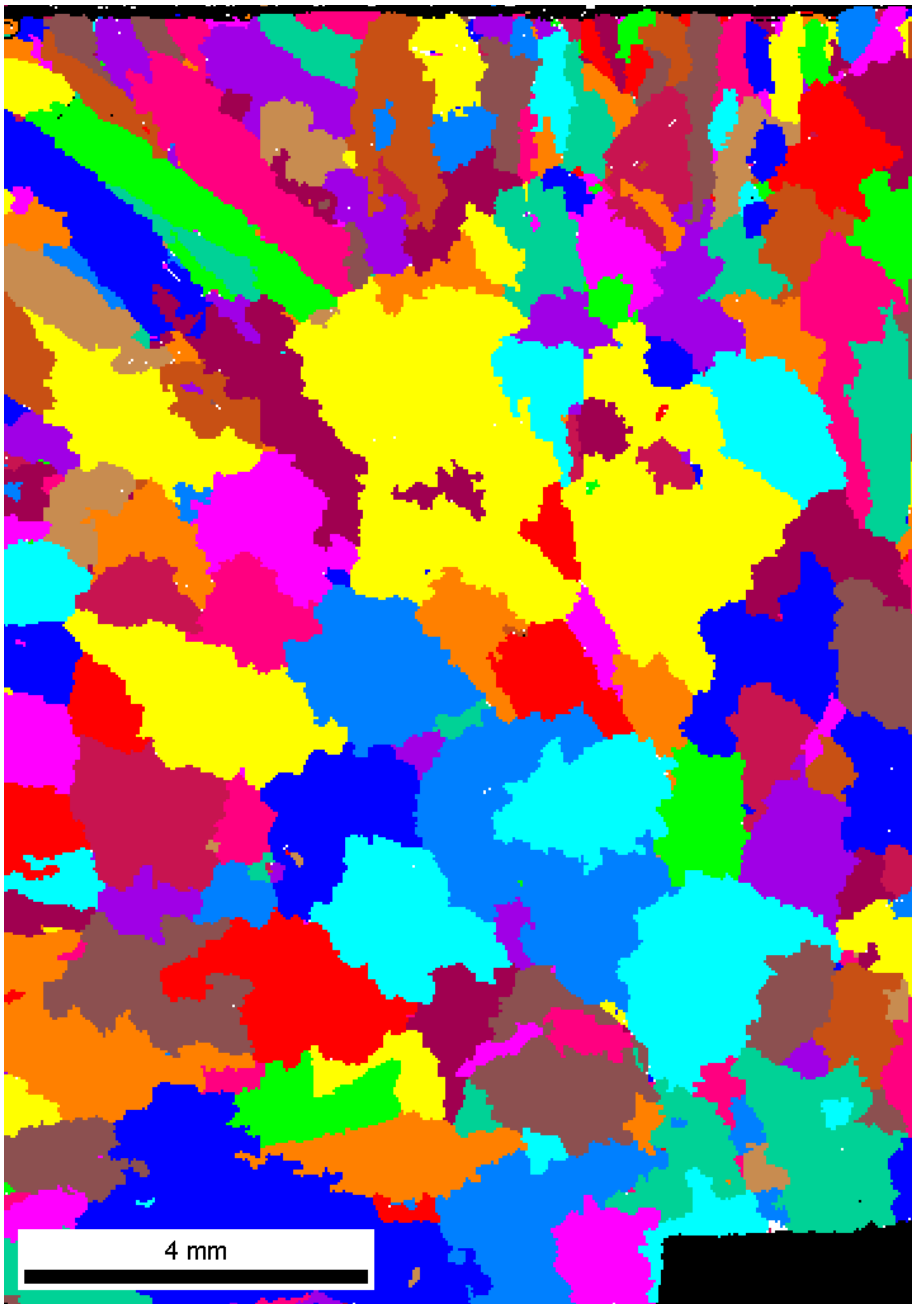

Figure 29: EBSD map of thermal analysis cup sample with EGR.

4.4 Grain refinement analysis of Y-block castings

Macro structures of the Y-block samples are shown in Figure 30. Figure 30a shows the uninoculated reference sample. Here, the solidification structure is dominated by long columnar grains spreading from the surface into the center of the block. Tendencies of shrinkage porosity are also observable at the top of the casting. Equiaxed grains dominate the inoculated sample's structure, as shown in Figure 30b. A significant reduction in the length of the columnar grain zones can be observed.

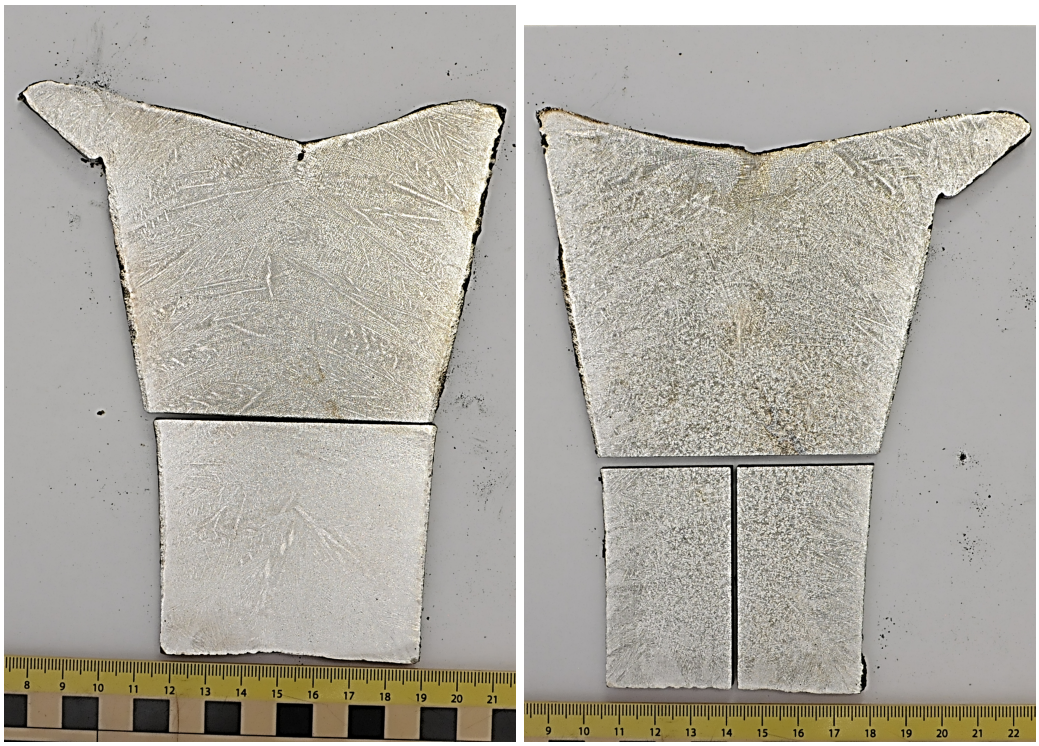

(a) Macro Y-block, reference. (b) Macro Y-block, Inoculated.

Figure 30: Images of reference and inoculated macro-etched Y-block samples, respectively.

Figures 31 and Figure 32 show the resulting large-area EBSD orientation maps for the inoculated and reference samples, respectively. Large elongated grains dominate the grain structure of both samples. An apparent cooling rate effect on the grain structure is observed for the corner region of the reference sample while not being as apparent in the inoculated Y-block sample. In the lower right corner of Figure 31, much finer columnar grains can be observed.

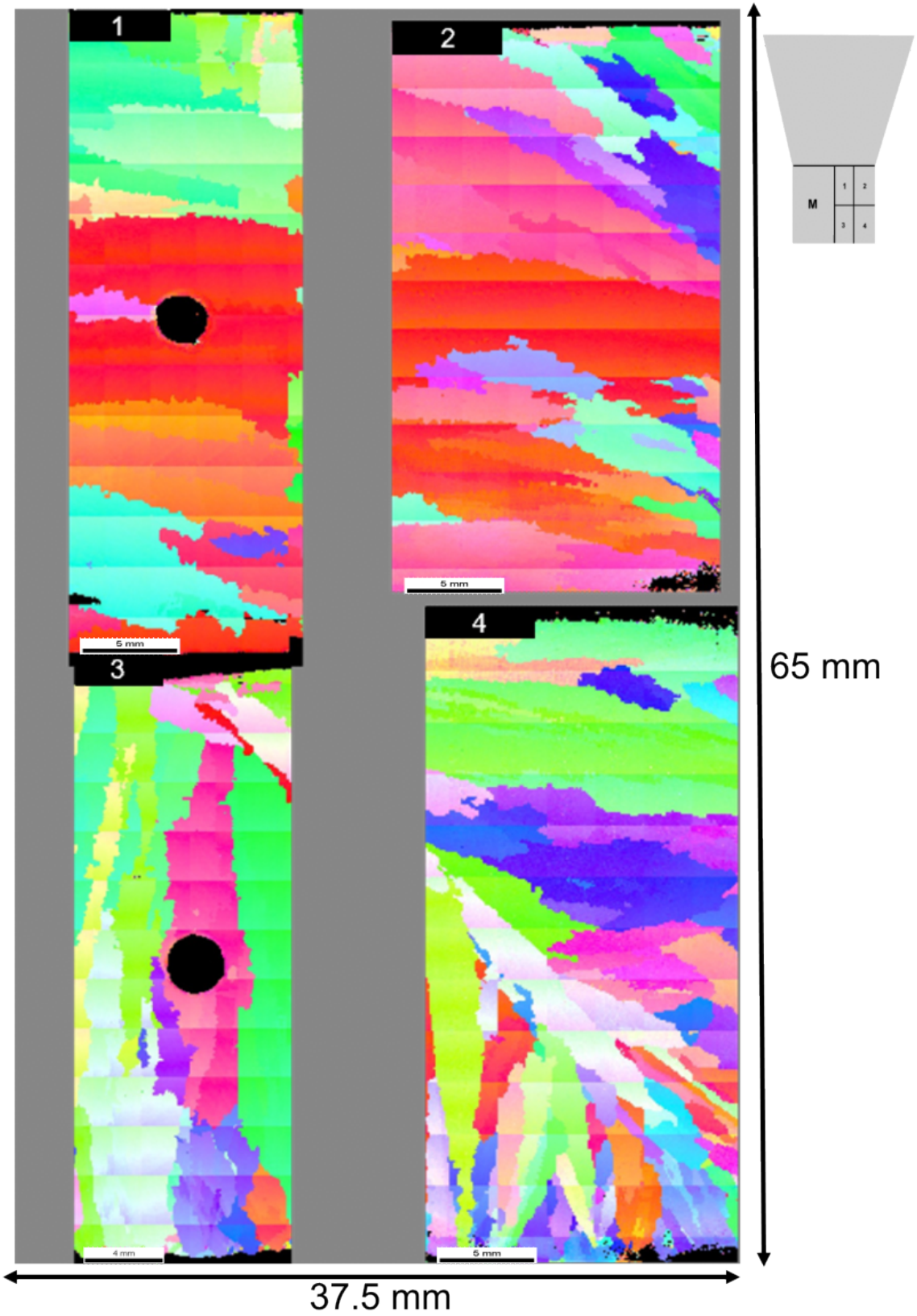

Figure 31: EBSD map of Y-block reference sample. The numbering 1-4 corresponds to the location of each sample on the Y-block seen in Figure 20.

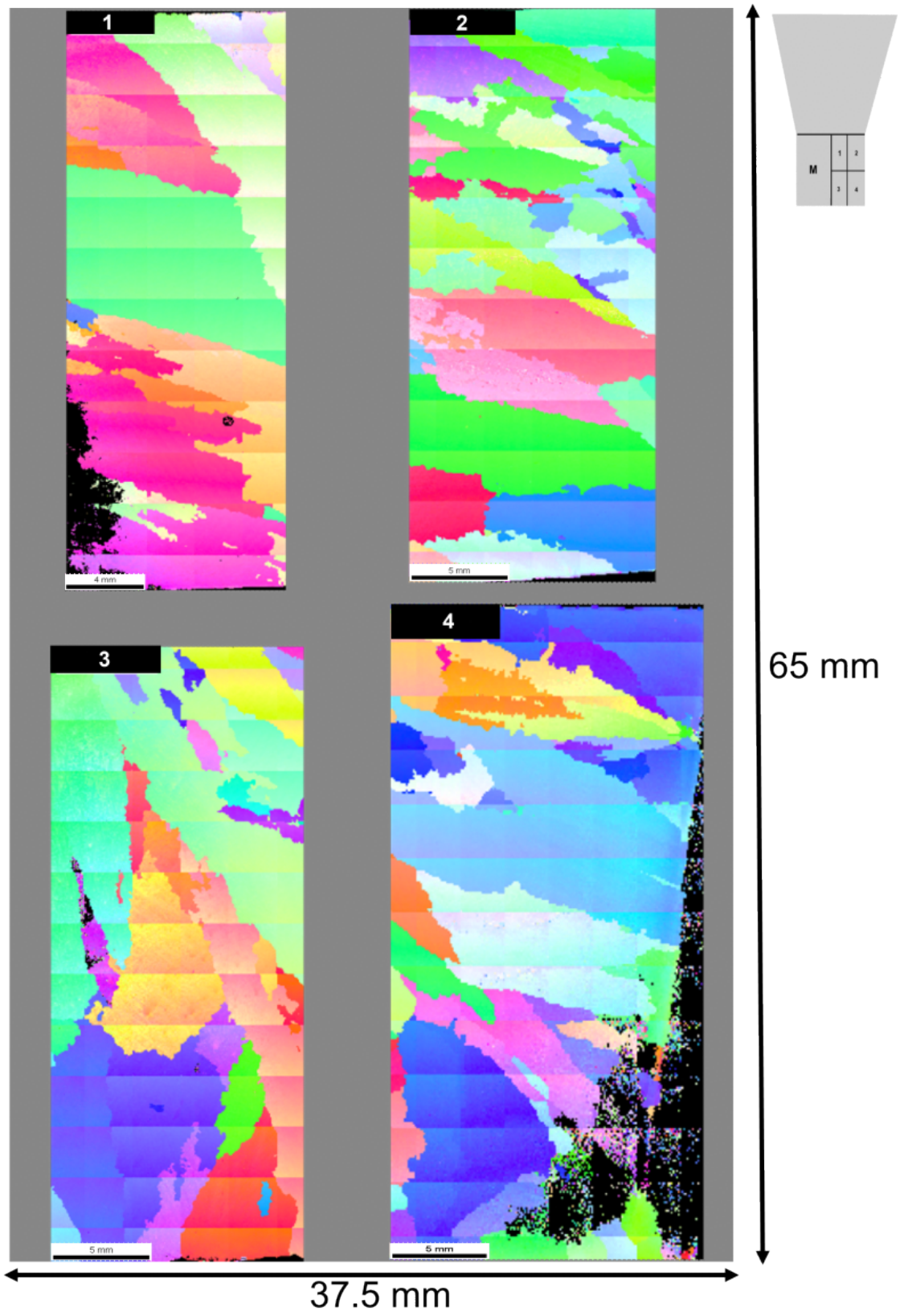

Figure 32: EBSD map of Y-block sample with EGR. The numbering 1-4 corresponds to the location of each sample on the Y-block seen in Figure 20.

4.5 SEM/EDX analysis of particles and phases

4.5.1 Particles and intermetallic phases in Ce-free alloy

The particles and phases in the reference sample before the addition of EGR were characterized. Aluminum oxides were the most abundant particles in the reference sample. Figure 33 show a gathering of Al_2O_3 particles in the reference sample, showing both needle and blocky morphologies.

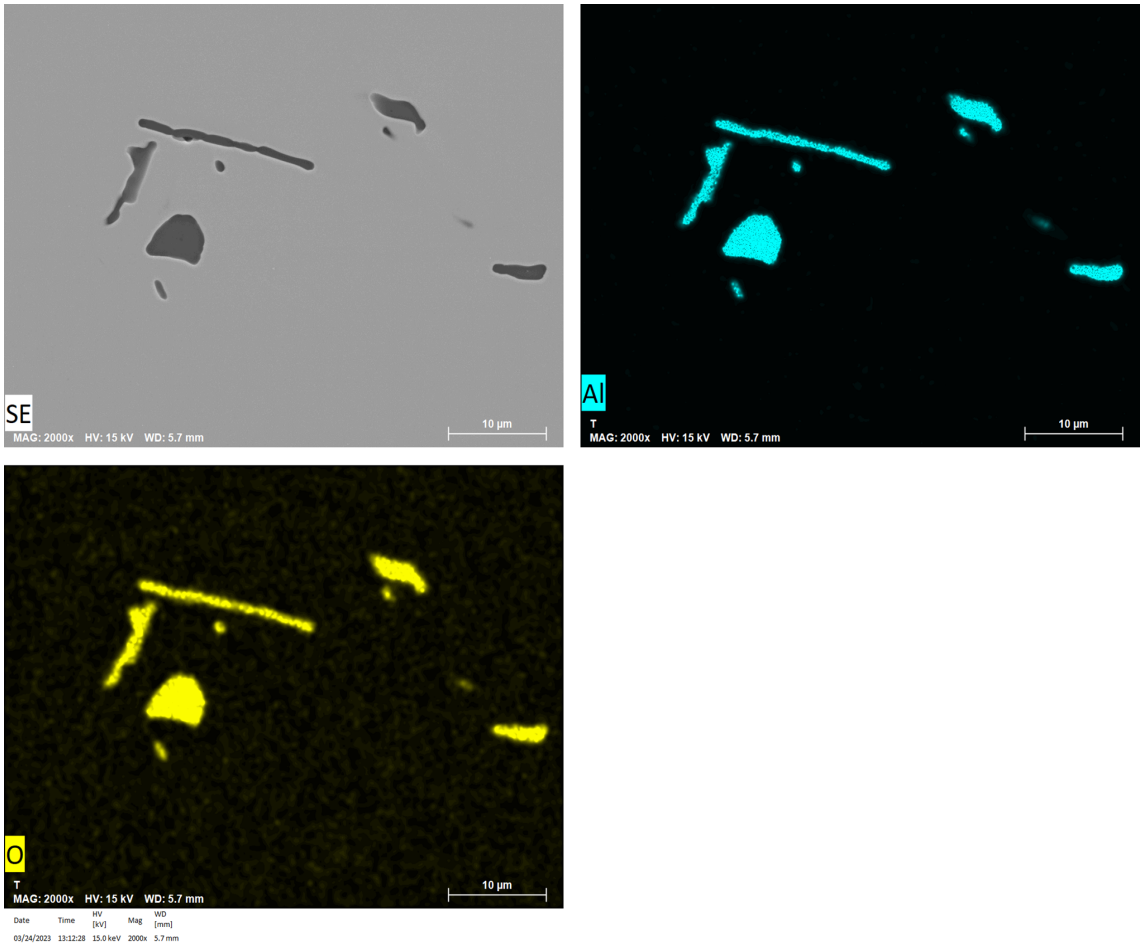

Figure 33: SEM image of Al_2O_3 particles in the reference Y-block sample with corresponding elemental mapping by EDX

Some pure manganese sulfides were also encountered. In Figure 34, a MnS particle can be observed. Such inclusions were small in size and were often found along grain boundaries. Contrary to the Al_2O_3 inclusions, the MnS particles have globular and hexagonal shapes and are considerably smaller than the Al_2O_3 particles.

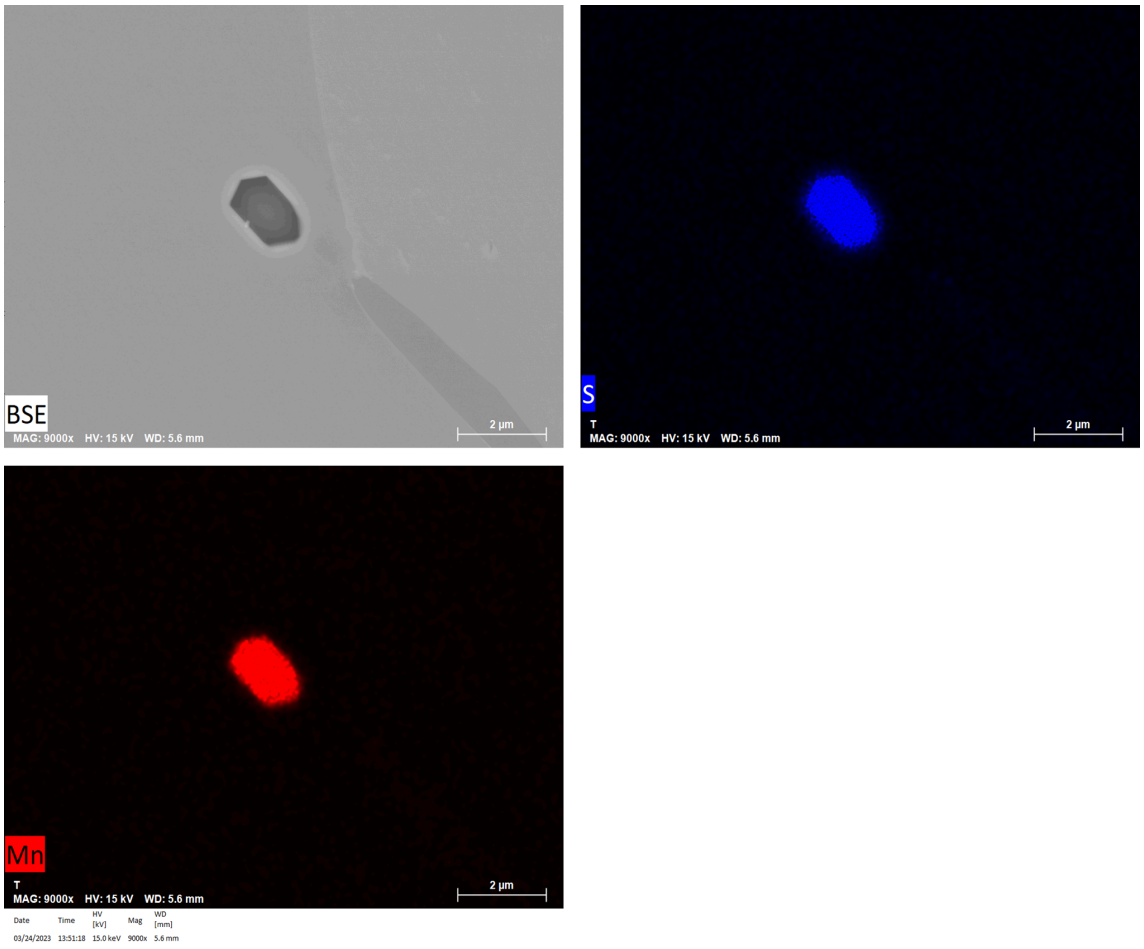

Figure 34: SEM image of a MnS particle in the reference Y-block sample with corresponding elemental mapping by EDX.

MnS particles were in some cases found combined with Al_2O_3 particles as seen in Figure 35. Here, an Al_2O_3 particle and MnS inclusion have coalesced along a grain boundary. The phenomenon was also observed in combination with intermetallic phases. This can be observed in Figure 36. As can be observed, an Al_2O_3 inclusion, surrounded by MnS is in the center of an area containing intermetallic phases.

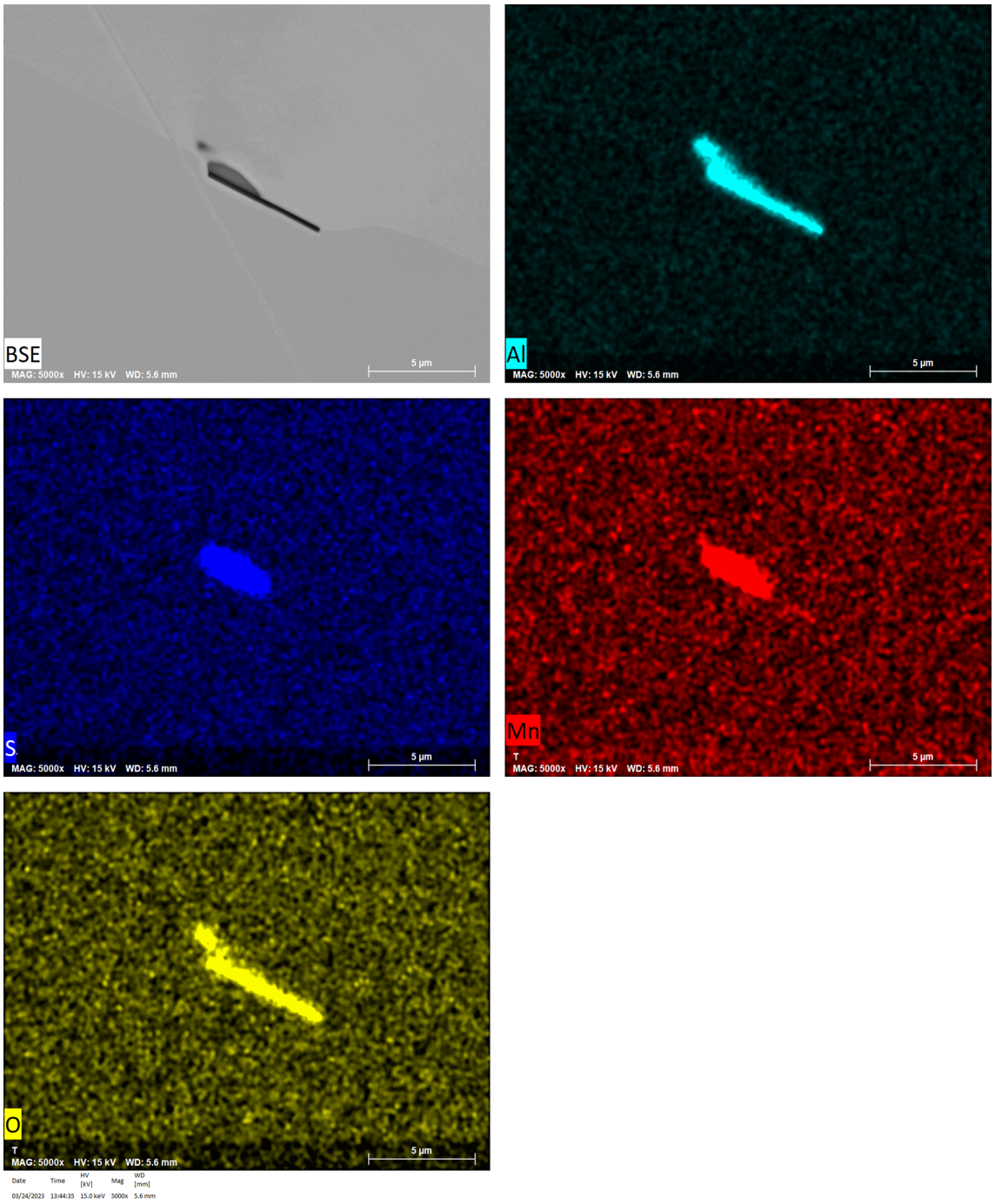

Figure 35: Compound particle composed of MnS and Al_2O_3 particles in reference Y-block sample.

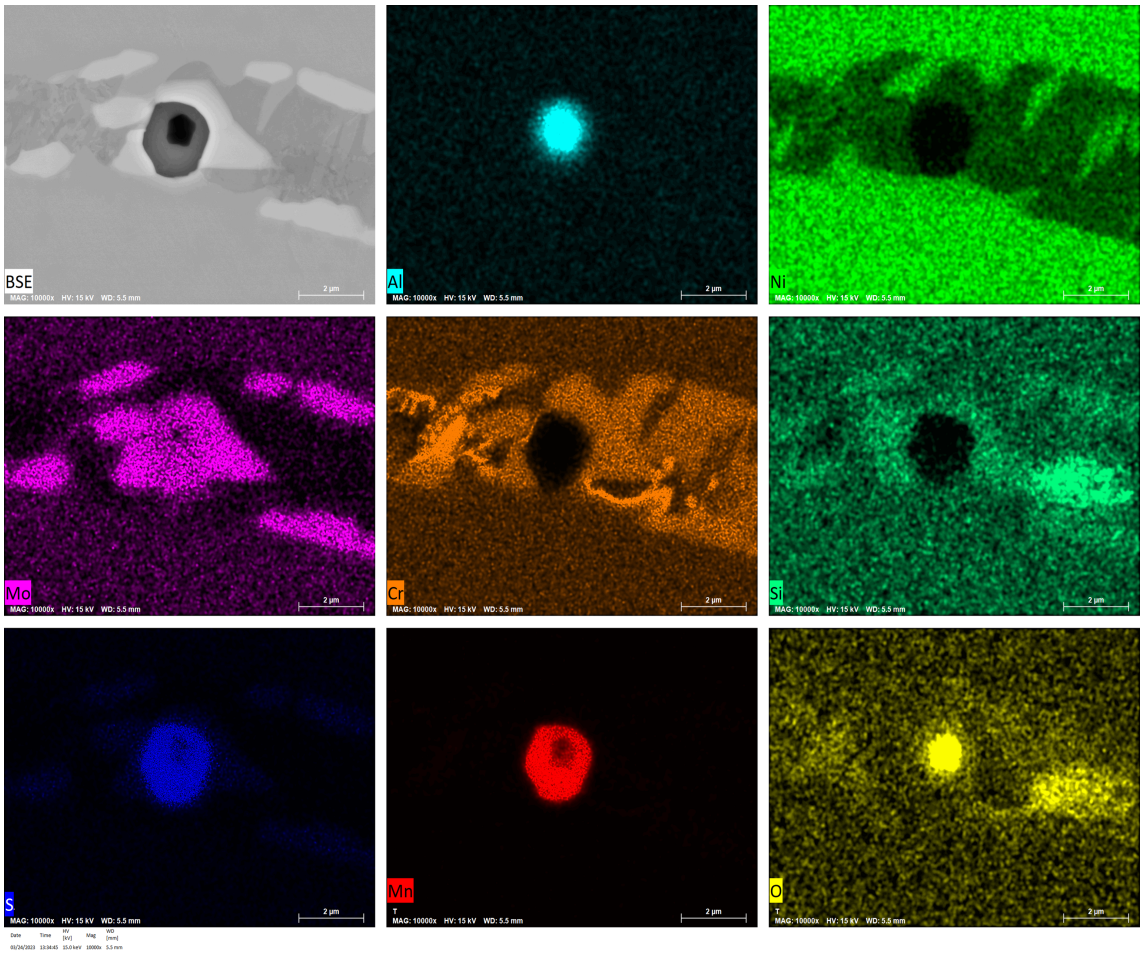

Figure 36: EDX elemental mapping of layered MnS and Al_2O_3 particles within an intermetallic phase in the reference Y-block sample.

Intermetallic phases in the reference and inoculated samples were also analyzed. Figure 37 shows a chromium- and molybdenum-rich secondary phase in the reference sample. The phases around the layered particle in Figure 36 differs in composition compared to the one in Figure 37 by also containing Si. The intermetallic phases are depleted in nickel compared to the surrounding matrix, but are enriched in molybdenum and chromium.

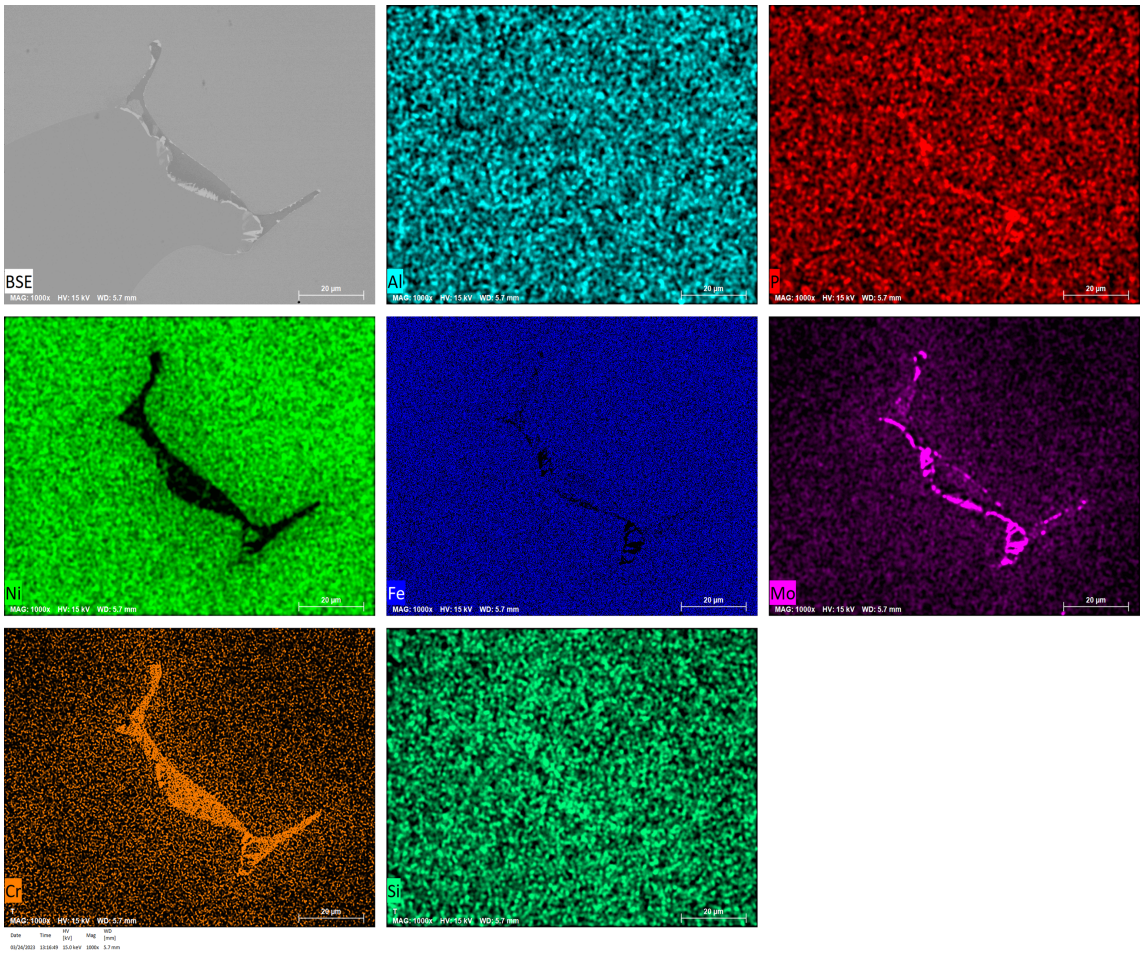

Figure 37: BSE image and EDX elemental mapping of an intermetallic phase from the reference Y-block sample.

To acquire the specific compositions of the observed phases, EDX spectra were analyzed. Figure 38 shows areas containing intermetallic phases in the reference Y-block sample. The composition of each phase observed was measured with EDX. The resulting compositions of the EDX shot sites seen in Figure 38 are presented in Table 13 and 14. It can be observed that the phases analyzed differ in their compositions, indicating the presence of several types of intermetallic phases. Especially the contents of Mo, Ni, and Cr varies between the phases.

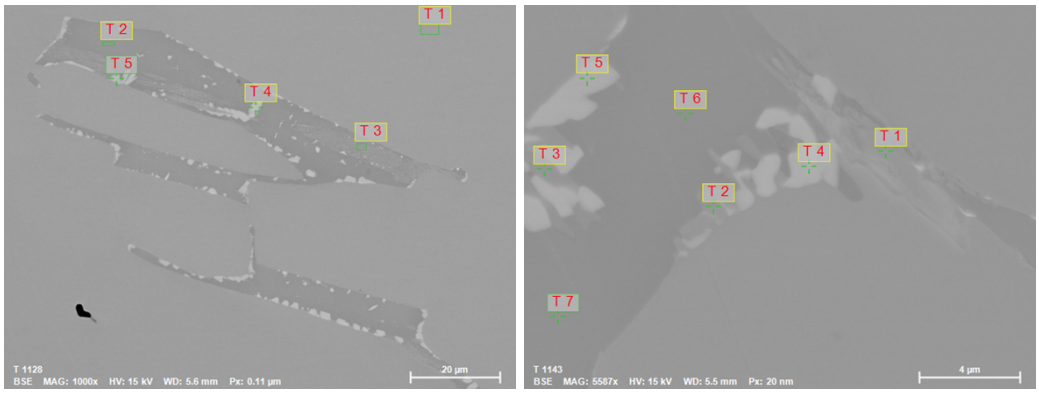

(a) (b)

Figure 38: SEM images of intermetallic phases in uninoculated Y-block sample.

Table 13: Measured composition from EDS analysis of Figure 38a. Values are given in weight percent.

Spectrum	Si	P	Cr	Fe	Ni	Mo
T1	0.93	0.25	24.86	61.20	6.21	6.55
T2	0.83	0	25.89	63.33	5.34	4.61
T3	0.76	0	18.73	65.62	11.89	2.99
T4	1.30	0.60	26.24	51.29	3.89	16.68

Table 14: Measured composition from EDS analysis of Figure 38b. Values are given in weight percent.

Spectrum	Si	P	Cr	Fe	Ni	Mo
T1	1.25	0.52	26.62	53.07	4.11	14.43
T2	1.12	0.43	27.09	52.82	4.27	14.26
T3	0.93	0.18	26.05	62.21	5.35	5.29
T4	0.92	0.16	26.17	62.17	5.07	5.49
T5	0.74	0	18.57	65.00	12.55	3.15

4.5.2 Inoculated sample

EDX mapping and analysis of cerium inclusions in the inoculated samples were done. Table 15 lists the resulting categories of Ce-containing inclusions and possible stoichiometries. The analysis showed that cerium aluminates are the most frequent inclusions, followed closely by cerium oxides. The sulfides and oxysulfides were found in considerably less amounts.

Much larger multiphased Ce-containing inclusions was also encountered during the analysis of the inoculated Y-block samples. Figures 39a, 39b, 39c and 39d are examples of how

they look like. In most cases, cerium aluminate is enveloped by cerium oxide, especially in Figure 39b and Figure 39c. Opposite cases were also encountered, however, to a much smaller degree.

The cerium sulfides and oxysulphides were often found at the edges of the larger inclusions.

Table 15: Possible stoichiometry of cerium-compounds encountered during EDX analysis.

Class	**Oxides**	**Sulphides**	**Aluminates**	**Oxysulphide**
Possible compound	CeO, CeO_2, Ce_2O_3	CeS	$CeAlO_3$	Ce_2O_2S

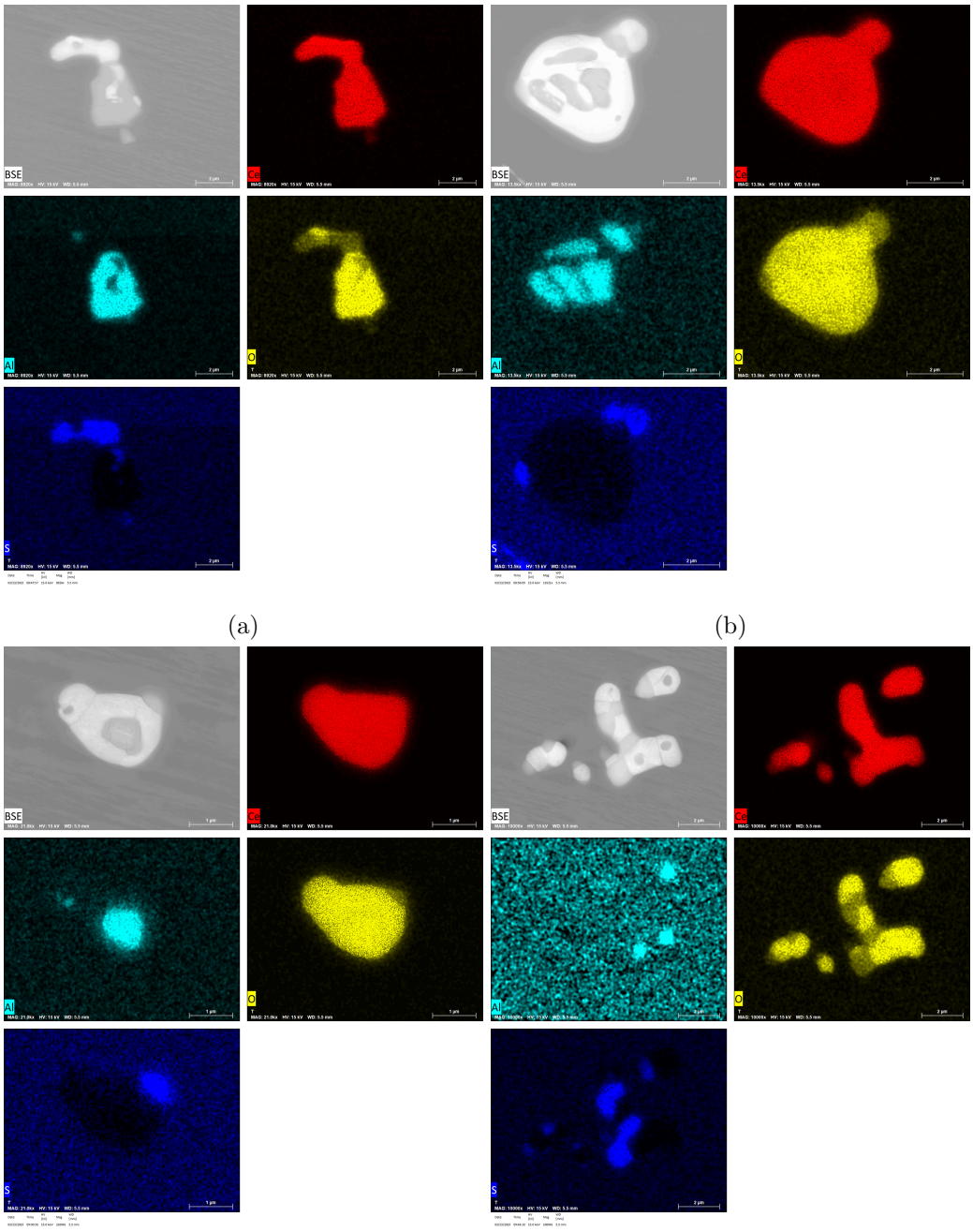

Figure 39: SEM images and EDX elemental mapping of Ce-containing inclusions from inoculated Y-block. Ce in red, Al in light blue, O in yellow, and S in blue.

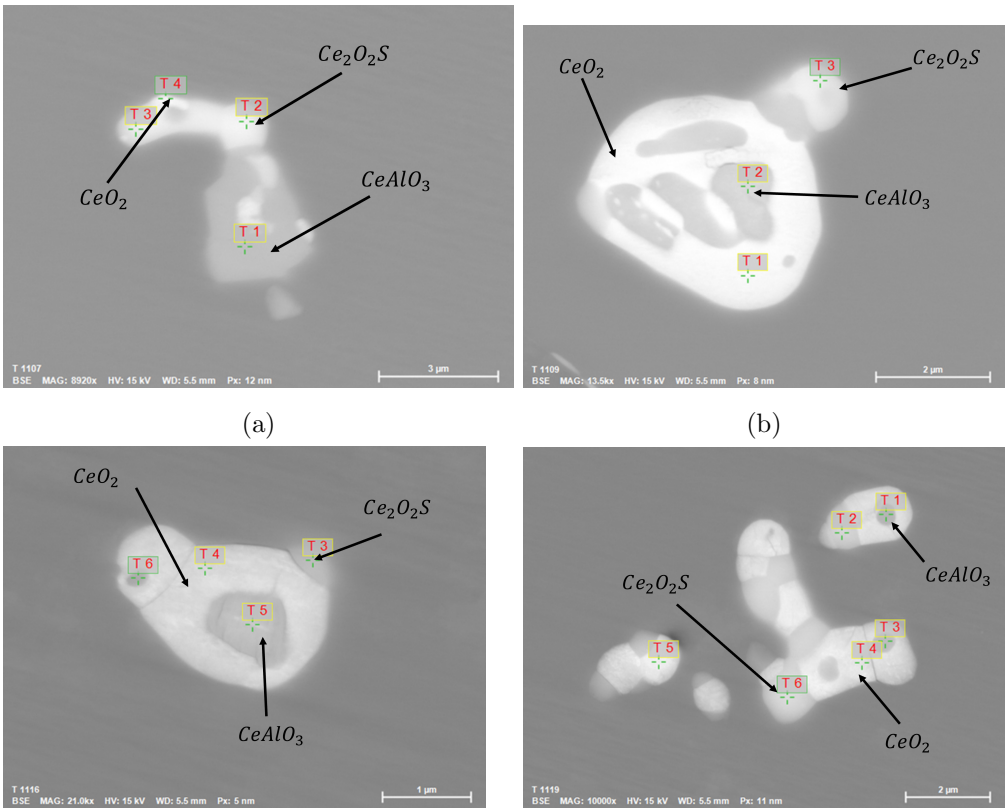

Figure 40: EDX shot sites and corresponding cerium inclusions.

Tables 16,17,18 and 19 show the measured chemical compositions of different inclusion phases in Figure 39. The compositions document the presence of $CeAlO_3$, Ce_2O_2S and CeO_2.

Table 16: Composition from EDX analysis of the particle seen in Figure 40a with trace elements removed. Values are given in atomic percent.

Spectrum	Ce	Al	O	S
T1	19.38	19.93	60.96	
T2	38.41		43.67	17.92
T3	35.94		46.52	17.53
T4	33.97		64.19	1.84

Table 17: Composition from EDX analysis of the particle seen in Figure 40b with trace elements removed. Values are given in atomic percent.

Spectrum	Ce	Al	O	S
T1	37.2		62.8	
T2	26.9	11.4	61.7	
T3	40.5		52.7	6.9
T4	33.97		64.19	1.84

Table 18: Composition from EDX analysis of the particle seen in Figure 40c with trace elements removed. Values are given in atomic percent.

Spectrum	Ce	Al	O	S
T3	35.83		52.25	11.93
T4	32.09		67.91	
T5	26.51	9.71	63.78	
T6	30.85	5.70	63.46	

Table 19: Composition from EDX analysis of the particle seen in Figure 40d with trace elements removed. Values are given in atomic percent.

Spectrum	Ce	Al	O	S
T1	31.73	8.06	60.21	
T2	38.14		52.07	9.79
T3	28.97	6.52	28.97	
T4	33.35		66.65	
T5	34.69		64.13	1.18
T6	37.82		44.11	18.07

The inoculated sample also contains inclusion particles and intermetallic phases. However, the amount of these phases is much smaller. Additionally, more types of secondary phases were encountered during the analysis of the reference sample compared to the inoculated sample. Figure 41 show an intermetallic phase encountered in the inoculated Y-block sample. The resulting composition of EDX analysis is presented in Table 20. Here mainly two intermetallic phases can be observed in addition to the matrix. These vary greatly in their Mo content and, to some extent, their Ni and Fe content.

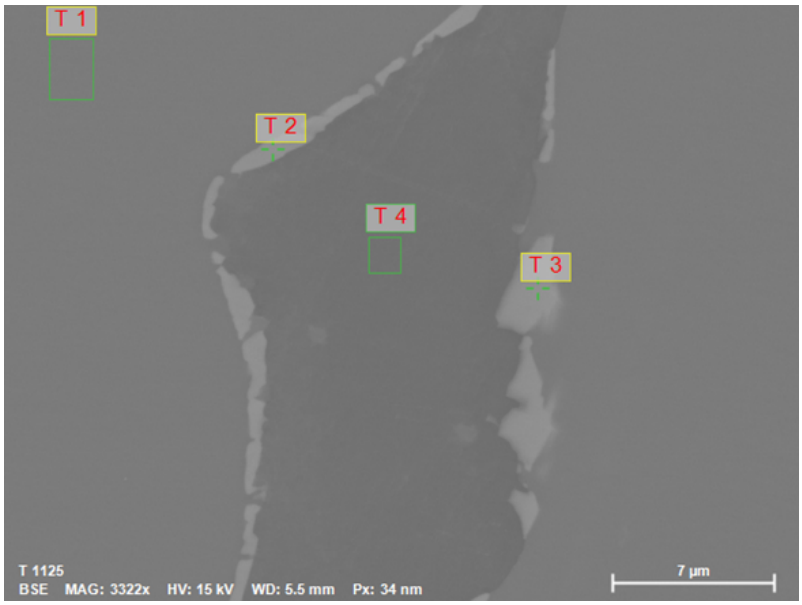

Figure 41: Intermetallic from inoculated Y-block sample.

Table 20: Measured composition from EDS analysis of Figure 41. Values are given in weight percent.

Spectrum	Si	Cr	Fe	Ni	Mo
T1	0.83	17.65	68.74	10.51	2.28
T2	1.40	27.83	54.12		16.65
T3	1.38	27.56	53.96		17.09
T4	0.87	24.24	68.01	4.47	2.40

4.6 Advanced Mineral Identification and Characterization System(AMICS)

The resulting particle count from the AMICS analysis of the samples is listed in Table 21.

Table 21: AMICS data summary: Counts of inclusions of different categories and pores.

Sample	All incl.	Sulfides	Al-oxides	Cerium incl.	Other	Pores
T.A. cup ref.	2203	27	1395	0	811	991
T.A. cup inoc.	11939	0	1	11683	255	280
Y-block ref.	1837	59	1705	0	54	794
Y-block inoc.	6386	0	0	6287	99	117

From the analysis of the AMICS data in ImageJ, each category of microparticles and pores can be sorted after their feret diameter. Figure 42 shows the size and morphology of Al_2O_3 particles detected in the reference T.A. cup and Y-block samples during scanning. Most of the Al_2O_3 inclusions have long and needle-shaped morphology with sharp edges.

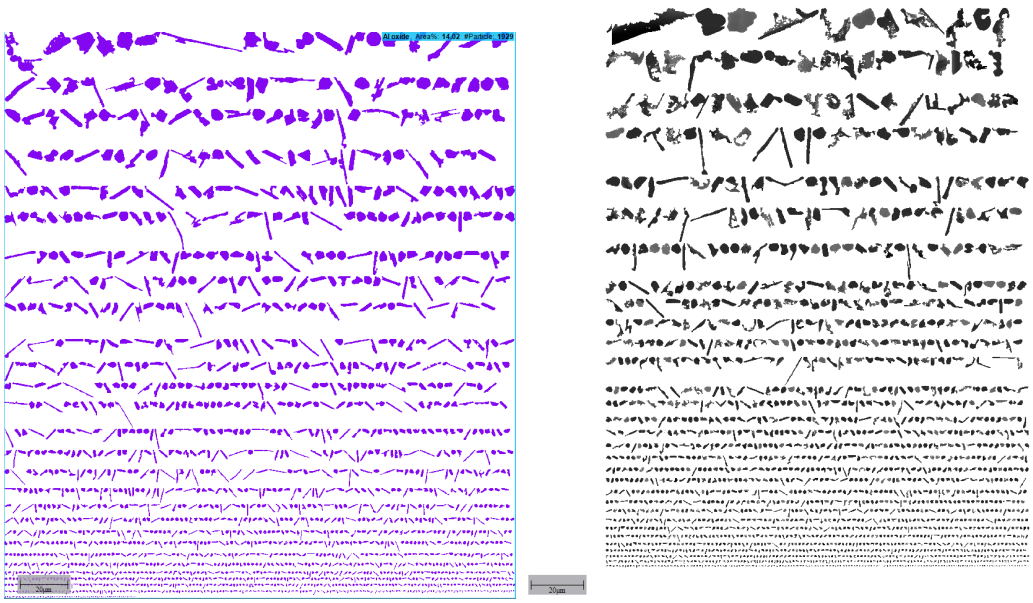

(a) T.A. cup (b) Y-block

Figure 42: Morphology for Al_2O_3 inclusions in the reference T.A. cup and Y-block samples.

The morphology of the Ce-bearing inclusions in the inoculated samples is presented in Figure 43. The shape of the inclusions is mainly round but varies to some degree. The "holes" in the middle of the particles represent a different phase due to contrast differences.

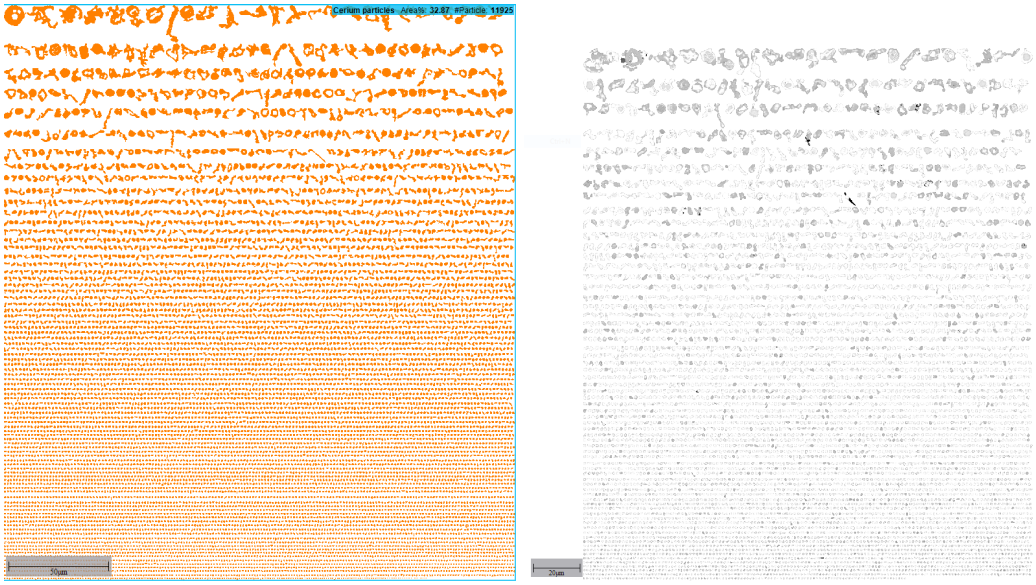

(a) T.A. cup (b) Y-block

Figure 43: Morphology of Ce-bearing inclusions in the inoculated T.A. cup and Y-block samples.

Particles in the category "Other" were logged as well during the scanning. The morphology of these inclusions is presented for the reference and inoculated T.A. cups in Figure 44

and in Figure 45 for the Y-block samples. More of these particles were documented in the T.A. cup samples than in the Y-blocks, in which few were found. A lower number of other particles in the inoculated T.A. cup sample than in the reference can also be observed.

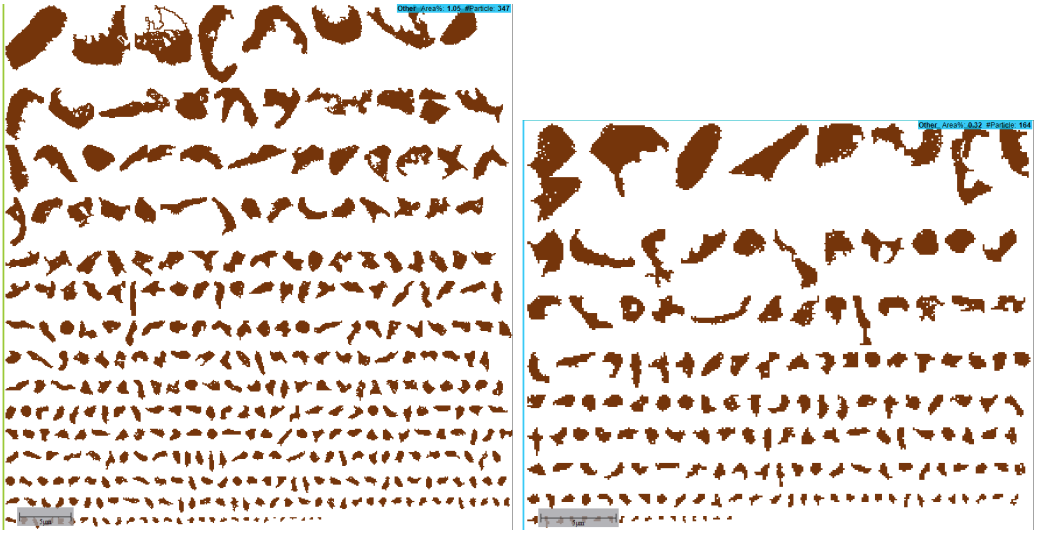

(a) Reference T.A. cup (b) Inoculated T.A. cup

Figure 44: Uncharacterized/other inclusions in the reference and inoculated T.A. cup samples.

(a) Reference Y-block (b) Inoculated Y-block

Figure 45: Uncharacterized/other inclusions in the reference and inoculated Y-block samples.

Figures 46 and 47 show the number and shape of the pores detected by the AMICS analysis. The pores in the T.A. cups were more elongated compared to the pores in the Y-block, which were more round in their shape. A clear reduction in the number of pores can be observed for both the T.A. cup and the Y-block samples with the addition of EGR.

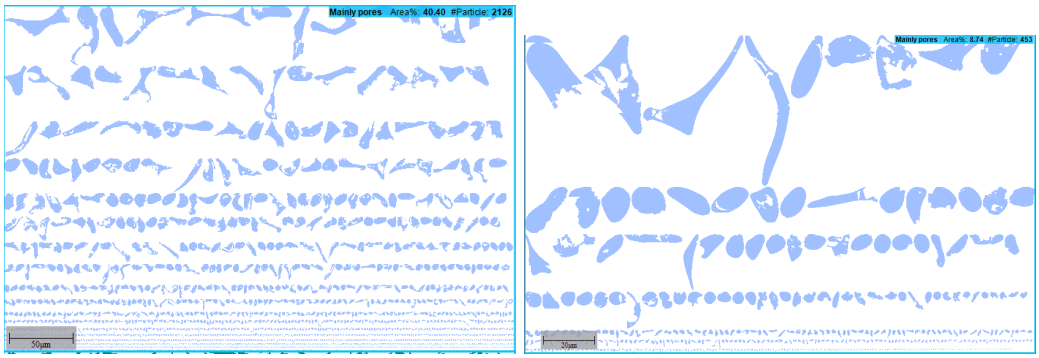

(a) Reference T.A. cup (b) Inoculated T.A. cuo

Figure 46: Pores in the reference and inoculated T.A. cup samples.

(a) Reference Y-block (b) Inoculated Y-block

Figure 47: Pores in the reference and inoculated Y-block samples.

4.7 Particle distributions

The particle distributions were based on the feret diameters measured with ImageJ particle analysis.

4.7.1 2D distributions

The 2D distributions are based on the raw data from the particle analysis. Figure 48 shows the particle size distributions for the reference T.A. cup sample as the number of particles per mm^2 of a given diameter. The distributions of Al_2O_3(Figure 48a) and all inclusion(Figure 48b) show that most of the particles are in size range 1-4μm.

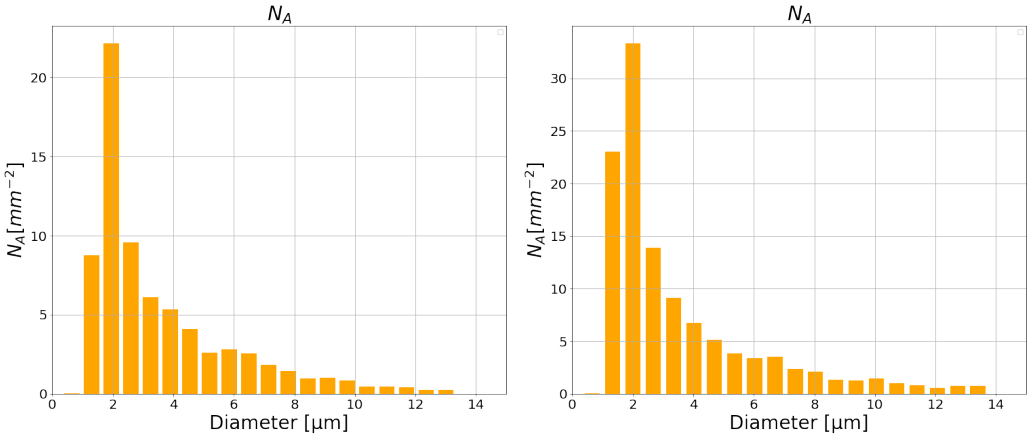

(a) Al_2O_3 inclusions (b) All inclusions

Figure 48: Number density in mm^{-2} as a function of particle diameter(μm) for T.A cup reference sample.

In Figure 49, the 2D particle distributions of the reference Y-block sample are illustrated. The number of Al_2O_3 particles is greater than in the T.A. reference sample. The number of all inclusions remains approximately alike.

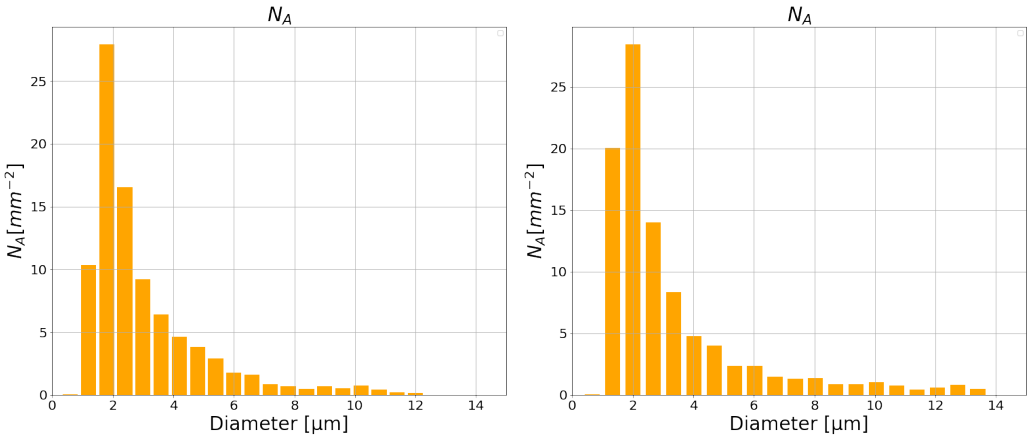

(a) Al_2O_3 inclusions (b) All incluisions

Figure 49: Number density in mm^{-2} as a function of particle diameter(μm) for Y-block reference sample.

In Figure 50, the 2D particle distributions of the inoculated T.A. cup sample are illustrated. Most cerium inclusions have a diameter of 1-3 μm. It can be seen from the distributions that the cerium inclusions match the number of all inclusions.

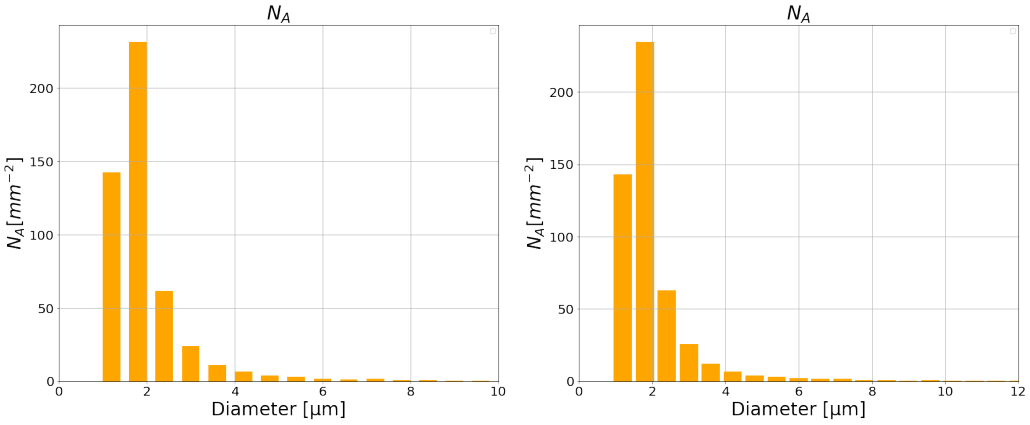

(a) Cerium inclusions (b) All inclusions

Figure 50: Number density in mm^{-2} as a function of particle diameter(μm) for T.A. cup inoculated sample.

In Figure 51, the 2D particle distributions of the inoculated Y-block sample are shown. Here, the size of cerium inclusions is slightly larger than in the T.A. cup sample. The total number of cerium inclusions and the total number of inclusions are also lower than in the T.A. cup. However, the ratio of cerium inclusions and total inclusions remains the same in the two castings.

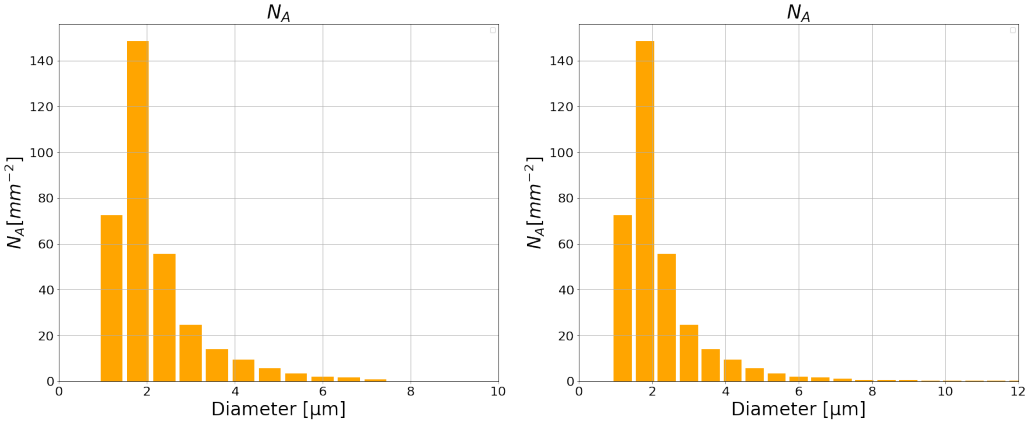

(a) Cerium inclusions (b) All inclusions

Figure 51: Number density in mm^{-2} as a function of particle diameter(μm) for Y-block inoculated sample.

4.7.2 3D distributions

Using the Finite Difference Method described in Section 2.9, the 2D distributions were converted into 3D distributions.

The number densities in mm^{-3} as a function of particle diameter for the reference T.A.

cup and Y-block samples are given in Figure 52 and Figure 53 along with a log-normal fitted curve for the distributions of Al_2O_3 and all inclusions.

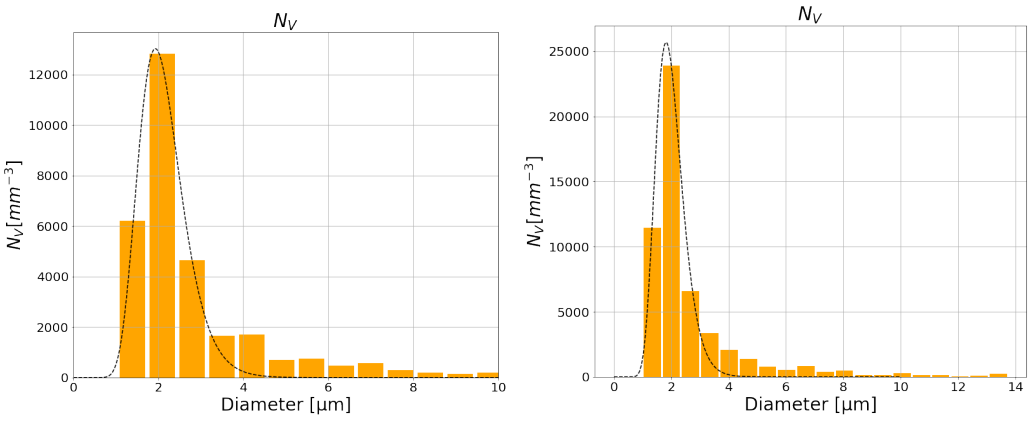

(a) Al_2O_3 inclusions (b) All inclusions

Figure 52: Number density in mm^{-3} as a function of particle diameter(μm) for T.A cup reference sample. The black lines are log-normal distributions

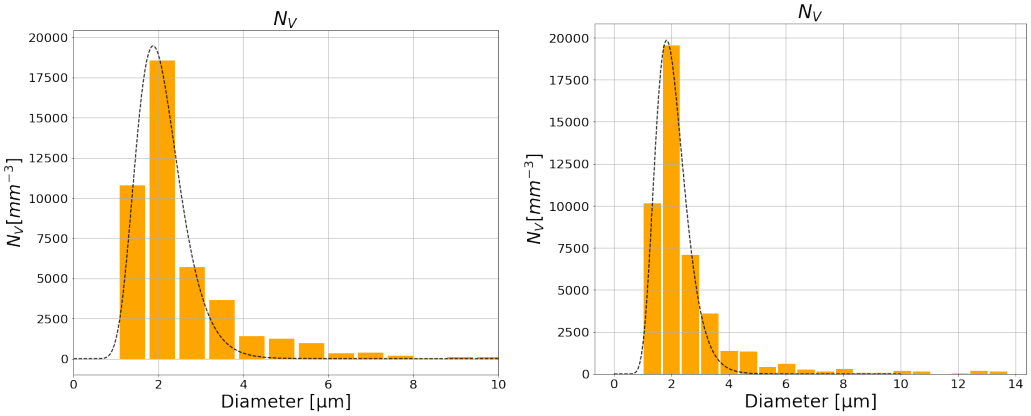

(a) Al_2O_3 inclusions (b) All inclusions

Figure 53: Number density in mm^{-3} as a function of particle diameter(μm) for Y-block reference sample. The black lines are log-normal distributions

The number densities in mm^{-3} as a function of particle diameter for the inoculated T.A. cup and Y-block samples are given in Figure 54 and Figure 55 along with a log-normal fitted curve for the distribution.

It is evident from Figure 54 that Ce-bearing particles dominate the inclusions in the T.A. cup inoculated sample. In the inoculated Y-block sample, it can be observed that the cerium particles make up the same percentage of the total inclusion number as the T.A. cup, however, with only half the particle number density. This is also evident from Table 21.

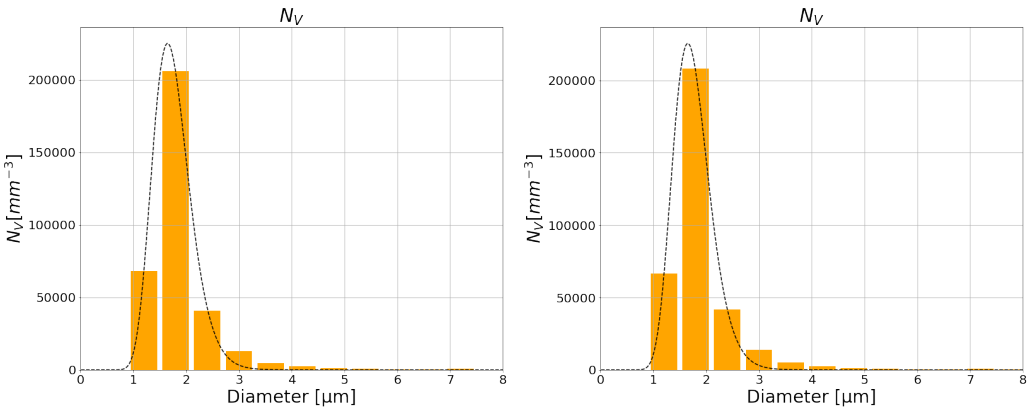

(a) Cerium inclusions (b) All inclusions

Figure 54: Number density of Ce-bearing particles in mm^{-3} as a function of particle diameter(μm) for the T.A cup inoculated sample. The black dashed lines are fitted log-normal distributions

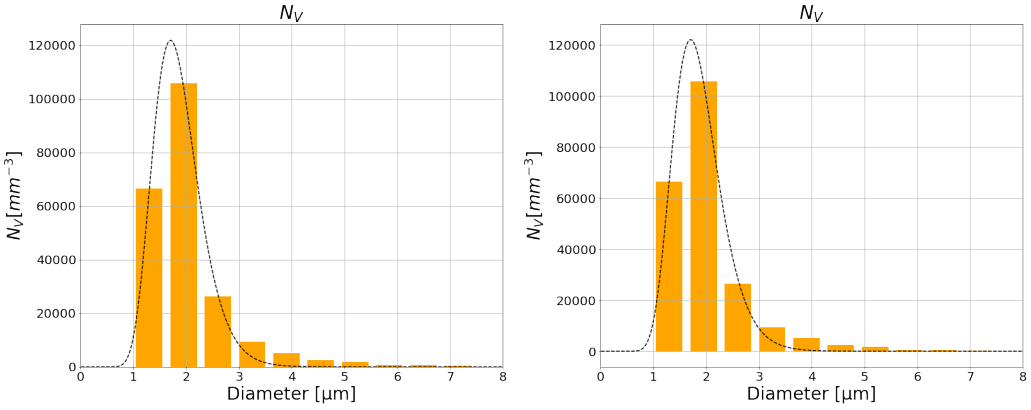

(a) Cerium inclusions (b) All inclusions

Figure 55: Number density in mm^{-3} as a function of particle diameter(μm) for the Y-block inoculated sample. The dashed black lines are fitted log-normal distributions.

In Figure 56, the fitted size distribution curves for each type of microparticle and the total number of inclusions are plotted. The plots contain the numbers of the corresponding T.A. cup and Y-block samples. As can be observed in the Figures, the number of Al_2O_3 particles in the reference sample is higher in the Y-block compared to the T.A. cup inoculated sample. However, the number of cerium particles per mm^3 is considerably higher in the T.A. cup.

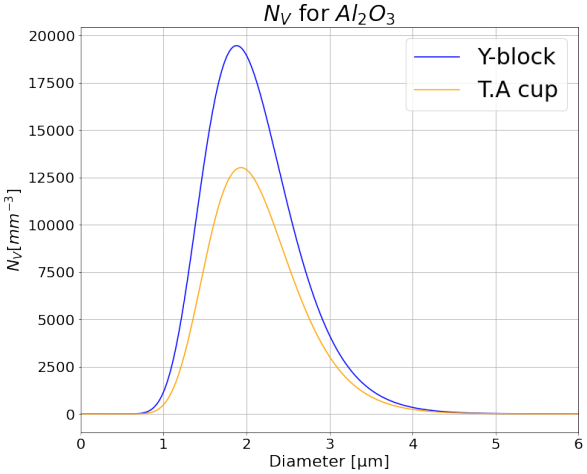

(a)

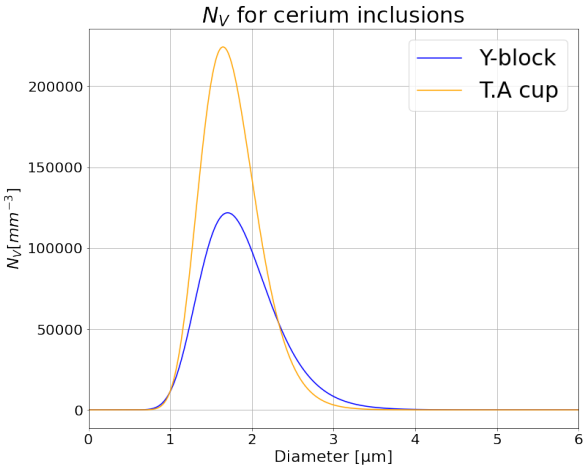

(b)

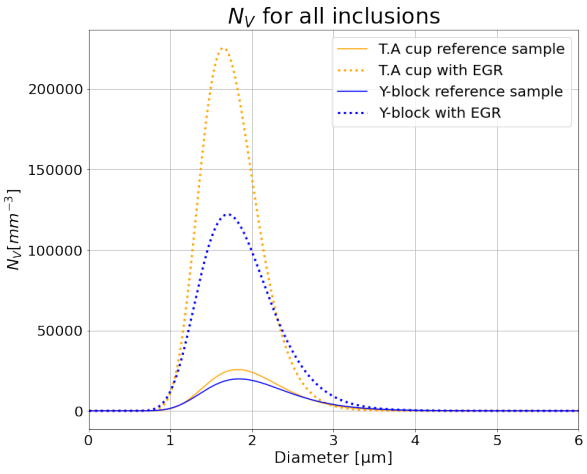

(c)

Figure 56: Fitted log-normal number density distributions of Al_2O_3 and all inclusions in the uninoculated T.A. cup and Y-block samples(56a), Ce-inclusions and all inclusions in the inoculated T.A. cup and Y-block samples(56b), and all inclusions for the reference and inoculated T.A. cup and Y-block samples(56c).

Figure 57 illustrates all inclusions and cerium inclusions for the EGR-inoculated samples. It can be observed that the cerium inclusions are the main contributor to the total number of inclusions in the samples. It is also evident that the number density of Ce-bearing inclusions is significantly decreased in the large Y-blocks compared to the small T.A. cups.

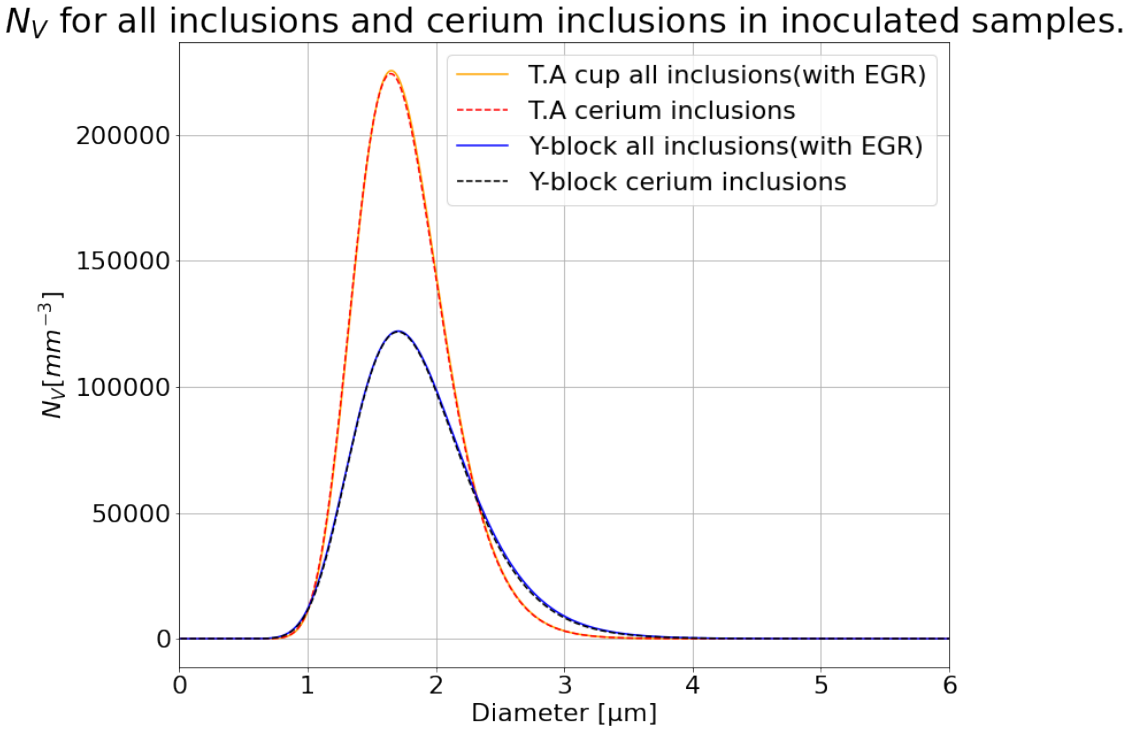

Figure 57: Log-normal distribution of all inclusions and cerium inclusions in the inoculated samples.

In Figure 58 and Figure 59, an overview image of the scanned area in AMICS with cerium particles highlighted, is shown for the inoculated T.A. cup and Y-block samples, respectively. The images show an even distribution of the cerium inclusions in the samples. Some clustering of inclusions can be observed in the T.A. cup sample.

Figure 58: Cerium inclusion overview in the scanned area of the inoculated T.A. cup. The matrix is black, while cerium inclusions are bright.

Figure 59: Overview images of Ce-bearing inclusions in the AMICS-scanned area of the inoculated Y-block. The matrix is black, while cerium inclusions are bright.

4.8 Grain size analysis and nucleation potency

The grain sizes of the T.A. cup and Y-block samples were measured, and the average grain size was calculated with the Intercept method. The results of the calculations are listed in Table 22.

Table 22: Grain size measurements based on the Intercept method in the horizontal and vertical direction of the samples. Average grain size in bold. Reduction of average grain size for the inoculated samples given in percent.

Sample	Avg. grain size horizontal dir.	Avg. grain size length dir.	Avg. grain size	Reduction
T.A cup reference	1038μm	1556μm	**1297**μm	-
T.A cup inoculated	746μm	905μm	**826**μm	36.3%
Y-block reference	5212μm	4442μm	**4827**μm	-
Y-block inoculated	4071μm	3832μm	**3951**μm	18.1%

Figure 60 shows the average grain size of the reference and inoculated samples of the Y-block and the T.A. cups. A refining effect was achieved for both castings, with a 36% reduction of the average grain size in the T.A. cups and an 18% reduction in the Y-block with the addition of EGR.

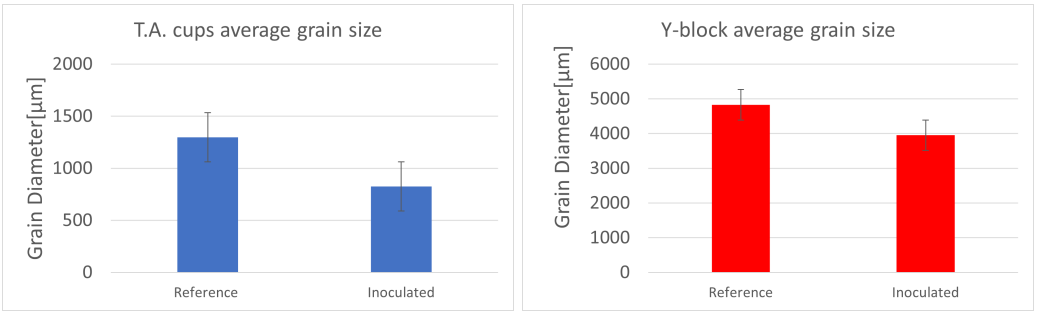

(a) (b)

Figure 60: Average grain diameter in μm for the reference and inoculated samples in the T.A cups and Y-blocks.

The two-dimensional grain size distributions in the T.A. cups based on ImageJ analysis are presented in Figure 61. The inoculated sample consists of grains with smaller diameters compared to the reference sample. The distribution also shows a negative linear relationship between the number of grains with increasing grain size for the inoculated sample. This relationship is not observed in the distribution for the reference sample. Moreover, the uninoculated sample contains larger grains than the inoculated sample.

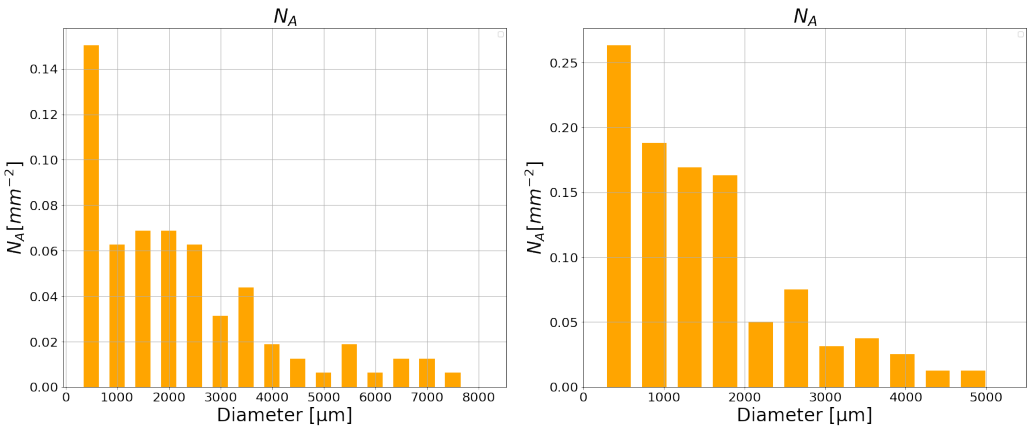

(a) Reference (b) Inoculated

Figure 61: Number density in mm^{-2} as a function of grain diameter(μm) for the T.A. cup samples.

The T.A.-cup EBSD maps were analyzed in ImageJ, and the grain size distribution was given as output. The data was converted to three dimensions and fitted to a log-normal curve. The fitted curves for the reference and inoculated samples are plotted in Figure 62. The inoculated sample contains a higher number of grains per cubic millimeter compared to the reference sample.

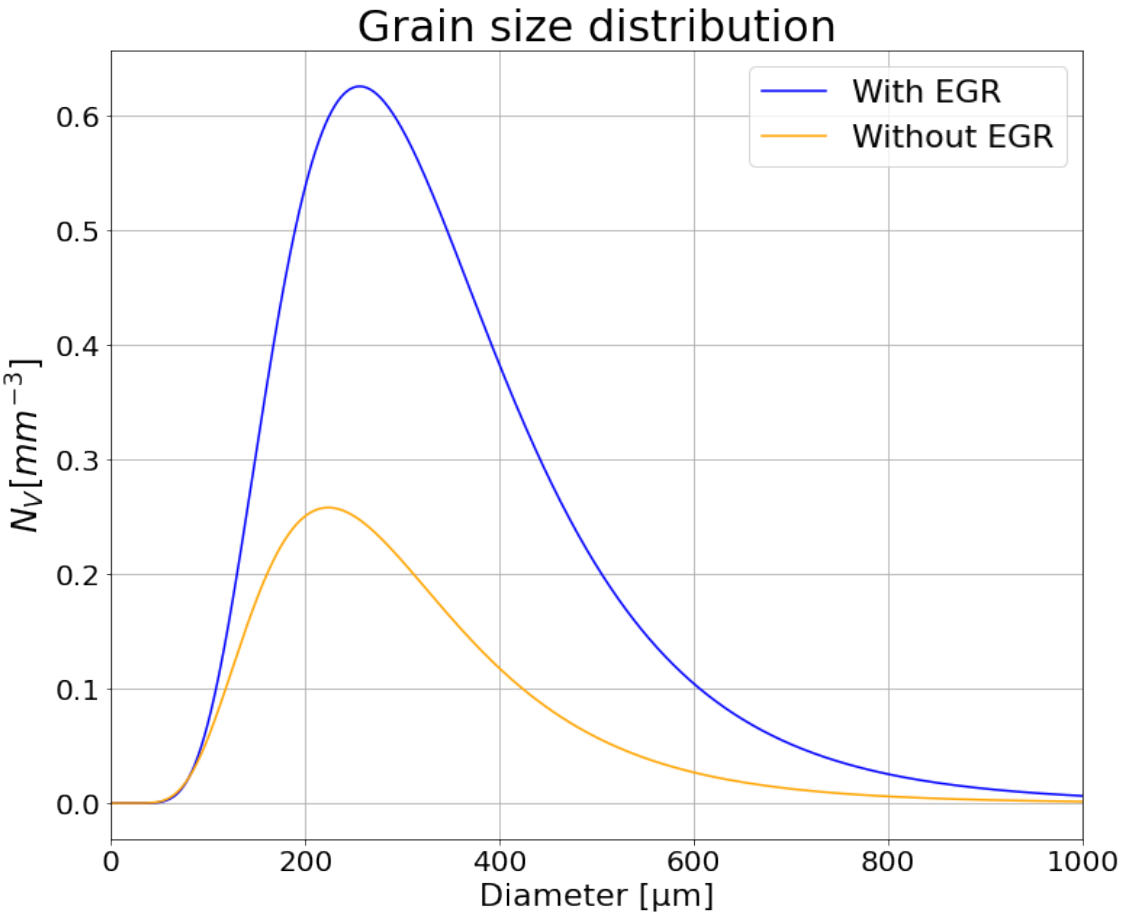

Figure 62: Grain size distribution for T.A cup samples with and without EGR.

The nucleation potency, N_V was calculated for the three-dimensional distribution by dividing the number density of grains by the number density of cerium inclusions in the inoculated T.A. cup sample:

$$N_V = \frac{N_{V,grain}}{N_{V,Ce}} \tag{28}$$

The result is given in Table 23.

Table 23: Nucleation potency for the inoculated T.A. cup sample with respect to the 3D distributions of grains and Ce-bearing inclusions.

	Nucleation potency
3D	0.0004%

A nucleation potency of 0.0004% was achieved through inoculation.

5 Discussion

5.1 Influence of casting trial parameters on the recovery of Ce

In Table 10, the targeted and measured cerium contents in each of the samples are presented. The cerium recovery ratio varied greatly and was significantly lower than what is experienced in the industry. For the addition level focused on in this thesis, the recovery rate of Ce was 25.6%. Several factors will influence the yield of the EGR during manufacturing. The industry standard for the addition of EGR in steel is that the EGR is added at the same time as the melt is poured into the ladle when a layer of melt is already covering the bottom of the ladle. This is done to ensure sufficient mixing and distribution of the inoculants. Furthermore, it decreases the degree of interaction between the EGR and the surface walls of the ladle. These interactions should be avoided as they can be associated with a decreased recovery rate. During the casting trial, the EGR was added at the bottom of each ladle corresponding to the castings with different EGR addition levels. Insufficient mixing of the EGR could thus explain the low cerium yield for the trial.

5.2 Thermal analysis and Factsage predictions

The cooling curves for thermal analysis cups were, unfortunately, characterized by large deviations between the parallels with the same addition levels, as shown in Figure 24. Hence, valid data on the effect of EGR additions on thermal phenomena such as solidus and liquidus temperatures could not be quantified. Additionally, the data acquired from the trials did not correlate to what was predicted in the Factsage equilibrium diagrams.

The Factsage diagrams in Figure 23 show the predicted solidification route of the reference and inoculated samples. Common for both is the initial formation of δ-ferrite. For austenitic steels, this is generally only a high-temperature phase, as it is expected to transform to austenite either through a peritectic or solid-state transformation. However, the Factsage diagram predicts the formation of δ-ferrite again at lower temperatures. The amounts of δ-ferrite predicted by Factsage in the final microstructure of the steel were not observed. This may be explained by the high cooling rate obtained in the casting trials, thus making the steel deviate from its equilibrium solidification route.

Likewise, the Factsage diagrams predicted the formation of some nitrides, carbides, and other phases. These were not detected during the SEM/EDX analysis of the inclusions and phases in the sample nor in the AMICS data. In the reference samples, however, some phases containing phosphorus were found. These were predicted in the inoculated sample by Factsage, but not in the reference sample, as can be seen in Figure 37. These phases were not found in the inoculated sample. This indicates that the phosphorous-containing intermetallic phase in Figure 37 may be Cr_3P or Mo_3P.

5.3 Grain refinement of the T.A. cups through EGR addition

The macroscopic examination of the T.A. cups in Figure 25 reveals a finer as-cast microstructure than the Y-block samples. In the inoculated sample, the degree of columnar characteristics is visibly reduced compared to the reference sample. An initial view of the images also reveals a remarkable grain size reduction by the EGR addition.

The LOM analysis of the samples also reveals the refinement effect of the cerium inclusions in the inoculated alloys. Figure 26 clearly shows a refinement effect through the reduction of dendrite arm thickness. Calculations on the secondary dendrite arm spacing in the T.A. cup samples gave a 27% reduction for the inoculated sample. The reduction in SDAS indicates a shorter local solidification time,t_f, of the dendrites by EGR addition. As mentioned in Section 2.7.1, the SDAS is closely related to the segregation and formation of interdendritic phases. Hence, the reduction of the SDAS in the inoculated sample may affect the precipitation of intermetallic phases.

As shown in Figure 27 and Table 12, the addition of EGR also influenced the columnar characteristics of the microstructure through the reductions of the total length of columnar zones and the length of the longest columnar grains. A reduction of 60% and 73% for the length of columnar zones and longest grain, respectively, for the inoculated T.A. cup show that the EGR promotes a columnar to equiaxed transition during solidification.

The EBDS maps of the T.A. cups can also confirm the columnar to equiaxed transition. As can be observed in Figures 29 and 28, the columnar characteristics of the grains were significantly suppressed by the addition of EGR. It can be observed that an almost completely equiaxed grain structure dominates the inoculated sample, while the reference samples consist of long columnar grains growing towards the center. This is a clear indication of grain refinement through the heterogeneous nucleation of grains upon inoculant particles ahead of the solid/liquid interface. Some contributions may also arise from the effect of solute cerium impeding the growth through the solute effect and Q-factor.

Through the calculations of the average grain size of the T.A. cup, a refining effect of the inoculated samples can be observed. Figure 60a shows a reduction of 36% in the average grain size in the inoculated T.A. cup.

The two-dimensional grain size distributions presented in Figure 61 show the differences between the reference and inoculated T.A. cup samples. The two-dimensional grain size distribution show that a significantly larger fraction of the grains per mm^2 are in size range of 0-1000μm in the inoculated sample than in the reference. Summing the number densities in the size range 0-1000μm gives a number density of 0.2 grains per mm^2 for the reference sample compared to 0.4 grains per mm^2 for the inoculated sample. Moreover, the largest grain sizes in the inoculated sample do not exceed 5500 μm, while for the reference sample, grains up to 8000μm in diameter could be observed. In the fitted log-normal

three-dimensional distribution of the grain sizes, shown in Figure 62, it can be observed that the inoculated samples contain a significantly larger degree of smaller grains per mm^3 compared to the reference. It should be noted that due to limitations with the Saltykov conversion matrix and the required bin size for the size intervals in the 3D distribution, some larger grains were neglected, especially for the reference sample. Therefore, in reality, the distribution curve of the reference sample should be wider, spanning over larger grain diameters.

The nucleation potency calculated was 0.0004% based on three-dimensional grain size distribution and inclusions in the inoculated T.A. cup sample. This means most of the Ce-bearing inclusion particles could not act as effective nucleation sites for steel grains. The achieved nucleation potency is considerably lower compared to the literature. However, many of these studies are based on well-established inoculants in light-metal alloys, which have a considerably smaller grain size compared to steels. Moreover, the as-cast grain size of austenitic steel is known to be large. Thus it would be expected that the nucleation potency for the steel in this thesis would be some orders of magnitude lower than that of light metal alloys.

In addition to the grain refining potency of the inoculant, generally measured by atomic matching, the efficiency of the inoculants to effectively nucleate grains depends on their morphology, size distribution, and volume fraction as described in Section 2.8.3. According to the *Free growth model* proposed by Greer et al.[6], the heterogenous nucleation of grains is preferred to occur on larger inclusions. However, if the inclusions are too large, the nucleation efficiency would decrease. The size distribution of inoculant particles in the melt is important to obtain the optimal potency for the nucleation of equiaxed grains in the melt. Figure 50a shows the two-dimensional size distribution of the cerium inclusions in the inoculated T.A. cup. Grong et al.[2] suggested a distribution of inoculants where a larger number of inclusions of the size of about one micron is optimal for the refinement process. Comparing this with the two-dimensional size distribution in Figure 50a and the three-dimensional size distribution in Figure 54a for the cerium inclusions obtained in this thesis, we can observe that it is a good match with what was suggested by Grong et al. in Figure 9. It can be observed that the size of the cerium inclusions is mainly between one and three microns, with an average size of about 1.8μm for the T.A. cups. TiB_6 particles in the size range of 2-5μm has been documented as active heterogeneous nucleation sites in Al alloys[71, 72, 73]. Hence, it is reasonable to consider cerium inclusions larger than 1μm as potential active nucleation sites. However, the optimum size of inoculants in steels is not yet documented. Based on these conclusions, the nucleation of equiaxed grains should be amplified. Though the nucleation of equiaxed grains was documented in the T.A. cup sample, the reason for the low calculated nucleation frequency remains unanswered.

Another consideration of the grain refinement potential is the initial phase nucleating upon the cerium inclusions. The Factsage equilibrium diagrams show that the first phase

to form during the solidification of the steel is δ-ferrite which will have a different lattice mismatch with the potential cerium-containing inclusions. The δ-ferrite will later do a solid-state transformation into austenite. Hence, the grain refinement potency of the cerium inclusions also has to take into account their ability to nucleate δ-ferrite grains.

5.4 Grain refinement of the Y-blocks through EGR addition

The refinement effect in the Y-blocks was not as significant as in the T.A. cups under the solidification conditions of the casting trials. However, both the macroscopic examination and grain size measurements on the EBSD maps documented the effect of the EGR addition. In the macro-etching images of the Y-block shown in Figure 30, the refinement effect was clearly visible. The uninoculated sample consisted only of columnar grains extending into the center of the block. In the inoculated sample, the columnar zones were clearly suppressed, growing 1-2cm towards the center of the casting before being replaced with an equiaxed zone.

The EBSD results of the Y-block did not document the same effect of the EGR. A clear equiaxed zone in the inoculated Y-block could not be observed, though some equiaxed grains were witnessed in the inoculated samples near the center. From Figures 31 and 32, it is evident that the addition of EGR did not achieve a complete columnar to equiaxed transition. However, the Y-blocks also experienced a drop in the average grain size with inoculation(18%), as is presented in Table 60. Hence the EGR addition successfully achieved some refinement for the larger casting.

As listed in Table 22, the degree of refinement on the average grain size was much more evident in the T.A. cups, which experienced a 36% reduction in grain size compared to the 18% observed in the Y-block. Several factors may explain why this is the case: One factor is the effect of the temperature gradient within the solidifying melt. The Y-block samples were much larger than the T.A. cups, resulting in a significantly longer total solidification time and a large temperature gradient throughout the casting. As described in Section 2.8.4, a larger temperature gradient is generally associated with negatively impacting the columnar to equiaxed transition, leading to a suppression of the grain refinement effect of the cerium-containing inoculants. The effect of the temperature gradient can also explain why the grain size in the Y-block is significantly larger than in the T.A. cups, even for the inoculated sample.

The longer solidification time of larger casting may also have influenced the grain size through the fading mechanism and segregation of cerium. As mentioned in Section 2.8.5, a longer time for the inoculants in the melt will, in many cases, reduce the efficiency of the grain refinement. As the time in the melt increases due to the longer solidification time, the cerium inclusions may agglomerate, forming large inclusions and thus reducing the number of active potential nucleation sites ahead of the solid/liquid interface on which

heterogeneous nucleation can be initiated.

5.5 Composition of non-metallic inclusions

The uninoculated samples consisted mainly of Al_2O_3 inclusions and some MnS particles. It is clear that these inclusions are modified by the addition of cerium in the form of EGR, as the AMICS results do not document the presence of any of these inclusions in the inoculated samples as shown in Table 21. The cerium is likely modifying the Al_2O_3 inclusions through the formation route depicted in Equation 21. This may explain the layered morphology of cerium phases observed in Figure 39, where the innermost phase is likely the one to have formed/nucleated first.

The compositional mapping of the cerium inclusions illustrated in Figure 39 was acquired during the analysis of the inoculated Y-block sample. Hence, the reason for the layering of cerium phases into larger inclusions may be promoted by the solidification time, giving the cerium more time to diffuse and agglomerate, as discussed earlier. In the Y-block, larger inclusions were observed compared to the T.A. cups, indicating an effect of the size of the castings on the size distribution of the microparticles.

Cerium aluminates and oxides were the most frequent cerium inclusions found during analysis. Some oxysulfides were also encountered, but seldom any pure cerium sulfides. The content of aluminum was relatively high in the steel due to the deoxidation process during the melting trials, thus binding the oxygen in Al_2O_3 inclusions. The level of sulfur in this steel grade is very low, so it was therefore expected not to find many cerium sulfide inclusions in the steel after inoculation.

The composition Table 15 gives that the most likely stoichiometry of the cerium inclusions found in the steel was $CeAlO_3$, CeO_2, and Ce_2O_2S. This corresponds well with other studies on cerium-based grain refiners[3, 4, 74, 57]

Bramfitts lattice disregistry model and the E2EM model both state that the lower the lattice disregistry or misfit between a given inclusion and the phase intended to nucleate upon the inclusions, the more potent the nucleating agent will be in the melt. The planar mismatch and lattice disregistry calculations by Yang et al.[60] and Van Der Eijk et al.[4] show that $CeAlO_3$ will theoretically be the most potent cerium inclusion for nucleating austenite grains in the steel melt. The $CeAlO_3$ had a lattice disregistry of 3.82% compared to Ce_2O_3's 7.7% and Ce_2O_2S's 10.2%. An abundance of the $CeAlO_3$ inclusions may therefore be desirable in order to facilitate the heterogeneous nucleation of austenite grains. The deoxidation process of the steel may therefore be essential for the optimization of the cerium inclusions in the melt. The Al_2O_3 inclusions in the reference steel, which get modified by the cerium, may, however, often be elongated and, to a degree, clustered. This may result in the cerium inclusions also being elongated and clustered, as can be

observed in Figure 39d.

As mentioned in Section 2.8.1, studies have shown that the optimal distribution of inoculants is having many inclusions between $1\mu m$ and $5\mu m$. A compromise would thus be achieved between having many potential nucleation sites and having sufficiently large inoculants for the initiation of nucleation according to the *Free growth theory*[6]. The large layered particles observed during EDX of the inoculated Y-block sample may therefore prove detrimental to the nucleation potency of the EGR. Observed in Figure 39, the multiphased inclusions in question are shown. With the $CeAlO_3$ phase in the center of the inclusions and CeO_2 formed around it, the potential lattice disregistry between the cerium inclusion and the austenite will be larger than it could have, as the cerium oxide will have a higher lattice disregistry. The layering effect can possibly be decreased by reducing the solidification time of the steel, which may suppress the layering by decreasing the time for diffusion and agglomeration in the melt. This will simultaneously provide more inclusions that may act as heterogeneous nucleation sites.

The effect of the cerium oxysulfide, Ce_2O_2S, on the nucleation potency of the larger inclusions remains unclear. As shown in some of the inclusions in Figure 39, they are usually located as smaller particles at the edges of large inclusions. The Ce_2O_2S inclusions have a higher lattice disregistry with the austenite phase. However, they are often considerably smaller in size compared to cerium oxides and aluminates, so it remains unclear their specific role in the nucleation potential of the inclusion.

5.5.1 Morphology and size distribution of inclusions

The morphology of the inclusions in the reference samples is the characteristic of the Al_2O_3 inclusions. As can be seen in Figures 42a and 42b, these appear as often elongated and needle-shaped particles. In the two-dimensional size distributions of the uninoculated samples, it was found that Al_2O_3 inclusions of size 1-5μm made up the main part of the total number of inclusions in reference samples. The three-dimensional distributions of the Al_2O_3 inclusions showed the same trend. However, the total number of Al_2O_3 inclusions per mm^3 were substantially larger in the Y-block samples compared to the T.A. cup, as is shown in Figure 56a. The opposite trend was found for the cerium-containing inclusions in the inoculated samples. As can be observed in Figure 56b, the total number of cerium inclusions per mm^3 was considerably larger in the T.A. cup sample. As discussed earlier, this may be an effect of fading due to the increased solidification time in the Y-block. However, the measured number density indicates that the fading mechanism does not occur for the Al_2O_3 inclusions.

The cerium particles are, for the most part, approximately circular in their shape, as can be seen in Figures 43a and 43b, where the morphology and size of every cerium-containing inclusions scanned during the AMICS analysis are listed. However, also elongated cerium-

containing inclusions were encountered, typically as seen in Figure 39d. These morphologies may be due to the modification of the Al_2O_3 particles by cerium, and thus achieving the same morphology.

Some limitations exist for the conversion of measured feret diameters into two-dimensional and three-dimensional distributions. For instance, will less frequent larger particles be neglected in the distributions due to their low frequency. A delta for the size ranges must be chosen, and thus a compromise must be made in order to get the distribution most characteristic for the inclusions. This may suppress the documented effect of larger inclusions in the samples.

5.5.2 Effect of cerium on pores and the precipitation of intermetallics

Intermetallic phases are often encountered in stainless steels due to their high alloying content. From the Factsage diagrams in Figure 23, such phases were expected to form in the steel. In Figure 38, SEM images of some of the intermetallics encountered are imaged. From the EDX analysis and elemental maps of these phases, their characteristics are obtained. They are enriched in molybdenum and chromium compared to the surrounding matrix while containing less nickel. Some of the compositional EDX measurements correspond to the composition of the σ-phase. The formation of the σ-phase is, as mentioned, expected from the Factsage diagrams. The χ-phase is also documented in the inoculated samples. Some of the intermetallics in the reference sample also contain a small degree of phosphorous, as observed in Figure 37.

The σ and χ-phase are often encountered together with δ-ferrite. The δ-ferrite is richer in the σ-forming elements. These include chromium, molybdenum, and silicon. Additionally, the diffusions rate of chromium and molybdenum in the δ-ferrite is considerably larger than in austenite[14], and hence the formation of the σ-phase usually occurs within δ-ferrite islands in the steel.

On the basis of Backscatter Electron Imaging, the σ, χ, and δ-ferrite phases can easily be identified. Due to the increased content of heavy elements such as molybdenum in the χ-phase, it will appear brightest during imaging, followed by the σ-phase and, lastly, the δ-ferrite. The δ-ferrite appears darker than the austenite phase as well due to its lesser content of the heavier austenite-forming elements.

Compared to the reference alloy, the number of intermetallic phases and δ-ferrite was reduced in the inoculated sample. Fewer "islands" as can be observed in Figure 38, were encountered. As intermetallic phases were less encountered in the EGR-inoculated sample, an effect of cerium inoculation on suppressing the formation of σ and χ may be suggested. In the work of Wang et al.[75], the addition of cerium reduced the Mo and Cr segregation and thus suppressed the precipitation of the σ phase, which was replaced with δ-ferrite precipitation. Furthermore, the addition of EGR was shown to decrease the secondary

dendrite arm spacing in the 316L austenitic steel. The SDAS is closely related to the degree of segregation in castings, as solute elements will be segregated interdendritically. The cerium may enrich these interdendritic regions with solute-rich liquid regions due to its low solubility in the austenite phase and thus refine the dendrite arms. This will additionally suppress the segregation of σ-forming elements in these regions. Hence, the cerium-containing inclusions can reduce the amount of unwanted phases in the steel.

Intermetallics were not included in the AMICS analysis. Hence, the amount of these phases in the reference and inoculated steel samples are not directly quantified but rather based on observation during SEM/EDX analysis of the samples. The intermetallic phases were neglected due to the threshold settings for the automatic detection of particles during the AMICS and ImageJ analysis. This makes the color of the matrix and the intermetallic phases too sclose to consistently and precisely characterize these phases.

6 Conclusion

This thesis examined the effect of EGR, a cerium-based master alloy, on the solidification structure and microparticles in austenitic stainless steel. The addition of EGR significantly refined the microstructure and grain size of the thermal analysis cup castings. The columnar characteristics of grains were greatly suppressed. This was documented through LOM analysis and measurements of the secondary dendrite arm spacing. Large-area EBSD also documented the reduction in grain size of the inoculated sample by showing a larger portion of equiaxed grains in the inoculated sample. In addition, it provided a grain size distribution, showing a higher portion of smaller grains than in the reference alloy without EGR addition.

Under the given solidification conditions of the trial, the grain refinement effect on the large Y-blocks was not as good as in the T.A. cups. In the Y-block, the effect of the temperature gradient greatly suppressed the nucleation of equiaxed grains on the inoculant inclusions, in addition to increased solidification time, possibly leading to fading phenomenon of the inoculant particles.

AMICS and SEM/EDX analysis showed that the number of intermetallic phases and pores in the samples was reduced with the addition of EGR. When added to the melt, the cerium formed oxide, aluminate, and oxysulfide inclusions. The cerium oxides and aluminates were the most frequent cerium inclusions. It is suspected that the cerium inclusions have formed on Al_2O_3 particles in the melt.

7 Future work

Further work on inoculation grain refinement of steels with EGR would be beneficial to truly understand the mechanisms associated with the inoculation process. Acquiring lattice parameters on the different cerium inclusions formed when added to the steel melt would give a more specific understanding of each of the cerium inclusions' ability to initiate heterogeneous nucleation of both austenite and δ-ferrite grains. A TEM study of the inclusions could achieve this.

Furthermore, knowledge of the mechanisms leading to fewer and larger inclusions in large castings is needed. This may be achieved by studying the effect of different holding times of EGR in the steel melt before solidification.

Bibliography

[1] Harry Bhadeshia and Robert Honeycombe. *Steels: microstructure and properties*. Butterworth-Heinemann, 2017.

[2] Øystein Grong et al. "Microstructure control of steels through dispersoid metallurgy using novel grain refining alloys". In: *ISIJ international* 46.6 (2006), pp. 824–831.

[3] Fredrik Haakonsen. "Optimizing of Strømhard austenitic manganese steel". In: (2009).

[4] Casper Van Der Eijk et al. "Grain refinement of fully austenitic stainless steels using a Fe-Cr-Si-Ce master alloy". In: *ELECTRIC FURNACE CONFERENCE*. Vol. 59. 2001, pp. 51–60.

[5] Bruce L Bramfitt. "The effect of carbide and nitride additions on the heterogeneous nucleation behavior of liquid iron". In: *Metallurgical Transactions* 1.7 (1970), pp. 1987–1995.

[6] AL Greer et al. "Modelling of inoculation of metallic melts: application to grain refinement of aluminium by Al–Ti–B". In: *Acta materialia* 48.11 (2000), pp. 2823–2835.

[7] Marshall.P. *Austenitic Stainless Steels: Microstructure and Mechanical properties*. Elsevier Applied Science Publishers, 1984.

[8] V. Kain. "5 - Stress corrosion cracking (SCC) in stainless steels". In: *Stress Corrosion Cracking*. Ed. by V.S. Raja and Tetsuo Shoji. Woodhead Publishing Series in Metals and Surface Engineering. Woodhead Publishing, 2011, pp. 199–244. ISBN: 978-1-84569-673-3. DOI: https://doi.org/10.1533/9780857093769.3.199. URL: https://www.sciencedirect.com/science/article/pii/B9781845696733500055.

[9] Joseph R Davis et al. *Stainless steels*. ASM international, 1994.

[10] Kin Ho Lo, Chan Hung Shek, and JKL Lai. "Recent developments in stainless steels". In: *Materials Science and Engineering: R: Reports* 65.4-6 (2009), pp. 39–104.

[11] Clive R Clayton and INGEMAR Olefjord. "Passivity of austenitic stainless steels". In: *Corrosion mechanism in theory and practice, Marcel Dekker, NY* (1995).

[12] Michael F McGuire. *Stainless steels for design engineers*. Asm International, 2008.

[13] Marián Vach et al. "Evolution of secondary phases in austenitic stainless steels during long-term exposures at 600, 650 and 800 C". In: *Materials Characterization* 59.12 (2008), pp. 1792–1798.

[14] A Perron et al. "Understanding sigma-phase precipitation in a stabilized austenitic stainless steel (316Nb) through complementary CALPHAD-based and experimental investigations". In: *Acta materialia* 79 (2014), pp. 16–29.

[15] DM Escriba et al. "Chi-phase precipitation in a duplex stainless steel". In: *Materials Characterization* 60.11 (2009), pp. 1214–1219.

[16] Wilfried Kurz and David J Fisher. *Fundamentals of solidification*. 1984.

[17] Jonathan A Dantzig and Michel Rappaz. *Solidification: -Revised & Expanded*. EPFL press, 2016.

[18] David A Porter and Kenneth E Easterling. *Phase transformations in metals and alloys (revised reprint)*. CRC press, 2009.

[19] T.E. Quested and A.L. Greer. "Athermal heterogeneous nucleation of solidification". In: *Acta Materialia* 53.9 (2005), pp. 2683–2692. ISSN: 1359-6454. DOI: https://doi.org/10.1016/j.actamat.2005.02.028. URL: https://www.sciencedirect.com/science/article/pii/S1359645405001291.

[20] DH StJohn et al. "The Interdependence Theory: The relationship between grain formation and nucleant selection". In: *Acta Materialia* 59.12 (2011), pp. 4907–4921.

[21] Yijiang Xu et al. "Revealing the heterogeneous nucleation behavior of equiaxed grains of inoculated Al alloys during directional solidification". In: *Acta Materialia* 149 (2018), pp. 312–325. ISSN: 1359-6454. DOI: https://doi.org/10.1016/j.actamat.2018.02.058. URL: https://www.sciencedirect.com/science/article/pii/S1359645418301745.

[22] Mark Easton and David StJohn. "Grain refinement of aluminum alloys: Part II. Confirmation of, and a mechanism for, the solute paradigm". In: *Metallurgical and Materials Transactions A* 30.6 (1999), pp. 1625–1633.

[23] Seppo Louhenkilpi. "Chapter 1.8 - Continuous Casting of Steel". In: *Treatise on Process Metallurgy*. Ed. by Seshadri Seetharaman. Boston: Elsevier, 2014, pp. 373–434. ISBN: 978-0-08-096988-6. DOI: https://doi.org/10.1016/B978-0-08-096988-6.00007-9. URL: https://www.sciencedirect.com/science/article/pii/B9780080969886000079.

[24] Doru Stefanescu and Roxana Ruxanda. "Fundamentals of Solidification". In: vol. 9. Feb. 2004, pp. 71–92. ISBN: 978-1-62708-177-1. DOI: 10.31399/asm.hb.v09.a0003724.

[25] Dominique Bouchard and John S Kirkaldy. "Prediction of dendrite arm spacings in unsteady-and steady-state heat flow of unidirectionally solidified binary alloys". In: *Metallurgical and Materials Transactions B* 28.4 (1997), pp. 651–663.

[26] George Ellwood Dieter and David Bacon. *Mechanical metallurgy*. Vol. 3. McGraw-hill New York, 1976.

[27] Feng Wang et al. "The influence of the effect of solute on the thermodynamic driving force on grain refinement of Al alloys". In: *Metallurgical and Materials Transactions A* 46.1 (2015), pp. 505–515.

[28] P Lan et al. "Analysis of solidification microstructure and hot ductility of Fe–22Mn–0· 7C TWIP steel". In: *Materials Science and Technology* 30.11 (2014), pp. 1297–1304.

[29] R Tuttle. "Effect of rare earth additions on grain refinement of plain carbon steels". In: *International Journal of Metalcasting* 6.2 (2012), pp. 51–65.

[30] Yahia Ali et al. “Current research progress in grain refinement of cast magnesium alloys: A review article”. In: *Journal of Alloys and Compounds* 619 (2015), pp. 639–651.

[31] TE Quested and AL Greer. “The effect of the size distribution of inoculant particles on as-cast grain size in aluminium alloys”. In: *Acta materialia* 52.13 (2004), pp. 3859–3868.

[32] M.A Easton and D.H StJohn. “A model of grain refinement incorporating alloy constitution and potency of heterogeneous nucleant particles”. In: *Acta Materialia* 49.10 (2001), pp. 1867–1878. ISSN: 1359-6454. DOI: https://doi.org/10.1016/S1359-6454(00)00368-2. URL: https://www.sciencedirect.com/science/article/pii/S1359645400003682.

[33] M-X Zhang and PM Kelly. “Edge-to-edge matching model for predicting orientation relationships and habit planes—the improvements”. In: *Scripta Materialia* 52.10 (2005), pp. 963–968.

[34] Ming-Xing Zhang and Patrick M Kelly. “Crystallographic features of phase transformations in solids”. In: *Progress in Materials Science* 54.8 (2009), pp. 1101–1170.

[35] Ming Li et al. “A new grain refiner for ferritic steels”. In: *Metallurgical and Materials Transactions B* 48.6 (2017), pp. 2902–2912.

[36] Dong Qiu, Ming-Xing Zhang, and Patrick M Kelly. “Crystallography of heterogeneous nucleation of Mg grains on Al2Y nucleation particles in an Mg–10 wt.% Y alloy”. In: *Scripta Materialia* 61.3 (2009), pp. 312–315.

[37] David H Stjohn et al. “New approach to analysis of grain refinement”. In: *International Journal of Cast Metals Research* 20.3 (2007), pp. 131–135.

[38] David H StJohn et al. “Grain refinement of magnesium alloys”. In: *Metallurgical and Materials Transactions A* 36 (2005), pp. 1669–1679.

[39] BS Murty, SA Kori, and M Chakraborty. “Grain refinement of aluminium and its alloys by heterogeneous nucleation and alloying”. In: *International Materials Reviews* 47.1 (2002), pp. 3–29.

[40] TV Atamanenko et al. “Criteria of grain refinement induced by ultrasonic melt treatment of aluminum alloys containing Zr and Ti”. In: *Metallurgical and Materials Transactions A* 41 (2010), pp. 2056–2066.

[41] H. Men and Z. Fan. “Effects of solute content on grain refinement in an isothermal melt”. In: *Acta Materialia* 59.7 (2011), pp. 2704–2712. ISSN: 1359-6454. DOI: https://doi.org/10.1016/j.actamat.2011.01.008. URL: https://www.sciencedirect.com/science/article/pii/S1359645411000127.

[42] Da Shu et al. “A quantitative study of solute diffusion field effects on heterogeneous nucleation and the grain size of alloys”. In: *Acta Materialia* 59.5 (2011), pp. 2135–2144.

[43] Qiang Du and Yanjun Li. “An extension of the Kampmann–Wagner numerical model towards as-cast grain size prediction of multicomponent aluminum alloys”. In: *Acta materialia* 71 (2014), pp. 380–389.

[44] I Maxwell and A Hellawell. “A simple model for grain refinement during solidification”. In: *Acta Metallurgica* 23.2 (1975), pp. 229–237.

[45] Cláudio A Siqueira, Noé Cheung, and Amauri Garcia. “Solidification thermal parameters affecting the columnar-to-equiaxed transition”. In: *Metallurgical and Materials Transactions A* 33 (2002), pp. 2107–2118.

[46] DA Pineda and Marcelo de Aquino Martorano. “Columnar to equiaxed transition in directional solidification of inoculated melts”. In: *Acta materialia* 61.5 (2013), pp. 1785–1797.

[47] H Jung et al. “Columnar to equiaxed transition during directional solidification in refined Al-based alloys”. In: *Journal of Alloys and Compounds* 484.1-2 (2009), pp. 739–746.

[48] James D Hunt. “Steady state columnar and equiaxed growth of dendrites and eutectic”. In: *Materials science and engineering* 65.1 (1984), pp. 75–83.

[49] M Gäumann, R Trivedi, and W Kurz. “Nucleation ahead of the advancing interface in directional solidification”. In: *Materials Science and Engineering: A* 226 (1997), pp. 763–769.

[50] Ch-A Gandin. “From constrained to unconstrained growth during directional solidification”. In: *Acta Materialia* 48.10 (2000), pp. 2483–2501.

[51] Ø. Grong T. Skaland and T. Grong. “A Model for the Graphite Formation in Ductile Cast Iron: Part I. Inoculation Mechanisms”. In: *Metallurgical and Materials Transactions A* (1993). ISSN: 10. DOI: https://doi.org/10.1007/BF02648605.

[52] Yating Shan et al. “Mechanisms of solidification structure improvement of ultra pure 17 wt% Cr ferritic stainless steel by Ti, Nb addition”. In: *Journal of Materials Science & Technology* 27.4 (2011), pp. 352–358.

[53] Chao Wang et al. “Grain refining of 409L ferritic stainless steel using Fe-Ti-N master alloy”. In: *Metallurgical and materials transactions A* 41 (2010), pp. 1616–1620.

[54] Gen Li et al. “Refinement of the solidification structure of austenitic Fe-Mn-C-Al TWIP steel”. In: *Metallurgical and Materials Transactions B* 51 (2020), pp. 452–466.

[55] Yun-ping Ji et al. “Effect of Ce on solute redistribution in liquid ahead of solid–liquid interface during solidification of Fe–4 wt.% Si alloy”. In: *Journal of Iron and Steel Research International* 28 (2021), pp. 1251–1258.

[56] H Li et al. “Influence of rare earth metals on the nucleation and solidification behavior of iron and 1045 steel”. In: *Metallurgical Transactions B* 19 (1988), pp. 383–395.

[57] Long-Mei Wang et al. “Study of application of rare earth elements in advanced low alloy steels”. In: *Journal of Alloys and Compounds* 451.1-2 (2008), pp. 534–537.

[58] Ø. Grong. “Metallurgical Modelling of Welding-2nd Ed.” In: (1997).

[59] Ming Li et al. “Crystallographic study of grain refinement in low and medium carbon steels”. In: *Philosophical Magazine* 96.15 (2016), pp. 1556–1578.

[60] Jian YANG et al. “Effect of RE oxide on growth dynamics of primary austenite grain in hardfacing layer of medium-high carbon steel”. In: *Journal of Rare Earths* 30.8 (2012), pp. 814–819. ISSN: 1002-0721. DOI: https://doi.org/10.1016/S1002-0721(12)60136-7. URL: https://www.sciencedirect.com/science/article/pii/S1002072112601367.

[61] YP Ji et al. “Grain refinement mechanism of the δ-ferrite in steels through cerium addition”. In: *Metallurgical and Materials Transactions A* 51 (2020), pp. 1707–1718.

[62] Fang-Jie Lan et al. “Effect of Rare-Earth Cerium on Nonmetallic Inclusions in Fe–Mn–C–Al Twinning-Induced Plasticity Steel”. In: *steel research international* 94.1 (2023), p. 2200421.

[63] Qiang Ren and Lifeng Zhang. “Effect of cerium content on inclusions in an ultra-low-carbon aluminum-killed steel”. In: *Metallurgical and Materials Transactions B* 51 (2020), pp. 589–600.

[64] Haixin Yang et al. “Modification of Sulfides in a High Sulfur Steel by Cerium Addition”. In: *Metallurgical and Materials Transactions B* 53.6 (2022), pp. 3992–4005.

[65] Fei Pan et al. “Thermodynamic Calculation among Cerium, Oxygen, and Sulfur in Liquid Iron”. In: *Scientific Reports* 6 (Oct. 2016), pp. 1–6. DOI: 10.1038/srep35843.

[66] N Kojola et al. “Pilot plant study of nozzle clogging mechanisms during casting of REM treated stainless steels”. In: *Ironmaking & Steelmaking* 38.1 (2011), pp. 1–11. DOI: 10.1179/030192310X12690127076398. URL: https://doi.org/10.1179/030192310X12690127076398.

[67] Yuri Gulbin. “ON ESTIMATION AND HYPOTHESIS TESTING OF THE GRAIN SIZE DISTRIBUTION BY THE SALTYKOV METHOD”. In: *Image Analysis Stereology* 27.3 (2011), pp. 163–174. ISSN: 1854-5165. DOI: 10.5566/ias.v27.p163-174. URL: https://www.ias-iss.org/ojs/IAS/article/view/841.

[68] C.B Basak and A.K Sengupta. “Development of a FDM based code to determine the 3-D size distribution of homogeneously dispersed spherical second phase from microstructure: a case study on nodular cast iron”. In: *Scripta Materialia* 51.3 (2004), pp. 255–260. ISSN: 1359-6462. DOI: https://doi.org/10.1016/j.scriptamat.2004.04.009. URL: https://www.sciencedirect.com/science/article/pii/S1359646204002222.

[69] L. MICHELS. “Effect of Holding Time on Populations of Microparticles in Spheroidal Graphite Irons”. In: *Metallurgical and Materials Transactions B* ().

[70] *Standard Test Methods for Determining Average Grain Size*.

[71] D Qiu and M-X Zhang. “Effect of active heterogeneous nucleation particles on the grain refining efficiency in an Mg–10 wt.% Y cast alloy”. In: *Journal of alloys and compounds* 488.1 (2009), pp. 260–264.

[72] Ma Qian, DH StJohn, and MT Frost. “Heterogeneous nuclei size in magnesium–zirconium alloys”. In: *Scripta Materialia* 50.8 (2004), pp. 1115–1119.

[73] Mark Easton and David StJohn. “An analysis of the relationship between grain size, solute content, and the potency and number density of nucleant particles”. In: *Metallurgical and materials transactions A* 36.7 (2005), pp. 1911–1920.

[74] Yunping Ji, Ming-Xing Zhang, and Huiping Ren. “Roles of lanthanum and cerium in grain refinement of steels during solidification”. In: *Metals* 8.11 (2018), p. 884.

[75] Qi Wang et al. “The influence of Ce micro-alloying on the precipitation of inter-metallic sigma phase during solidification of super-austenitic stainless steels”. In: *Journal of Alloys and Compounds* 815 (2020), p. 152418.

Appendix

A Casting trial

Table 24: EGR addition and cerium recovery for all castings in the trial. Percentages in weight percent.

Casting No.	**1**	**2**	**3**	**4**	**5**	**6**
EGR addition	0.6%	1.5%	0.3%	0.0%	0.1%	0.6%
Cerium recovery	37.9%	25.6%	35.9%	-	46.2%	25.6%

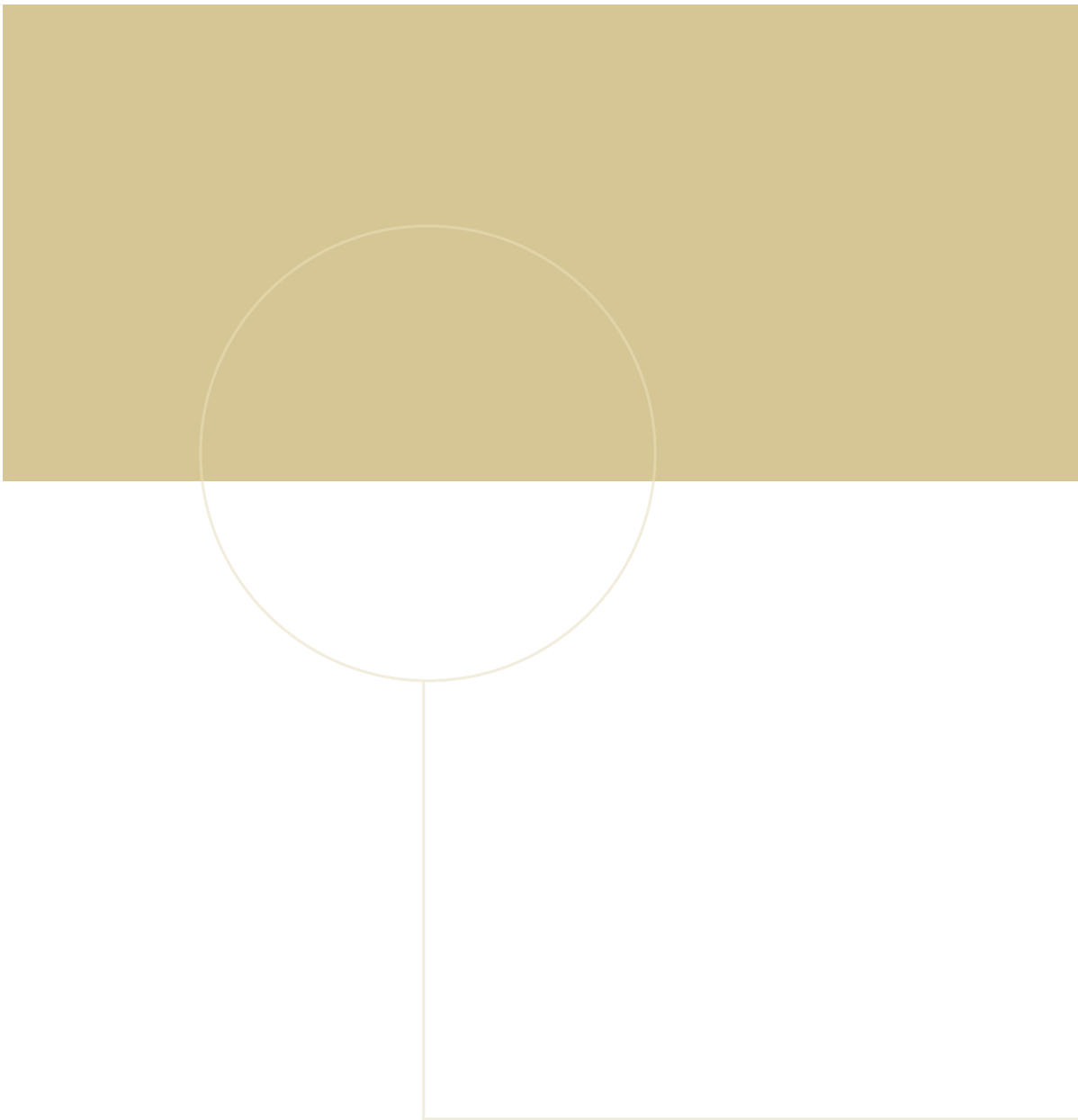

NTNU

Norwegian University of
Science and Technology